UNIVERSITY OF CALIFORNIA SAN DIEGO

Mechanisms of Cystinosis Regenerative Therapies and Pathogenesis

A dissertation submitted in partial satisfaction of the requirements for the degree Doctor of Philosophy

in

Biomedical Sciences

by

Spencer Goodman

Committee in charge:

Professor Stephanie Cherqui, Chair
Professor Chris Glass
Professor Shelly Halpain
Professor Samara Reck-Peterson
Professor Jing Yang

2020

The dissertation of Spencer Goodman is approved, and it is acceptable in quality and form for publication on microfilm and electronically:

Chair

University of California San Diego

2020

DEDICATION

This work is dedicated to my family and friends without whom I would never have been able to reach graduate school, much less complete this thesis. My research was only possible because of their support, so really in a way they are responsible for these pages and this science being created. Mom and Dad, Devin, Dina and all my BMS colleagues and old friends – thank you for your help and support, friendship and companionship and for always being up for an adventure.

On a far lighter note, I would also like to thank the bartenders and waitstaff of the dearly departed La Jolla Rock Bottom. Even though it was recently and tragically taken from us, in my earlier graduate years the "bench-to-bar" proximity was instrumental for both coming up with new ideas and maintaining sanity after experimental dead ends. RB, you will be missed.

Finally, to any grad student who happens to read this while desperately trying to figure out how to get an assay to work at 3AM: stay strong, keep a clean lab notebook, and good luck.

TABLE OF CONTENTS

LIST OF ABBREVIATIONS

Acryonym	Definition	Acryonym	Definition	Acryonym	Definition
2D	two dimensional	FXN or hFXN	human frataxin	PCR	polymerase chain reaction
3D	three dimensional	Gapdh	Glyceraldehyde 3-phosphate dehydrogenase	PFA	paraformaldehyde
6PG	6-phosphogluconate	H&E	haematoxylin and eosin	PH	pleckstrin homology
ANOVA	analysis of variance	HPLC	High-performance liquid chromatography	PHI	personal health information
Arg1	arginase 1	HSPC	hematopoietic stem and progenitor cell	Plek	pleckstrin
BMDMs	bone marrow derived macrophages	Iba1	Ionized calcium binding adaptor molecule 1	Plek No-C	pleckstrin amino acids 1-245
bp	basepair	iNOS	inducible nitric oxide synthase	Plek No-N	pleckstrin amino acids 103-350
Carkl	carbohydrate-like kinase	kbp	kilo basepair	PPP	pentose phosphate pathway
CBC	complete blood count	kD	kilodalton	QC	quality check
CC16	clara cell protein 16	KO	knockout	qPCR	quantitative polymerase chain reaction
Cdc42	cell division control protein 42 homolog	L5	lumbar level 5	R4P	ribose-4-phosphate
CKD	chronic kidney disease	LMW	low molecular weight	Rac2	Ras-related C3 botulinum toxin substrate 2
cm	centimeters	LV	lentiviral vector	RCM	reflectance confocal microscopy
CN	cystinotic	Lyz2	Lysozyme C-2	RNAseq	RNA sequenceing
CNS	central nervous system	M(IL-4/IL-10)	anti-inflammatory/alterantive macropahges	ROI	region of interest
co-IP	co-immunoprecipitated	M(LPS/IFNγ)	proinflammatory/classical macrophages	RT	room temperature
Cox8	Cytochrome c oxidase subunit 8A	MCP1	monocyte chemoattractant protein 1	S7P	sedoheptulose-7-phosphate
CRISPR	clustered regularly interspaced short palindromic repeats	mfxn	murine frataxin	Sca1	stem cells antigen 1
Ctns	cystinosin	MHCII	major histocompatibility complex class II	SDS	sodium dodecyl sulfate
cytoB	cytochalasin B	mm	milimeters	SEM	standard error of the mean
DRG	dorsal root ganglia	MOI	multiplicty of infection	Shpk	Sedoheptulokinase
E4P	erythrose-4-phosphate	MuRF-1	muscle RING finger 1	TNT	tunneling nanotube
eGFP or GFP	(enhanced) green fluorescent protein	nCCV	normalized confocal crystal volume	TSH	thyroid stimulating hormone
eGFR	estimated glomular filtration rate	NEM	N-Ethylmaleimide	WBC	white blood cell
ELISA	enzyme linked immunosorbet assay	NeuN	neuronal nuclei	WT	wild-type
FACS	Fluorescence-activated cell sorting	NGS	next generation sequencing	X4P	xylose-4-phopshate
FDA	food and drug administration	OCT	optimal cutting temperature	XO	xanthine oxidase
Fe-S	iron-sulfide	PARP1	poly(adenosine 5′-diphosphate–ribose) polymerase 1	YG8R	B6.Cg-Fxntm1Mkn Tg(FXN)YG8Pook/J
FRDA	Friedreich's Ataxia	PBS	phosphate buffered saline	μm	micrometers

LIST OF FIGURES

LIST OF TABLES

LIST OF SUPPLEMENTAL FILES

Supplemental File 1: Supplemental materials for Chapter 2

Supplemental File 2: Supplemental materials for Chapter 3.1

Supplemental Videos 3.1, 3.2: 3D modeling of eGFP BMDM and IC-21

Supplemental Videos 3.3, 3.4, 3.5: 3D-modeling of cystinosin- and frataxin-eGFP IC-21 with DsRed+ fibroblasts

Supplemental File 3: Supplemental materials for Chapter 4

Supplemental File 4: Supplemental materials for Chapter 5

Supplemental Videos 5.1, 5.2: Raw intradermal confocal image stacks

Supplemental Videos 5.3, 5.4: Selection for isolated crystal and skin structure in 2D

Supplemental Videos 5.5, 5.6: 3D reconstructions of isolated crystals and skin structure

Supplemental Videos 5.7, 5.8. 3D reconstructions of case study patient images

ACKNOWLEDGEMENTS

I would like to gratefully acknowledge Professor Stephanie Cherqui for her mentorship and support as the chair of my committee. Stephanie always challenged me, and all our lab members, to critically reason and put the best science forward. Through experimental brainstorming to sending us present at annual conferences to many, many, many rough drafts of manuscripts her support has been invaluable.

I would also like to thank all the members of the Cherqui lab past and present who have helped me in countless ways. From assay troubleshooting to commiserating over failed experiments, I'll always remember and treasure my time with the group. Getting to know each and every colleague was rewarding and enjoyable – I'd like to specifically thank Emily Chua, Riley Smith, Dr. Tatiana Lobry, Dr. Priyanka Mishra, Lei Cao and Joseph Rainaldi as they do not appear as acknowledged co-authors below.

Chapter 2, in full, is a reprint of the material as it appears in Science Translational Medicine 2017. *Rocca, Celine J., Spencer M. Goodman, Jennifer N. Dulin, Joseph H. Haquang, Ilya Gertsman, Jordan Blondelle, Janell L. M. Smith, Charles J. Heyser, and Stephanie Cherqui. "Transplantation of Wild-type Mouse Hematopoietic Stem and Progenitor Cells Ameliorates Deficits in a Mouse Model of Friedreich's Ataxia." 9.413 (2017).* The dissertation author was a co-investigator and the second author of this paper.

Chapter 3.1, in full, is a reprint of the material as it appears in *Goodman, S., Naphade, S., Khan, M., Sharma, J. & Cherqui, S. Macrophage polarization impacts tunneling nanotube formation and intercellular organelle trafficking. Sci Rep 9, 14529, doi:10.1038/s41598-019-50971-x (2019).* The dissertation author was the primary investigator and author of this paper.

Chapter 3.2 is based on unpublished work with the coauthors Eniko Sajti, Rebecca Melton, Chris Glass and Stephanie Cherqui. The dissertation author was the primary investigator of this work.

Chapter 3.4 is based on unpublished work with the coauthors Swati Naphade, Ilya Gertsman and Stephanie Cherqui. The dissertation author was the co-primary investigator of this work.

Chapter 4, in whole, is currently being prepared for submission for publication of the material. Goodman, S., Khan, M., Li, Z., Sharma, J., Cano, J., Costellanos, C., Estrada, V., Gertsman, I., Cherqui, S. The dissertation author was the primary investigator and author of this material.

Chapter 5, in whole, has been submitted for publication of the material which may appear in Journal of the American Medical Association. Bengali, M., Goodman, S., Sun, X., Dohil, M., Newbury, R., Dohil, R., Jain, S., Cherqui, S. *"Intradermal imaging of cystine crystals as a non-invasive biomarker for cystinosis."* The dissertation author was the co-primary investigation and equally collaborated in writing the paper.

VITA

2010	Undergraduate Research Assistant, Finnerty Lab, Boston University, Boston
2012	Bachelor of Science, Cum Laude, Boston University, Boston
2012-2014	Postbaccaleurate Researcher, Friedman Lab, NIDCD, NIH, Bethesda
2014-2020	PhD Candidate, Cherqui Lab, University of California San Diego, San Diego
2020	Doctor of Philosophy, University of California San Diego, San Diego
2020-	Postdoctoral Fellow, Renal Biology, GNF Novartis, San Diego

PUBLICATIONS

1. **Goodman, S.**, S. Naphade, M. Khan, J. Sharma and S. Cherqui (2019). "Macrophage polarization impacts tunneling nanotube formation and intercellular organelle trafficking." Sci Rep **9**(1): 14529.
2. Rocca, C. J., **S. Goodman**, J. N. Dulin, J. H. Haquang, I. Gertsman, J. Blondelle, J. L. M. Smith, C. J. Heyser and S. Cherqui (2017). "Transplantation of wild-type mouse hematopoietic stem and progenitor cells ameliorates deficits in a mouse model of Friedreich's ataxia." Sci Transl Med **9**(413).
3. Ariazi, J., A. Benowitz, V. De Biasi, M. L. Den Boer, S. Cherqui, H. Cui, N. Douillet, E. A. Eugenin, D. Favre, **S. Goodman**, K. Gousset, D. Hanein, D. I. Israel, S. Kimura, R. B. Kirkpatrick, N. Kuhn, C. Jeong, E. Lou, R. Mailliard, S. Maio, G. Okafo, M. Osswald, J. Pasquier, R. Polak, G. Pradel, B. de Rooij, P. Schaeffer, V. A. Skeberdis, I. F. Smith, A. Tanveer, N. Volkmann, Z. Wu and C. Zurzolo (2017). "Tunneling Nanotubes and Gap Junctions-Their Role in Long-Range Intercellular Communication during Development, Health, and Disease Conditions." Front Mol Neurosci **10**: 333.
4. Bird, J. E., M. Barzik, M. C. Drummond, D. C. Sutton, **S. Goodman**, E. L. Morozko, S. M. Cole, A. K. Boukhvalova, J. Skidmore, D. Syam, E. A. Wilson, T. Fitzgerald, A. U. Rehman, D. M. Martin, E. T. Boger, I. A. Belyantseva and T. B. Friedman (2017). "Harnessing molecular motors for nanoscale pulldown in live cells." Mol Biol Cell **28**(3): 463-475.
5. Bengali M*, **Goodman S*** … & Cherqui, S. "Intradermal cystine crystal imaging is a novel predictive non-invasive biomarker for human cystinosis patients". *Manuscript submitted to JAMA.* (* equal contributors)
6. **Goodman S**, Khan M … & Cherqui, S. "Shpk-deficient hematopoietic stem cell therapy remains effective to rescue cystinosis". *Manuscript in preparation*.

ABSTRACT OF THE DISSERTATION

Mechanisms of Cystinosis Regenerative Therapies and Pathogenesis

by

Spencer Goodman

Doctor of Philosophy in Biomedical Sciences

University of California San Diego, 2020

Professor Stephanie Cherqui, Chair

Cystinosis is a multisystem genetic lysosomal storage disorder caused by mutations in the *CTNS* gene leading to cystine crystal accumulation within lysosomes. Current treatments merely delay disease progression so we have pioneered hematopoietic stem and progenitor cell (HSPC) transplantation in mice. Our group previously discovered that HSPC-derived macrophages are important effectors of this therapy by facilitating the delivery of functional lysosomes to diseased tissue through membranous protrusions called tunneling nanotubes (TNTs). This transplantation approach is being translated into human cystinosis patients in an ongoing Phase I/II clinical trial.

To understand the mechanistic underpinnings of this therapy, we investigated macrophage polarization and TNT-mediated intercellular trafficking. Employing an *in vitro* polarization co-culture system and automated image analysis workflows, we found that pro-inflammatory stimulation reduced TNT-like protrusion formation and lysosomal transport. However, we found that co-culture of macrophages with diseased cystinotic fibroblasts increased TNT formation and trafficking, signaling we further explored via metabolomic analysis of culture media.

Next, we addressed if *SHPK*, a metabolic gene involved in macrophage polarization that is frequently eliminated in cystinosis, is required for optimal HSPC therapy. We generated novel knockouts using CRISPR-Cas9, confirmed that *Shpk* expression was ablated and described a hepatic and urinary metabolic phenotype. We then transplanted $Shpk^{-/-}$ HSPCs into cystinotic mice and determined that they are equally efficacious as wildtype (WT) donors. Based on these findings, $SHPK^{-/-}$ patients will be enrolled as future subjects in the clinical trial.

Finally, we developed a novel clinical endpoint for the clinical trial by quantitating cystine crystals from intradermal confocal images of patients. We created an automated image analysis methodology to measure crystal density in both 2D and 3D. We found that patients have significantly higher normalized confocal crystal volume (nCCV) than healthy controls, and that this new metric correlates with patient age and several clinical outcomes. This methodology presents the potential to become a biomarker to monitor long-term disease trend, compliance with treatment, and anticipatory guidance for potential complications.

Overall, this work serves to highlight the potential of HSPC-based regenerative therapies to treat previously incurable genetic diseases. This work highlights how an understanding of basic molecular mechanisms can be directly translated into developing novel regenerative therapies for humans.

Chapter 1: Introduction

1.1: General background

As humans age and suffer from disease or injury, our tissues become damaged and lose healthy morphology and function. While current medical therapies aim to alleviate or even prevent the symptomatic manifestations of this decline, the emerging discipline of regenerative medicine seeks to translate understanding of molecular biology, genetics and tissue engineering into novel therapeutics to restore normal function of human cells, tissue and organs. With approaches ranging from stem cell-based transplantations to gene therapy to 3D printing of new organs, regenerative medicine holds the promise of utilizing the body's own repair mechanisms to fundamentally expand the nature of treatable injuries and disease.

One such orphan condition that could greatly benefit from new regenerative therapies is the main focus of this work, the genetic disorder cystinosis. Cystinosis is a classic monogenic autosomal-recessive lysosomal storage disorder caused by mutations in the *CTNS* gene that affects roughly one out of every 100,000 children (1). Detailed sequencing of many unrelated patients has revealed over 100 separate mutations ranging from small indels or substitutions to larger deletions that lead to cystinosis (2). However, by far the most common disease-causing mutation is a 57 kilo base pair (kbp) deletion spanning all 12 *CTNS* exons, as well as partial eliminations of neighboring genes *TRPV-1,* a capsaicin receptor, and *SHPK,* a glycolytic metabolic enzyme involved in macrophage polarization (3,4). Cystinotic patients lacking the *TRPV-1* gene demonstrate reduced response to capsaicin spice (potentially accounting for the high frequency of patients that enjoy spicy food), but the consequences of loss of *SHPK* are less clear, aside from changes in urinary

metabolites which may or may not be specifically due to nonfunctional *SHPK* – Chapter 4 of this dissertation further explores cystinosis and *SHPK* (5,6).

All disease-causing mutations, not just the common 57-kb deletion, in some way perturb the normal expression of cystinosin, the protein encoded by the *CTNS* gene. Cystinosin is a 41.7 kilodalton (kD) hydrogen/cystine symporter ubiquitously expressed in the lysosomal membrane (7). When normally functioning, this transporter exports cystine from the lysosome into the cytosol where it is reduced into the amino acid cysteine. However, in cystinosis, nonfunctional cystinosin results in cystine accumulation and crystallization within lysosomes. These crystals deposit all over the body and have been observed in humans in tissues ranging from the skin to the cornea (8). Among numerous other symptoms, cystinotic patients develop renal Fanconi syndrome characterized by polyuria, polydipsia, proteinuria, dehydration and failure to grow (9). Left untreated, proximal tubule failure will progress to end-stage renal disease and death by 10-12 years of age. Current specific treatment is limited to cysteamine, which depletes cystine by allowing lysosomal export through alternative channels (10). However, cysteamine, along with many other treatments to manage symptoms, requires a demanding dosing schedule (up to 60 pills a day around the clock) and has numerous negative side effects such as severe gastric issues and body odor which ensures that long-term patient compliance is difficult (11). Most importantly, cystine depletion via cysteamine merely delays and does not halt or reverse disease progression. Thus, while lifespan has been dramatically extended, patients still require multiple kidney transplants and ultimately still die early due to either renal failure or a variety of other causes of death. For this reason, our lab has focused on development revolutionary regenerative cystinosis therapies that aim to intervene at the genetic level, the ultimate cause of the disease.

Our group has focused on developing hematopoietic stem cell gene therapy for cystinosis (12-14). Hematopoiesis, or the generation of all blood derived cells, relies upon the replicative power of hematopoietic stem and progenitor cells (HSPCs). HSPCs are multipotent bone marrow cells with the ability to self-renew and differentiate into all types of blood cells ranging from erythrocytes to platelets to leukocytes. Years of previous work by our lab has developed a rigorous HSPC transplantation model using a knockout (KO) mouse model of cystinosis which accurately phenocopies many human symptoms (15,16). Recipient mice are lethally irradiated to open up the bone marrow niche, then HSPCs harvested from a healthy donor mouse are injected via the tail vein. By several months post-transplantation, HSPCs have engrafted into the bone marrow and begun differentiating into immune progeny stably resident in numerous organs including kidney, eye, brain and spleen. Measuring the critical biomarker cystine by mass spectrometry revealed a significant and persistent reduction across all tissues following transplantation of healthy but not cystinotic ($Ctns^{-/-}$) HSPCs of up to 94% clearance, and we also observed long-term histological and functional preservation of the kidney (12). A strategy using HSPCs is required for a disease like cystinosis for two key reasons; first, cystinosin is a lysosomal transmembrane protein which is not secreted, so traditional enzyme replacement therapy would not work and second, *Ctns* is ubiquitously expressed and required by every tissue, so *in vivo* viral gene therapy would be ineffective because no viral vector can successfully infect all tissues. Subsequent work began to translate this strategy to a therapy useful in humans by finding that *ex vivo* transduction of $Ctns^{-/-}$ HSPCs with a self-inactivating lentiviral vector containing WT *Ctns* cDNA was also effective for transplantation into cystinotic mice (14). Overall, a single HSPC transplantation appears to be an effective therapy preventing cystinosis disease progression permanently for the remainder of the mouse lifespan.

Mice, however, are not people. While the mouse may be one of the best model organisms to understand human biology and model therapeutic interventions, a clinical trial is ultimately required to determine how well this specific human biology can be predicted with congenic rodents. After extensive additional preclinical toxicology and pharmacology studies, our lab has begun an FDA-approved Phase I/II clinical trial to use gene-modified autologous HSPCs to treat human cystinosis (ClinicalTrials.gov Identifier: NCT03897361). HSPCs will be collected via apheresis from the blood of subjects and cells will then be infected in a dish with a lentiviral vector containing WT *CTNS* cDNA. The majority of transduced cells – which is our therapeutic product - will be frozen down while aliquots are extensively characterized to assess a safety profile based on factors such as vector copy number and insertional mutagenesis. Several months after HSPC collection, patients will be myleoablated with the chemotherapeutic drug busulfan which serves the same function as irradiation in mice, that is, to open up the bone marrow niche so that the engrafted cells have somewhere to go and live. Afterwards patients are monitored while still in isolation until various criteria indicative of successful engraftment and reconstitution of the immune system are met, at which point they can be released. Assessments of transplantation efficacy via clinical endpoints such as tests of renal function and direct measurement of cystine levels in the blood begins several months post-transplantation and will continue for several years. One important endpoint is the measurement of the amount of cystine crystals in the skin, a new automated quantitative imaging tool whose development is described in Chapter 5. This is surrogate maker to estimate non-invasively the impact of stem cells in tissues at different time points. As of June 2020, one patient underwent this process just over 6 months ago, another is due to begin within weeks and several others are scheduled to follow.

While several of the major questions this work seeks to address are directly relevant to or even involved in our ongoing clinical trial, we also are interested in precisely understanding the basic cellular and molecular mechanisms involved in HSPC transplantation therapy. After all, the actual way by which blood stem cells prevent a disorder predominantly manifesting in the kidney or thyroid or other organs is not immediately obvious. Our group demonstrated that transplanted HSPCs-derived macrophages or microglia heavily engraft into every diseased organ (17). Furthermore, transplanting DsRed *Ctns*$^{-/-}$ mice with HSPCs transduced with a CTNS-eGFP fusion protein resulted in eGFP vesicles within cystinotic cells, suggesting that delivery of functional protein from HSPC-progeny to diseased host tissue is responsible for tissue preservation. While this process of cross-correction could occur via either vesicle secretion or direct cell-cell contact, we demonstrated *in vitro* that macrophages optimally reduced cystine content in fibroblasts only when directly co-cultured but not when separated in the same media. Secretion of the cystinosin protein was therefore ruled out as the primary mechanism of cross-correction.

Confocal and electron microcopy of these co-cultures revealed a very interesting phenotype – the extension of long, thin protrusions from macrophages to fibroblasts, occasionally resulting in plasma membrane fusion between both cells. These structures are known as tunneling nanotubes (TNTs), first described in 2004 as direct cell-to-cell bridges facilitating intercellular organelle trafficking in cultured rat pheochromocytoma cells (18). While no TNT-specific molecular markers have been discovered, TNTs may be recognized on the basis of the following; thin (50-200 nm), long (up to hundreds of microns), actin-rich tubular structures protruding from the plasma membrane without making contact with the substratum (19). While most TNTs lack microtubules, a specific subset extruded from macrophages or natural killer cells are thicker than normal and stain positive for tubulin (20). They have been observed connecting numerous cell types both *in*

vitro (18, 21) and *in vivo (*20,22*) and* implicated in a wide variety of biological processes ranging from lysosomal and mitochondrial trafficking (22,23) to bacterial and prion pathogenesis (major 24-26) to calcium-mediated cellular communication (21). We determined that lysosomes are trafficked from HSPC-derived macrophages through TNTs in both cells and mice using both live *in vitro* microscopy and detailed examination of kidney sections of HSPC transplanted animals (17). The research described here in Chapter 3 extends this key finding by further investigating the cellular nature of macrophages involved in cross-correction as well as exploring the molecular machinery involved in TNT formation or induction signaling.

As a whole, this work aims to both characterize functional mechanisms of HSPC-mediated therapy as well relate and this basic knowledge to the ongoing clinical trial for cystinosis. By exploring how HSPC-derived macrophages effect the prevention of cystinosis in mice, we developed techniques and draw conclusions potentially broadly relevant to other aspects of regenerative medicine. For instance, we have applied a similar HSPC transplantation strategy to treat the mouse model of Friedreich's Ataxia (FRDA), a neuromuscular disorder caused by mutations in a mitochondrial gene (27). Such an application, described in Chapter 2 of this dissertation, highlights how multiple organellular loss-of-function disorders may be treated with HSPC therapy. Based on our work, other groups have applied the same strategy to other genetic disorders like Dent's disease (28), making a fundamental understanding of the TNT-mediated mechanisms of action even more important. At the same time, we also have the exciting opportunity to immediately apply our skills and findings to patients undergoing a first-in-human clinical trial. By bridging the gaps of basic cellular/molecular biology to translational clinical science, this work succulently demonstrates the promise (and challenges) facing cell-based regenerative therapies today.

1.2: Chapter summaries

The first section, Chapter 2, explores the applicability of our HSPC transplantation strategy for an entirely different disorder, Friedrich's Ataxia (FRDA). This disease is caused by a triplet-expansion in the frataxin gene, leading to transcriptional silencing, repression and ultimately mitochondrial dysfunction (29). We transplanted frataxin-deficient mice with WT HSPCs in order to characterize the behavioral, neurological, and molecular response (27). We observed marked improvement in many of the physiological symptoms of the disease while confirming that a similar mechanism of action involving the delivery of functional frataxin protein or entire mitochondria from HSPC-derived phagocytes – microglia in the central nervous system, in this case – potentially through TNTs. Follow-up research in the lab since our initial publication has established a CRISPR-Cas9 editing system to precisely remove the triplet expansion from human CD34+ HSPCs, with a goal to eventually use edited autologous HSPCs to treat FRDA in another clinical trial (36). Of particular importance to other Chapters presented here, many of the imaging analysis technologies from this paper were eventually refined and developed into the more complex TNT-detection or cystine crystal measurement workflows presented afterwards.

The next section, Chapter 3, describes several overlapping projects where we further explore the basic cellular and molecular mechanistic underpinnings of our HSPC transplantation therapy. The first section, Chapter 3.1, contains our published investigation into any connection between TNT formation and intercellular organelle trafficking with different subpopulations of polarized macrophages. This work sought to follow up on our initial discovery of the importance of HSPC-derived macrophages in transplantation therapy (17). We optimized an *in vitro* macrophage polarization system which experimentally confirmed previous findings of a change

towards a less elongated cellular morphology following pro-inflammatory stimulation (30). We then developed novel unbiased image analysis algorithms to quantitate the frequency of TNT-like protrusion formation as well as the relative amounts of intercellular lysosomal trafficking. Using this technology, we found that pro-inflammatory treatment of macrophages results in a reduction of TNT-like protrusion formation and intercellular spread of lysosomes. Interestingly, we also detected increased protrusion formation and trafficking following co-culture of macrophages with *Ctns*$^{-/-}$ fibroblasts as compared to WT. However, while these findings may be exciting, a major concern is the applicability of *in vitro* stimulation to the actual *in vivo* situation. Stimulation in a dish can push macrophages far beyond normal physiological phenotypes and lead to behavior which may not be replicated in a mouse, much less a human. This danger is succinctly highlighted by our attempt to detect any *in vivo* correlation to our results using *Rac2*$^{-/-}$ HSPCs. The *Rac2*$^{-/-}$ mouse model has been shown to skew macrophages towards a pro-inflammatory phenotype by disrupting normal anti-inflammatory polarization, and so we hypothesized that they would be less effective at prevention of cystinosis following HSPC transplantation (31). However, transplanting cystinotic animals with, *Rac2*$^{-/-}$ resulted in perfectly normal rescue compared to WT. Even given this discrepancy, our findings *in vitro* established a dynamic culture system to understand the intricacies of intercellular trafficking in the context of cystinosis. Furthermore, we developed image analysis technology that can be applied automatically to not only TNTs but also other cellular protrusions, an important contribution to a field challenged by lack of clearly-defined markers.

While our research presented in Chapter 3.1 followed a very focused and narrow investigation into the precise connection between macrophage polarization and TNT formation, our next section Chapter 3.2 aims to complement this with a far broader and more untargeted

methodology. Here, we utilize RNAseq to explore the transcriptome of HSPC-derived kidney-resident immune cells from transplanted cystinotic mice. We developed a complex FACS gating strategy to select different populations of immune cells, not only macrophages but also neutrophils, monocytes and others. We then performed next generation sequencing (NGS) to try to understand the differences between different cell types, between cells from different genotypes of mice, and also between HSPC-derived and endogenous host cells. While technical difficulties have so far limited the scope of our conclusions, we were able to identify novel genes potentially dysregulated in cystinosis such as Lyz2.

Moving from our cellular focus in the preceding sections, our work described in Chapter 3.3 explored the molecular underpinnings of TNT formation, which are only beginning to be understood (32). Using a DNA array differential expression approach, we identified genes which appear upregulated in transplanted cells which have undergone cross-correction – potentially indicating that these genes are required for TNT formation. The most promising candidate identified was pleckstrin (Plek), a PH-domain containing protein known to induce deformation at the plasma membrane (33, 34). We discovered that pleckstrin was necessary for optimal TNT-like protrusion formation from macrophages by using shRNA to knockdown *Plek* expression. Furthermore, we found that this mechanism may involve Rac1 or the tubulin cytoskeleton based on their co-immunoprecipitation with Plek.

In Chapter 3.4, the final section of Chapter 3, we seek to address a question raised by our work with co-cultured macrophages and cystinotic fibroblasts, showing that TNT formation was increased in presence of the diseased cells as compared to WT cells; namely, what signaling released by the diseased cells may enhance TNT-like protrusion formation and intercellular lysosomal trafficking. Taking a metabolomic approach, we investigated both secreted media as

well as intracellular fractions of co-cultures. While several purinergic candidates initially appeared promising, none were able to stimulate or suppress TNT-like protrusion formation alone and we eventually discovered that differential response by cystinotic cells to media deprivation was most likely to blame. That said, we did discover several unknown differences in energy metabolism and biosynthetic pathways by comparing WT and cystinotic cells, even if they might not appear as strikingly different in blood plasma from knockout mice.

Our work in Chapter 4 uses many of techniques and technologies we previously described to address a new more translational question highly relevant to the ongoing clinical trial. We sought to determine if *SHPK* – a gene which, in addition to *CTNS,* is deleted in the most common human cystinosis mutation, the 57-kbp deletion – is required for optimal HSPC transplantation efficacy in cystinotic mice (2). The impetus to address this issue comes from three facts; first, our autologous gene therapy strategy to treat humans provides functional *CTNS* – but not *SHPK* – cDNA. Second, *Shpk* has been reported to be involved in regulation of macrophage polarization and differentiation through its role as a glycolytic enzyme in the pentose phosphate pathway (PPP) (4). Finally, as we have described, macrophages are an essential element of our HSPC therapy (17). Especially given that all our *in vivo* mouse models rely upon deletion only of *Ctns,* we needed to understand any impact of the lack of *Shpk* on HSPC transplantation success. We therefore used CRISPR-Cas9 to generate novel mouse genomic deletions of *Shpk,* and then characterized the reduction of mRNA and protein expression across the organism. We also characterized a mild metabolic phenotype consisting of dysregulation of PPP metabolites in liver and urine. We then transplanted Shpk-deficient HSPCs into cystinotic mice and observed normally efficacious reduction in cystine, restoration of *Ctns* expression and preservation of more normal kidney histology and renal function. This work effectively bridged the gap between our extremely basic

exploration of intercellular trafficking and the ongoing clinical trial – demonstrating the importance of establishing detailed cellular and molecular understandings of novel therapies. Importantly, there was no indication from these data that human patients carrying the most common disease-causing mutation at the homozygote state would fail to benefit from HSPC therapy, and so patients carrying this mutation have been enrolled as future subjects in the trial.

Finally, Chapter 5 continues this shift to humans and clinical care by highlighting our work developing diagnostic quantitative imaging tools to reliably and reproducibly assess cystine crystal abundance in human skin . By far the largest section, Chapter 5.1 demonstrates how we imaged the skin of nearly 100 cystinosis patients and healthy controls using a handheld intradermal confocal microscope to isolate cystine crystals. To analyze these image stacks, we developed a 3D volumetric quantitation macro which generated a single value representing the overall crystal density of this particular region of the skin. We observed that patients had dramatically higher crystal volume– which we termed normalized confocal crystal volume (nCCV) – than healthy controls, potentially allowing this tool to be developed as a diagnostic aid for clinical care of cystinosis. Furthermore, when we used regression analysis to compare nCCV to various parameters of overall health obtained from patient medical records, we discovered direct correlations between nCCV and major symptoms of cystinosis like hypothyroidism or chronic kidney disease (CKD). While strategies to use crystal density as a biomarker for cystinosis have been proposed in the past, our work in Chapter 5.1 is by far the largest and most rigorously quantitative effort that will hopefully assist in building a natural history of this rare disease (8, 35). While this is quite exciting to be a part of, our original goal in developing this imaging technology and analytical technique was to generate a quantitative endpoint to assess the efficacy of HSPC transplantation during the clinical trial. The next section, Chapter 5.2, presents our preliminary

data using this methodology on the first patients to undergo gene correction and HSPC transplantation.

We conclude with Chapter 6 which draws connections between the major findings and summarizes in broad strokes how this work has moved forward the understanding of cystinosis, TNTs, macrophage polarization and intercellular trafficking in general, but also the application of these fundamental findings into the ongoing first-in-human stem cell gene therapy clinical trial for cystinosis.

1.3: References

1. Emma, F., Nesterova, G., Langman, C., Labbe, A., Cherqui, S., Goodyer, P., … Levtchenko, E. (2014). Nephropathic cystinosis: an international consensus document. Nephrology Dialysis Transplantation, 29(suppl 4), iv87–iv94. doi: 10.1093/ndt/gfu090\

2. David, D., Princiero Berlingerio, S., Elmonem, M. A., Oliveira Arcolino, F., Soliman, N., Van Den Heuvel, B., … Levtchenko, E. (2018). Molecular Basis of Cystinosis: Geographic Distribution, Functional Consequences of Mutations in the ***CTNS*** Gene, and Potential for Repair. *Nephron*, *141*(2), 133–146. doi: 10.1159/000495270

3. Buntinx, L., Voets, T., Morlion, B., Vangeel, L., Janssen, M., Cornelissen, E., … Levtchenko, E. (2016). TRPV1 dysfunction in cystinosis patients harboring the homozygous 57 kb deletion. *Scientific Reports*, *6*(1). doi: 10.1038/srep35395

4. Haschemi, A., Kosma, P., Gille, L., Evans, C. R., Burant, C. F., Starkl, P., … Wagner, O. (2012). The Sedoheptulose Kinase CARKL Directs Macrophage Polarization through Control of Glucose Metabolism. *Cell Metabolism*, *15*(6), 813–826. doi: 10.1016/j.cmet.2012.04.023

5. Yang, F., & Zheng, J. (2017). Understand spiciness: mechanism of TRPV1 channel activation by capsaicin. *Protein & Cell*, *8*(3), 169–177. doi: 10.1007/s13238-016-0353-7

6. Wamelink, M. M. C., Ramos, R. J. J. F., Annette P. M. Van Den Elzen, Ruijter, G. J. G., Bonte, R., Diogo, L., … Salomons, G. S. (2015). First two unrelated cases of isolated sedoheptulokinase deficiency: A benign disorder? *Journal of Inherited Metabolic Disease*, *38*(5), 889–894. doi: 10.1007/s10545-014-9809-1

7. Kalatzis, V. (2001). Cystinosin, the protein defective in cystinosis, is a H -driven lysosomal cystine transporter. *The EMBO Journal*, *20*(21), 5940–5949. doi: 10.1093/emboj/20.21.5940

8. Chiavérini, C., Kang, H.-Y., Sillard, L., Berard, E., Niaudet, P., Guest, G., … Ortonne, J. P. (2013). In vivo reflectance confocal microscopy of the skin: A noninvasive means of assessing body cystine accumulation in infantile cystinosis. *Journal of the American Academy of Dermatology*, *68*(4). doi: 10.1016/j.jaad.2011.08.010

9. Cherqui, S. & Courtoy, P. J. The renal Fanconi syndrome in cystinosis: pathogenic insights and therapeutic perspectives. *Nat Rev Nephrol* **13**, 115-131, doi:10.1038/nrneph.2016.182 (2017).

10. Brodin-Sartorius, A., Tête, M.-J., Niaudet, P., Antignac, C., Guest, G., Ottolenghi, C., … Servais, A. (2012). Cysteamine therapy delays the progression of nephropathic cystinosis in late adolescents and adults. *Kidney International*, *81*(2), 179–189. doi: 10.1038/ki.2011.277

11. Ariceta, G., Lara, E., Camacho, J. A., Oppenheimer, F., Vara, J., Santos, F., … Cerro, L. A. J. D. (2014). Cysteamine (Cystagon(R)) adherence in patients with cystinosis in Spain: successful in children and a challenge in adolescents and adults. *Nephrology Dialysis Transplantation*, *30*(3), 475–480. doi: 10.1093/ndt/gfu329

12. Syres, K., Harrison, F., Tadlock, M., Jester, J. V., Simpson, J., Roy, S., … Cherqui, S. (2009). Successful treatment of the murine model of cystinosis using bone marrow cell transplantation. *Blood*, *114*(12), 2542–2552. doi: 10.1182/blood-2009-03-213934

13. Yeagy, B. A., Harrison, F., Gubler, M.-C., Koziol, J. A., Salomon, D. R., & Cherqui, S. (2011). Kidney preservation by bone marrow cell transplantation in hereditary nephropathy. *Kidney International*, *79*(11), 1198–1206. doi: 10.1038/ki.2010.537

14. Harrison, F., Yeagy, B. A., Rocca, C. J., Kohn, D. B., Salomon, D. R., & Cherqui, S. (2013). Hematopoietic Stem Cell Gene Therapy for the Multisystemic Lysosomal Storage Disorder Cystinosis. *Molecular Therapy*, *21*(2), 433–444. doi: 10.1038/mt.2012.214

15. Cherqui Stéphanie, Sevin, C., Hamard, G., Kalatzis, V., Sich, M., Pequignot, M. O., … Antignac, C. (2002). Intralysosomal Cystine Accumulation in Mice Lacking Cystinosin, the Protein Defective in Cystinosis. *Molecular and Cellular Biology*, *22*(21), 7622–7632. doi: 10.1128/mcb.22.21.7622-7632.2002

16. Nevo, N., Chol, M., Bailleux, A., Kalatzis, V., Morisset, L., Devuyst, O., … Antignac, C. (2009). Renal phenotype of the cystinosis mouse model is dependent upon genetic background. *Nephrology Dialysis Transplantation*, *25*(4), 1059–1066. doi: 10.1093/ndt/gfp553

17. Naphade, S., Sharma, J., Chevronnay, H. P. G., Shook, M. A., Yeagy, B. A., Rocca, C. J., … Cherqui, S. (2014). Brief Reports: Lysosomal Cross-Correction by Hematopoietic Stem Cell-Derived Macrophages Via Tunneling Nanotubes. *Stem Cells*, *33*(1), 301–309. doi: 10.1002/stem.1835

18. Rustom, A. (2004). Nanotubular Highways for Intercellular Organelle Transport. *Science*, *303*(5660), 1007–1010. doi: 10.1126/science.1093133

19. Ariazi, J., A. Benowitz, V. De Biasi, M. L. Den Boer, S. Cherqui, H. Cui, N. Douillet, E. A. Eugenin, D. Favre, **S. Goodman**, K. Gousset, D. Hanein, D. I. Israel, S. Kimura, R. B. Kirkpatrick, N. Kuhn, C. Jeong, E. Lou, R. Mailliard, S. Maio, G. Okafo, M. Osswald, J. Pasquier, R. Polak, G. Pradel, B. de Rooij, P. Schaeffer, V. A. Skeberdis, I. F. Smith, A. Tanveer, N. Volkmann, Z. Wu and C. Zurzolo (2017). "Tunneling Nanotubes and Gap Junctions-Their Role in Long-Range Intercellular Communication during Development, Health, and Disease Conditions." Front Mol Neurosci **10**: 333.

20. Önfelt, B., Nedvetzki, S., Benninger, R. K. P., Purbhoo, M. A., Sowinski, S., Hume, A. N., … Davis, D. M. (2006). Structurally Distinct Membrane Nanotubes between Human Macrophages Support Long-Distance Vesicular Traffic or Surfing of Bacteria. *The Journal of Immunology*, *177*(12), 8476–8483. doi: 10.4049/jimmunol.177.12.8476

21. Watkins, S.C. and R.D. Salter, Functional connectivity between immune cells mediated by tunneling nanotubules. Immunity, 2005. 23(3): p. 309-18.

22. Chinnery, H.R., E. Pearlman, and P.G. McMenamin, Cutting edge: Membrane nanotubes in vivo: a feature of MHC class II+ cells in the mouse cornea. J Immunol, 2008. 180(9): p. 5779-83.

23. Parr, A. M., Tator, C. H., & Keating, A. (2007). Bone marrow-derived mesenchymal stromal cells for the repair of central nervous system injury. *Bone Marrow Transplantation*, *40*(7), 609–619. doi: 10.1038/sj.bmt.1705757

24. Wang, X. and H.H. Gerdes, Transfer of mitochondria via tunneling nanotubes rescues apoptotic PC12 cells. Cell Death Differ, 2015. 22(7): p. 1181-91.

25. Yasuda, K., et al., Tunneling nanotubes mediate rescue of prematurely senescent endothelial cells by endothelial progenitors: exchange of lysosomal pool. Aging (Albany NY), 2011. 3(6): p. 597-608.
83.

26. Gousset, K., et al., Prions hijack tunnelling nanotubes for intercellular spread. Nat Cell Biol, 2009. 11(3): p. 328-36.

27. Rocca, C. J., Goodman, S. M., Dulin, J. N., Haquang, J. H., Gertsman, I., Blondelle, J., … Cherqui, S. (2017). Transplantation of wild-type mouse hematopoietic stem and progenitor cells ameliorates deficits in a mouse model of Friedreich's ataxia. *Science Translational Medicine*, *9*(413). doi: 10.1126/scitranslmed.aaj2347

28. Gabriel, S. S., Belge, H., Gassama, A., Debaix, H., Luciani, A., Fehr, T., & Devuyst, O. (2017). Bone marrow transplantation improves proximal tubule dysfunction in a mouse model of Dent disease. *Kidney International*, *91*(4), 842–855. doi: 10.1016/j.kint.2016.11.016

29. Delatycki, M. B., & Bidichandani, S. I. (2019). Friedreich ataxia- pathogenesis and implications for therapies. *Neurobiology of Disease*, *132*, 104606. doi: 10.1016/j.nbd.2019.104606

30. Mcwhorter, F. Y., Wang, T., Nguyen, P., Chung, T., & Liu, W. F. (2013). Modulation of macrophage phenotype by cell shape. *Proceedings of the National Academy of Sciences*, *110*(43), 17253–17258. doi: 10.1073/pnas.1308887110

31. Aflaki, E., Balenga, N. A. B., Luschnig-Schratl, P., Wolinski, H., Povoden, S., Chandak, P. G., … Kratky, D. (2011). Impaired Rho GTPase activation abrogates cell polarization and migration in macrophages with defective lipolysis. *Cellular and Molecular Life Sciences*, *68*(23), 3933–3947. doi: 10.1007/s00018-011-0688-4

32. Kimura, S., K. Hase, and H. Ohno, *The molecular basis of induction and formation of tunneling nanotubes.* Cell Tissue Res, 2013. **352**(1): p. 67-76.

33. Ma, A.D. and C.S. Abrams, Pleckstrin induces cytoskeletal reorganization via a Rac-dependent pathway. J Biol Chem, 1999. 274(40): p. 28730-5.

34. Ma, A.D., L.F. Brass, and C.S. Abrams, Pleckstrin associates with plasma membranes and induces the formation of membrane projections: requirements for phosphorylation and the NH2-terminal PH domain. J Cell Biol, 1997. 136(5): p. 1071-9.

35. Dohil, R., Carrigg, A. & Newbury, R. A potential new method to estimate tissue cystine content in nephropathic cystinosis. J Pediatr 161, 531-535 e531, doi:10.1016/j.jpeds.2012.03.011 (2012).

36. Rocca, C. J., Rainaldi, J. N., Sharma, J., Shi, Y., Haquang, J. H., Luebeck, J., … Cherqui, S. (2020). CRISPR-Cas9 Gene Editing of Hematopoietic Stem Cells from Patients with Friedreich's Ataxia. Molecular Therapy - Methods & Clinical Development, 17, 1026–1036. doi: 10.1016/j.omtm.2020.04.018

Chapter 2: HSPC Transplantation for Friedreich's ataxia

The following Chapter 2 is a reprint, in full, of material that appears in *Science Translational Medicine* on October 25, 2017.

2.1: Introduction

Friedreich's ataxia (FRDA) is a multisystemic autosomal recessive disease predominantly caused by GAA-repeat hyperexpansion within the first intron of the frataxin gene (FXN) (1). Long GAA repeats cause reduced expression of frataxin, a highly conserved mitochondrial protein mainly expressed in mitochondria-rich tissues including the nervous system, muscle, and heart (2). Although its function is not fully elucidated, frataxin is known to be an iron-binding protein participating in Fe-S cluster assembly. In the absence of frataxin, iron accumulates within mitochondria, leading to defective iron-mediated biosynthetic processes and increased oxidative stress (3–5). Pathologically, frataxin insufficiency leads to spinocerebellar neurodegeneration, ataxia, muscle weakness, and cardiomyopathy (1, 6). The primary pathological cause of the neuropathy is the loss of large sensory neurons in the dorsal root ganglia (DRGs), particularly in the lumbar region (7, 8), and the atrophy of dentate nuclei in the cerebellum (9). The transgenic YG8R mouse model, which exclusively expresses two mutant human FXN transgenes (hFXN) containing GAA expansions, develops progressive neurological degeneration with locomotor and coordination deficits and muscle weakness (10). Among transgenic FRDA mouse models expressing human FXN with expanded repeats, YG8R is the most severe model exhibiting substantial coordination and locomotor deficits by 3 months of age (11, 12).

Human hematopoietic stem and progenitor cells (HSPCs) from the bone marrow are ideal candidates for use in regenerative medicine and cell replacement therapy because of their ease of isolation, self-renewal capacity, and safety. Although the ability of HSPC transplantation to rescue

nonhematopoietic tissue remains contentious, we previously demonstrated that a single systemic transplant of wild-type mouse HSPCs led to long-term kidney, eye, and thyroid preservation in a mouse model of the multisystemic lysosomal storage disorder cystinosis (13–16). In this mouse model, the disease phenotype was rescued by the differentiation of wild-type HSPCs into macrophages that delivered lysosomes bearing functional cystinosin into diseased host cells potentially through long tubular extensions known as tunneling nanotubes (17). Tunneling nanotubes have been described as an intercellular delivery route for chemical mediators, proteins, and organelles such as lysosomes and mitochondria (18–20). We hypothesized that transplantation of wildtype mouse HSPCs could provide a delivery vehicle for functional frataxin and thereby alleviate disease progression in a mouse model of FRDA in which the mice express the mutant human frataxin (FXN) gene. Here, we report that wild-type mouse HSPC transplantation into young YG8R mice rescued many aspects of the FRDA phenotype including coordination and locomotion deficits and vacuolar degeneration of DRG neurons.

2.2: Results

Transplantation of wild-type mouse HSPCs prevents the onset of severe locomotor deficits in YG8R mice. To investigate the potential of wild-type mouse HSPC transplantation for treating FRDA, we intravenously injected lethally irradiated 2-monthold YG8R (mfxn−/− hFXN+) mice with wild-type green fluorescent protein (GFP)–expressing or DsRed-expressing Sca1+ mouse HSPCs (n = 13). Donor-derived HSPC engraftment ranged from 35 to 96% (expressed as a percentage of GFP-positive white blood cells in peripheral blood) (Supplemental File 1, table S1). As controls, we analyzed wild-type YG8R littermates (n = 16), nontransplanted YG8R littermates (n = 4), or lethally irradiated YG8R mice transplanted with YG8R (mfxn−/− hFXN+) HSPCs (n = 5). YG8R mice exhibited a progressive decrease in locomotor activity and coordination deficits by 3 months of age (10, 12). Thus, we assessed sensory function, motor function, and muscle strength for each group at both 5 and 9 months of age (3 and 7 months after transplantation, respectively). No difference in performance was observed in any of the behavioral tests at either time point between nontransplanted YG8R mice and those transplanted with mfxn−/− hFXN+ (control) HSPCs (Fig. 2.1A), indicating that neither irradiation nor transplantation with mfxn−/− hFXN+ HSPCs ameliorated the disease phenotype. Compared to wild-type mice, YG8R mice and those transplanted with mfxn−/− hFXN+ (control) HSPCs displayed reduced open-field locomotor activity, impaired coordination in the rotarod test, and alterations in gait, as well as decreased forelimb grip strength at both time points (Fig. 2.1A), consistent with previous reports (10, 12). In contrast, YG8R mice transplanted with wild-type mouse HSPCs exhibited normal locomotor activity and muscle strength at both 3 and 7 months after transplantation (Fig. 2.1A). Together, these data demonstrated that wild-type mouse HSPC transplantation in 2-month-old YG8R mice rescued the progressive neurobehavioral and muscular

deficits characteristic of this FRDA animal model. In contrast to our previous findings in a cystinosis model (14, 16), the YG8R mouse exhibiting the lowest percentage of donor-derived cell engraftment (35%; Supplemental File 1, table S1) still exhibited physiological rescue of the behavioral deficits (Supplemental File 1,table S2).

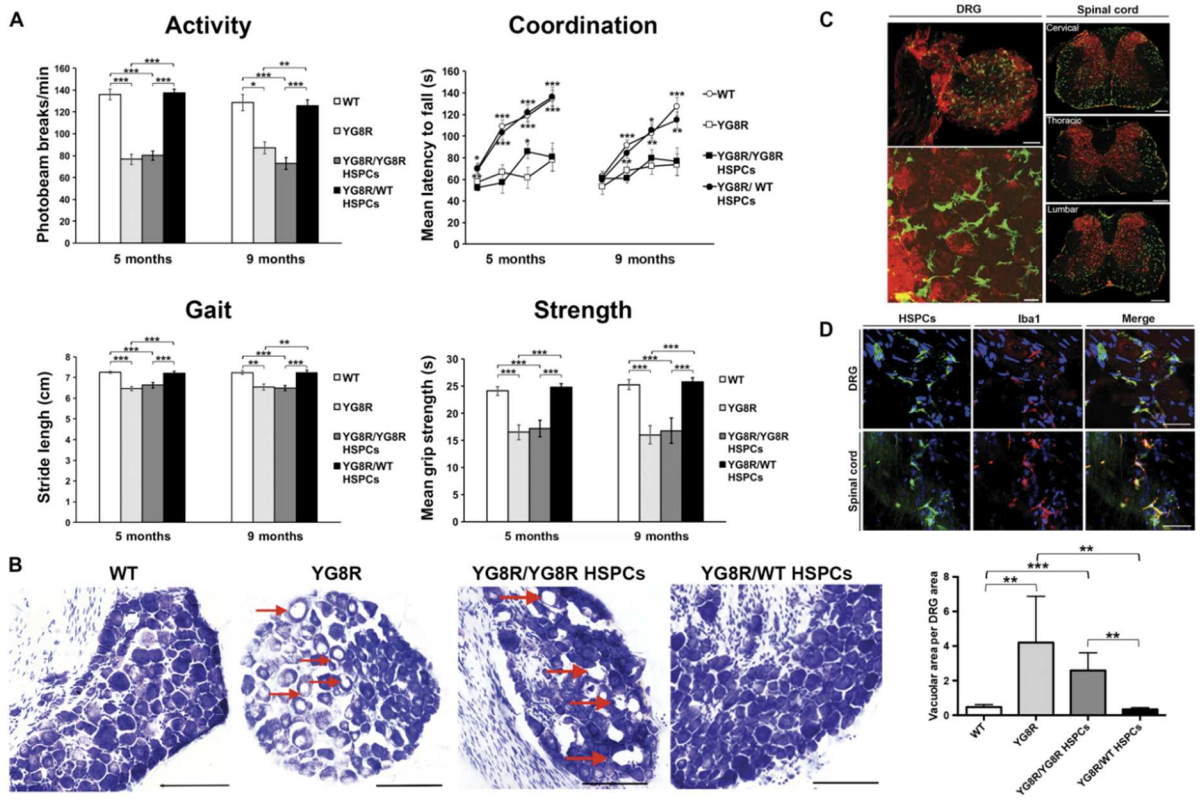

Figure 2.1: Neurobehavioral testing in YG8R mice transplanted with WT mouse HSPCs. (A) Neurobehavioral testing (open field, rotarod, gait, and grip strength) was performed for wild-type (WT) mice (n = 16), nontransplanted YG8R control mice (YG8R; n = 4), YG8R mice transplanted with YG8R mfxn−/− hFXN+ HSPCs (YG8R/ YG8R HSPCs; n = 5), and YG8R mice transplanted with wild-type HSPCs (YG8R/WT HSPCs; n = 13) at both 5 and 9 months of age. Locomotor activity was tested using an open-field test, coordination was tested using a rotarod test, gait was tested using an automated gait analysis system, and muscle strength was tested using a forelimb grip strength test. Data are means ± SEM. *P < 0.05, **P < 0.005 and ***P < 0.0005. For statistical comparison of three experimental groups, a mixed analysis of variance (ANOVA) with age of testing as a within-subjects variable was used, followed by independent sample t test. (B) Nissl-stained sections of the lumbar DRGs (L5) from representative 9-month-old wild-type mice (n = 15), YG8R control mice (n = 4), YG8R/YG8R HSPCs (n = 4), and YG8R/WT HSPCs (n = 11). Large vacuoles are shown by red arrows. Scale bars, 100 mm. Graph depicts total vacuolar area per DRG area (right). Data are means ± SEM. **P < 0.005 and ***P < 0.0005 (Mann-Whitney nonparametric test corrected for multiple testing by the Bonferroni correction). (C) Representative confocal images from a WT GFP+ HSPC-transplanted YG8R mouse 7 months after transplantation, stained with anti-GFP (green) and anti-NeuN (red) antibodies. Left: Image of a DRG. Scale bar, 100 mm (top). Magnified image with scale bar, 20 mm (below). Right: Images of cervical, thoracic, and lumbar spinal cord. Scale bars, 250 mm. (D) Confocal images of the DRG and spinal cord from a YG8R mouse transplanted with GFP+ HSPCs show engrafted cells (GFP; green) with neurons (NeuN; blue) and the Iba1 microglial marker (red). Scale bars, 30 mm.

Wild-type mouse HSPC transplantation prevents the degeneration of large sensory neurons in YG8R mice Neuropathology in FRDA results, in part, from degeneration of large sensory neurons in DRGs (8), causing the formation of large vacuoles within the lumbar DRGs of YG8R mice (10). Vacuolar accumulation in lumbar level 5 (L5) DRG neurons was detected in 9-month-old YG8R control mice with no significant difference in vacuolar area between nontransplanted and mfxn−/− hFXN+ HSPC-transplanted YG8R mice ($P = 0.5408$; Fig. 2.1B). In contrast, YG8R mice transplanted with wildtype mouse HSPCs exhibited a significant reduction in vacuolar area that was comparable to that of wild-type mice ($P < 0.005$; Fig. 2.1B).

Wild-type mouse HSPCs differentiate into phagocytic cells after engraftment in the mouse nervous system. Given that FRDA affects the central nervous system (CNS) in addition to peripheral sensory neurons (8), we next investigated the engraftment and differentiation of wild-type mouse HSPCs in different regions of the YG8R mouse nervous system. We found substantial engraftment of GFP+ HSPC-derived cells within the DRGs, spinal cord, and peripheral nerves, and as expected, most of the neurons appeared to be myelinated (Fig. 2.1C and Supplemental File 1, fig. S1). Within the DRGs in all spinal cord regions, donor cells were found in close proximity to neurons and were immunoreactive for the macrophage markers CD68 and major histocompatibility complex class II (MHCII), as well as Iba1, characterizing these cells as DRG-resident macrophages (Fig. 2.1, C and D, and Supplemental File 1, fig. S2, A and B) (21). In the spinal cord of the recipient YG8R mice, HSPC-derived cells were abundant in the ascending sensory axon tracts, within the dorsal and ventral roots, motor neuron pools, and dorsal spinal cord gray matter (Fig. 2.1, C and D). These cells were >99% Iba1+ and CD68+ , whereas fewer cells expressed MHCII (~30%; Supplemental File 1, fig. S2, A to C), indicating their microglial identity (22, 23). Three-dimensional (3D) visualization of the engrafted spinal cord that was subjected to

tissue clearing showed that a high concentration of engrafted HSPC-derived cells was found in close proximity to perivascular regions, suggesting that these cells may have infiltrated the CNS via the vasculature. Graft-derived cells were also detected throughout the gray and white matter in the brain, brainstem, and cerebellum of transplanted YG8R mice (Fig. 2.2A). The vast majority (>99%) of HSPC-derived cells within all regions of the brain displayed the typical ramified morphology of microglia and expressed CD68 and Iba1 but were not immunoreactive for MHCII, demonstrating that these cells were microglial cells (Fig. 2.2B and Supplemental File 1, fig. S2, A, B, and D) (24). Perivascular infiltration in the brain was further demonstrated by the presence of GFP+ HSPC-derived cells in close proximity to blood vessels (Supplemental File 1, fig. S2E), especially in the highly vascularized choroid plexus (Supplemental File 1, fig. S2F), as previously described (25).

Wild-type mouse HSPC transplantation restores frataxin expression and normalizes mitochondrial function in the brains of YG8R mice. Analysis of murine frataxin (mFxn) expression in the mouse brain confirmed that tissue engraftment of the HSPC-derived cells correlated with partial restoration of mFxn expression in transplanted mice compared to nontransplanted YG8R control mice, although mFxn expression did not reach that of wild-type animals. Residual expression of mFxn was also detected in YG8R mice, most likely because of crossreactivity of the quantitative polymerase chain reaction (PCR) primers with human FXN (Fig. 2.2C). Mitochondrial dysfunction in FRDA is associated with an increase in oxidized proteins within tissues (10, 26). Compared to wild-type control mice, oxidized proteins were significantly higher ($P < 0.05$) in the cerebrum of YG8R mice and those transplanted with mfxn−/− hFXN+HSPCs (Fig. 2.2D).

In addition, mitochondrial function was assessed using mitochondrial PCR array profiling (27) in the cerebrum of wild-type, YG8R, and HSPC-transplanted YG8R mice. Expression of mitochondrial genes crucial for a wide variety of processes ranging from control of apoptosis to oxidative phosphorylation was altered in the YG8R animals. Of the 89 genes tested, 15.7% showed an increase of at least twofold over wild-type mice, whereas only 4.4% of the genes were up-regulated in transplanted YG8R mice (Fig. 2.2E). Of these genes, five were significantly up-regulated in YG8R mice compared to wild-type animals, including several members of the solute carrier family of inner mitochondrial membrane transporters and other proteins involved in mitochondrial lipid metabolism ($P < 0.05$; Fig. 2.2E). No significant differences were observed between YG8R mice transplanted with wild-type mouse HSPCs and wild-type animals (Fig. 2.2E).

Figure 2.2. Transplanted WT mouse HSPCs engraft throughout the YG8R mouse brain. (A) Representative transverse section of the brain of a YG8R mouse 7 months after transplantation with wild-type mouse GFP+ HSPCs, labeled with anti-GFP (green) and anti-NeuN (red) antibodies. Scale bar, 1 mm. Magnified image #1 of the brain shows the periventricular regions including the corpus callosum (cc), lateral septal nuclei (LS), caudate putamen (CP), anterior cingulate area (ACA), and the somatosensory cortex (M1 and S2). VL, lateral ventricle. Scale bar, 150 mm. Magnified image #2 of the mouse brain shows the ventral striatum including the anterior commissure (aco), nucleus accumbens (ACB), lateral septal nuclei, and caudate putamen. Scale bar, 150 mm. Magnified image #3 shows the ventral pallidum (PAL) and the ventral striatum, including the islands of Calleja (isl) and the olfactory tubercle (OT). Scale bar, 150 mm. Lower panels depict the gray and white matter of the brain stem and cerebellum. Scale bar, 500 mm. Insets magnify the dentate nucleus (DN) of the cerebellum and the spinal trigeminal nucleus (Sp) of the brain stem. Scale bar, 50 mm. (B) Confocal images of YG8R mouse brain labeled with anti-GFP (green), anti-Iba1 (red), and anti-NeuN (blue) antibodies. Scale bar, 30 mm. (C) Quantification of murine frataxin mRNA expression in the cerebellum from wild-type mice (n = 14), YG8R mice (n = 8), and YG8R mice transplanted with wild-type mouse HSPCs (n = 13). Data are represented as fold change relative to wild type normalized to glyceraldehyde-3-phosphate dehydrogenase (GAPDH). Data are means ± SEM. **P < 0.005 and ***P < 0.0005 (one-way ANOVA, followed by post hoc Student'st test). (D) Representative Western blot showing protein oxidation in the cerebrum from one wild-type mouse, one YG8R nontransplanted mouse, one YG8R mouse transplanted with YG8R HSPCs (YG8R/YG8R HSPCs), and one YG8R mouse transplanted with wild-type HSPCs (YG8R/WT HSPCs), with (+) or without (−) a 2,4-dinitrophenylhydrazine (DNP) derivatization reagent. Cerebrum tissue from 9-month-old YG8R control mice (n = 4) and YG8R/YG8R HSPC mice (n = 4) was compared to that from wild-type mice (n = 6) and YG8R/WT HSPCs (n = 6). Data are means ± SEM. *P < 0.05 (one-tailed t test). Tub, tubulin; a.u., arbitrary units. (E) Scatterplots of mitochondrial gene expression changes in the cerebrum (n = 3) from wild-type animals compared to YG8R nontransplanted control mice (left) or YG8R/WT HSPCs mice (middle). The center line represents no change in gene expression, and up-regulated and down-regulated genes at a fold change of 2 or greater are noted by yellow and blue dots, respectively. mRNA changes that are significantly different between groups are represented on a separate bar graph (right). Data are means ± SEM. *P < 0.05, **P < 0.005, ***P < 0.0005, compared to wild-type mice (one-way ANOVA, followed by post hoc Student's t test).

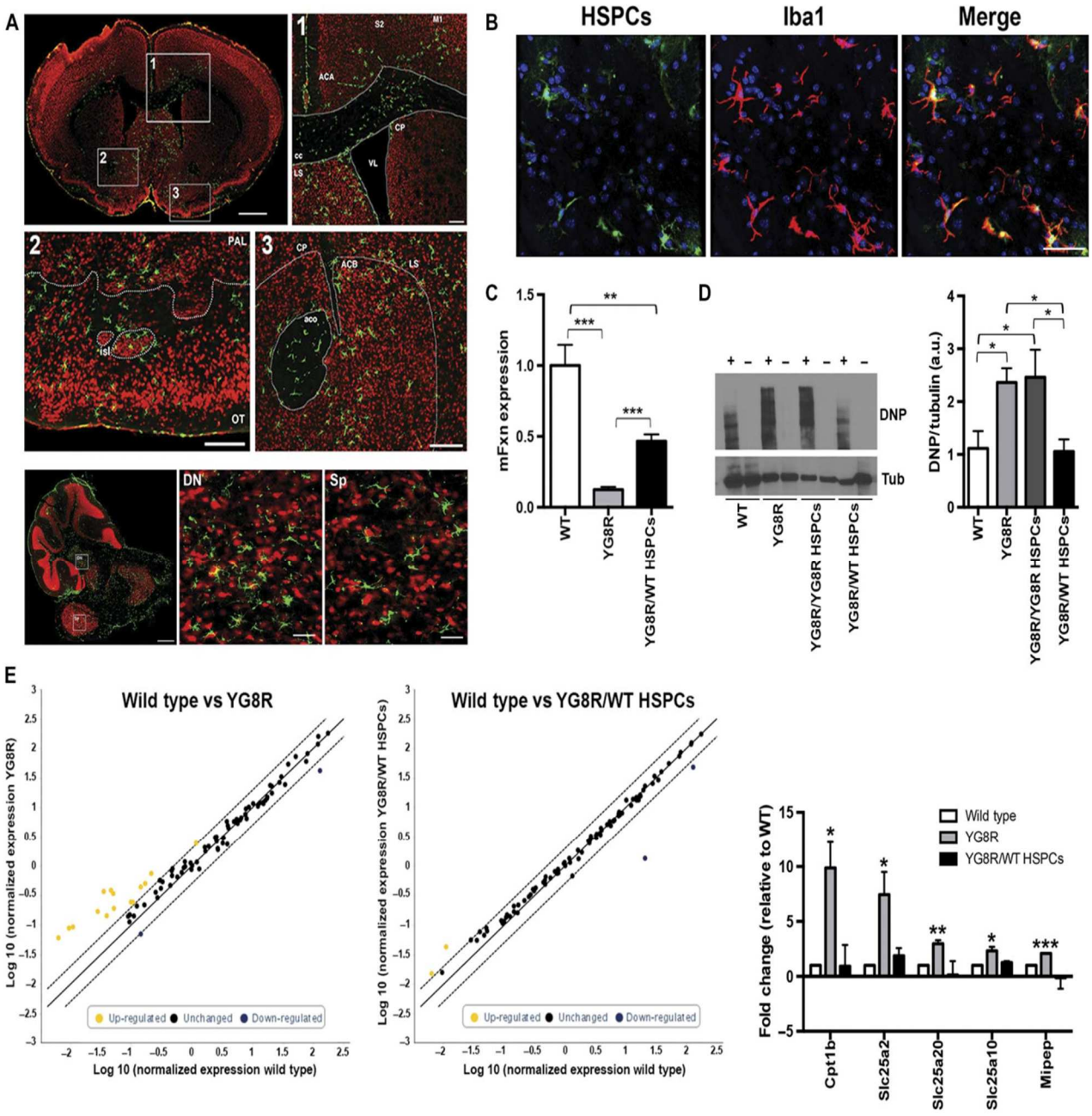

Wild-type mouse HSPCs are engrafted in the YG8R mouse heart and muscle, reducing iron deposition and decreasing skeletal muscle atrophy. An increase in oxidized proteins was also demonstrated in the skeletal muscle of YG8R control mice relative to wild-type mice, although this was not significant; normal amounts of oxidized proteins were found in the skeletal muscle of transplanted YG8R mice (P = 0.0798; Fig. 2.3A). Furthermore, in skeletal

muscle biopsies, we quantified by mass spectrometry lactate and pyruvate, metabolites that have been shown to be elevated in some mitochondrial diseases (28). There was a significant increase in the lactate-to-pyruvate ratio in the skeletal muscle of YG8R mice compared to wild-type mice ($P < 0.0005$), which was corrected in the HSPC-transplanted YG8R animals (Fig. 2.3B).

In addition to neurological deficits, FRDA patients also develop a progressive hypertrophic cardiomyopathy (29, 30). Thus, we investigated the potential impact of HSPC transplantation on heart pathology in YG8R mice. However, cardiomyopathy is very mild in this mouse model (10), and no phenotype was found in the YG8R mice compared to wild-type mice at 9 months of age (Supplemental File 1, fig. S3A). Evidence of cellular iron metabolic dysregulation in the form of iron deposition in cardiomyocytes has been observed in FRDA patients (31) and in 14- to 18-monthold YG22 mice (another FRDA mouse model expressing one copy of the mutated human frataxin gene) (10, 32). We observed iron deposition in mouse cardiomyocytes, as revealed by Perl's staining of heart sections from 18-month-old nontransplanted YG8R mice; this deposition was significantly decreased in YG8R mice transplanted with wildtype mouse HSPCs ($P = 0.042$; Fig. 2.3C).

In both heart and skeletal muscle tissues, mFxn expression was increased in the wild-type HSPC-transplanted mice compared to YG8R control mice (Fig. 2.3, D and E). Confocal microscopy analysis revealed large numbers of GFP+ cells engrafted in these tissues in HSPC transplanted YG8R animals (Fig. 2.3, F and G). The engrafted GFP+ cells expressed CD68 and MHCII (Supplemental File 1, fig. S3, Band C), indicating that these cells were macrophages.

To investigate potential muscular atrophy in YG8R mice, we measured the expression of two muscle-specific E3 ubiquitin ligases, muscle RING finger 1 (MuRF-1) and muscle atrophy F-box/atrogin-1, and a member of the transforming growth factor–b superfamily, myostatin, which

are all increased during skeletal muscle atrophy (33, 34). Expression of MuRF-1, atrogin-1, and myostatin was increased in the skeletal muscle from YG8R mice compared to wild-type mice (although this was not significant for atrogin-1). In contrast, expression of these three muscle proteins was normal in the transplanted YG8R mice (Fig. 2.3H), demonstrating the rescue of this defect by transplantation of wildtype mouse HSPCs.

Figure 2.3. Transplanted wild-type mouse HSPCs are engrafted in the heart and muscle of YG8R recipient mice. (A) Representative Western blot showing protein oxidation in the skeletal muscle of one wild-type mouse, one YG8R control mouse (YG8R), and one YG8R mouse transplanted with wild-type mouse HSPCs (YGR8/WT HSPCs), with (+) or without (−) a 2,4-dinitrophenylhydrazine derivatization reagent. Nine-month-old YG8R control mice [which included nontransplanted YG8R mice (n = 4) and YG8R mice transplanted with YG8R HSPCs (n = 5)] were compared to wild-type mice (n = 16) and YG8R mice transplanted with wild-type mouse HSPCs (YG8R/WT HSPCs; n = 13). Error bars indicate SEM. *P < 0.05. NS, statistically nonsignificant (one-tailed t test). (B) Quantification of lactate and pyruvate by mass spectrometry (represented as a ratio) in muscle tissues from wild-type mice (n = 6), YG8R nontransplanted control mice (n = 3), and YG8R mice transplanted with wild-type mouse HSPCs (n = 5). Error bars indicate SEM. *P < 0.05 and ***P < 0.0005 (one-way ANOVA, followed by post hoc Student's t test). (C) Representative Perl's staining of heart sections from an 18-monthold wild-type mouse, YG8R nontransplanted mouse, and YG8R mouse transplanted with wild-type HSPCs; blue staining indicates iron deposition. Scale bars, 50 and 15 mm (inset). The associated bar graph shows iron quantification in heart sections from wild-type mice (n = 4), YG8R control mice [nontransplanted (n = 2) and YG8R mice transplanted with YG8R HSPCs (n = 2)], and YG8R mice transplanted with wild-type mouse HSPCs (n = 3). Error bars indicate SEM. *P < 0.05 (one-way ANOVA, followed by post hoc Student's t test). (D and E) Quantification of murine frataxin mRNA expression in the heart (D) and skeletal muscle (E) from wild-type mice (n = 12), YG8R nontransplanted control mice (YG8R; n = 7), and YG8R mice transplanted with wild-type mouse HSPCs (YG8R/WT HSPCs; n = 11). Data are represented as fold change relative to wild-type normalized to GAPDH; error bars indicate SEM. *P < 0.05, **P < 0.005, ***P < 0.0005 (one-way ANOVA, followed by post hoc Student's t test). (F) Heart section from a YG8R mouse 7 months after transplantation with wild-type mouse HSPCs, stained with anti-GFP (green) antibody, the cardiomyocyte marker anti–a-actinin (magenta) antibody, and 4′,6-diamidino-2-phenylindole (DAPI) nuclear stain (blue). Scale bar, 150 mm. Magnified images on the right show the left ventricle (bottom) and the base of the aorta (top). Scale bars, 50 mm. (G) Skeletal muscle section from a YG8R mouse 7 months after transplantation with wild-type mouse HSPCs, stained with anti-GFP (green) antibody, filamentous actin dye phalloidin (magenta) antibody, and DAPI nuclear stain (blue). Scale bar, 150 mm. Magnified image of the skeletal muscle (inset). Scale bar, 50 mm. (H) Quantification of murine MuRF-1, atrogin-1, and myostatin mRNA expression in the skeletal muscle from wild-type mice (n = 5), YG8R nontransplanted control mice (n = 5), and YG8R mice transplanted with wild-type mouse HSPCs (n = 5). Data are represented as fold change relative to wild-type normalized to GAPDH; error bars indicate SEM. *P < 0.05 (one-way ANOVA, followed by post hoc Student's t test).

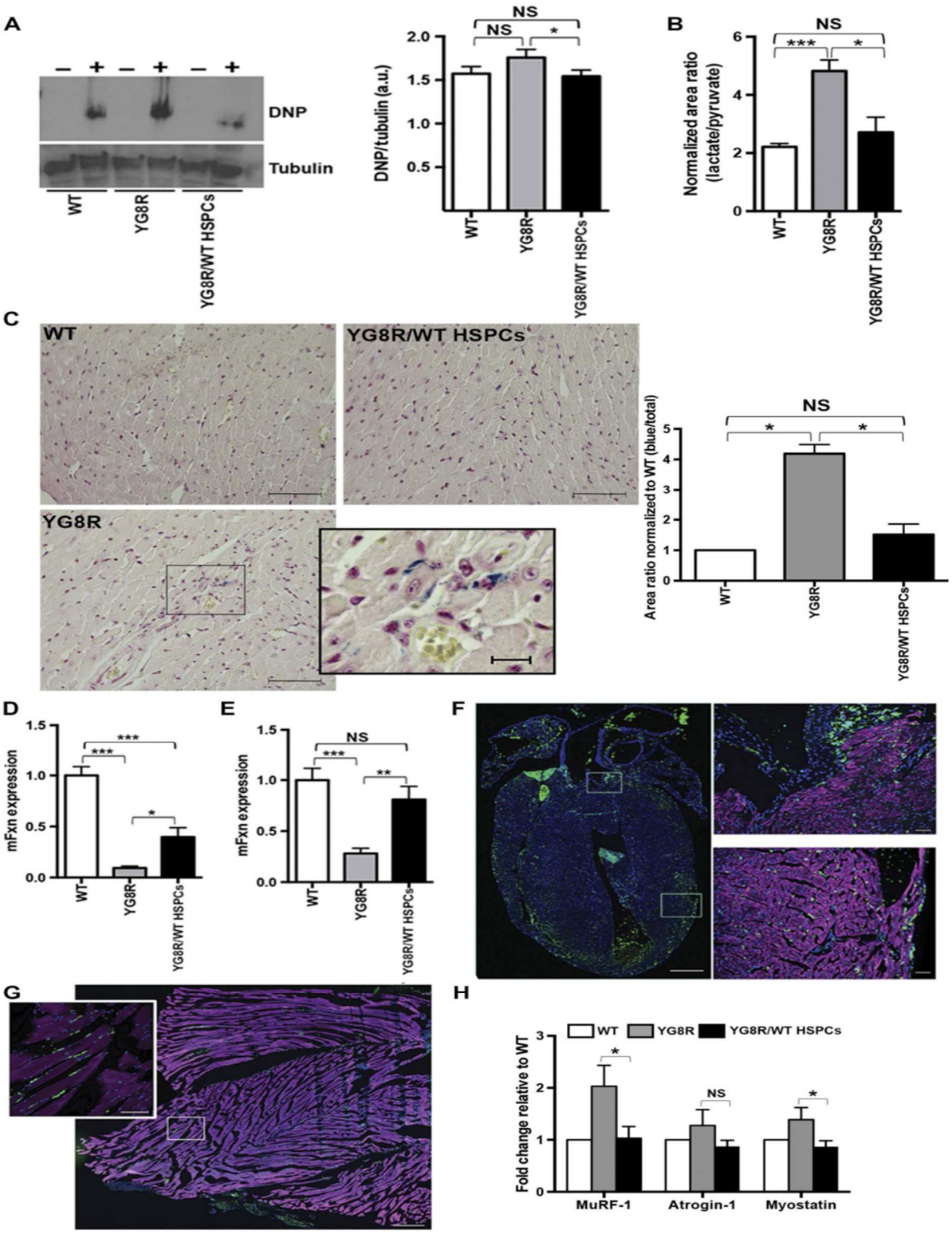
A
DNP
Tubulin
WT
YG8R
YG8R/WT HSPCs
NS
NS
*
DNP/tubulin (a.u.)
B
NS
***
*
Normalized area ratio (lactate/pyruvate)
C
WT
YG8R/WT HSPCs
YG8R
NS
*
*
Area ratio normalized to WT (blue/total)
D
***
***
*
mFxn expression
E
NS
***
**
mFxn expression
F
G
H
WT
YG8R
YG8R/WT HSPCs
*
NS
*
Fold change relative to WT
MuRF-1
Atrogin-1
Myostatin

Macrophages deliver frataxin to YG8R mouse fibroblasts. We previously reported that in the lysosomal storage disorder cystinosis, mouse HSPC-derived macrophages promote functional rescue of diseased cells through a lysosomal corrective mechanism (17). Hence, we asked whether phagocytic cells could also mediate the transfer of frataxin into mfxn−/− hFXN+ mouse fibroblasts in vitro. We cocultured fibroblasts harvested from YG8R mouse neonatal skin with macrophages isolated from the bone marrow of cytochrome c oxidase subunit VIII (Cox8)–GFP DsRed mice that ubiquitously expressed the mitochondrial Cox8 protein fused to GFP and the cytosolic DsRed reporter (35, 36). Using live imaging, we observed that theCox8-GFP protein was transferred from the DsRed-expressing macrophages to the mfxn−/− hFXN+ fibroblasts (Fig. 2.4A). In parallel, we used macrophages stably transduced with a lentiviral vector (LV) containing the human mitochondrial frataxin gene tagged with GFP (LV-hFXN-GFP). Mitochondria were then labeled with MitoTracker Red in the coculture assay. Movement of hFXN-GFP–bearing mitochondria was observed from the macrophages to the diseased fibroblasts, and hFXN-GFP could be observed in the recipient FRDA mouse fibroblasts (Fig. 2.4B).

Wild-type mouse HSPC-derived microglia and macrophages transfer mitochondrial proteins to YG8R mouse neurons in vivo. To assess whether transfer of mitochondrial proteins occurred in vivo, we transplanted YG8R mice with HPSCs isolated from DsRed Cox8- GFP mice. Cox8-GFP punctae were detected not only within the DsRed-expressing microglial cells but also within neurons in the YG8R mouse brain, spinal cord, and DRGs (Fig. 2.4C and Supplemental File 1, fig. S4). We typically observed that neurons containing Cox8-GFP were in contact with one or more DsRed+ microglial branch extensions (Fig. 2.4C), and GFP+ punctae were also observed within these microglial processes (Fig. 2.4D). Quantification in spinal cord tissue revealed that about 50% of neurons contained Cox8-GFP staining (see Fig. 2.4E and Supplemental

File 1, fig. S5 for quantification methodology). Transfer of frataxin from microglia to neurons was also demonstrated by transplanting YG8R mice with HSPCs isolated from DsRed transgenic mice and stably transduced with LVhFXN-GFP (Fig. 2.4F). In addition, evidence of transfer was apparent in the heart and skeletal muscle, in which Cox8-GFP was detected in recipient mouse muscle myocytes that were next to graft-derived macrophages (Supplemental File 1, fig. S4B). Together, these results suggest that mitochondrial protein transfer occurs from microglia to neuronal cells and that this transfer may be involved in HSPC-mediated rescue of the FRDA phenotype in the YG8R mouse model.

Figure 2.4. Wild-type mouse HSPC-derived cells deliver frataxin and Cox8 to FRDA cells in vitro and in vivo. (A and B) Representative frames from confocal imaging movies of YG8R mouse fibroblasts (F) cocultured with (A) primary macrophages (M) isolated from a DsRed Cox8-GFP transgenic mouse (video S2) or (B) IC-21 macrophages transduced with LV-hFXN-GFP and stained with a MitoTracker Red (video S3). Scale bars, 10 mm. (C) Representative confocal images of brain sections from a YG8R mouse transplanted with DsRed+ HSPCs (control; see video S4) and those of brain and spinal cord sections from a YG8R mouse transplanted withDsRed+ /Cox8-GFP+HSPCs at 7 months after transplantation, labeled with an anti-NeuN antibody (blue) (see fig. S4 for the DRG, heart, and muscle). White arrows depict Cox8-GFP in recipient mouse neurons in the brain and spinal cord (see videos S5 and S6 for 3D visualization). Scale bars, 10 mm. (D) Representative confocal images of a spinal cord section from a YG8R mouse transplanted with DsRed+ /Cox8-GFP+ HSPCs at 7 months after transplantation, labeled with an anti-NeuN antibody (blue). White arrows depict Cox8-GFP within branch extensions of the DsRed+ microglial cell. Scale bar, 5 mm. (E) Quantification of neurons containing Cox8-GFP in the cervical spinal cord gray matter of YG8R mice transplanted with DsRed+ /Cox8-GFP+ HSPCs at 7 months after transplantation (see fig. S4 for the description of the automatic unbiased quantification method). (F) Representative confocal images of brain and spinal cord sections from a YG8R mouse transplanted with DsRed+ HSPCs transduced with LV-hFXN-GFP at 7 months after transplantation and stained with anti-mCherry (red) and anti-NeuN (blue) antibodies. Scale bars, 10 mm

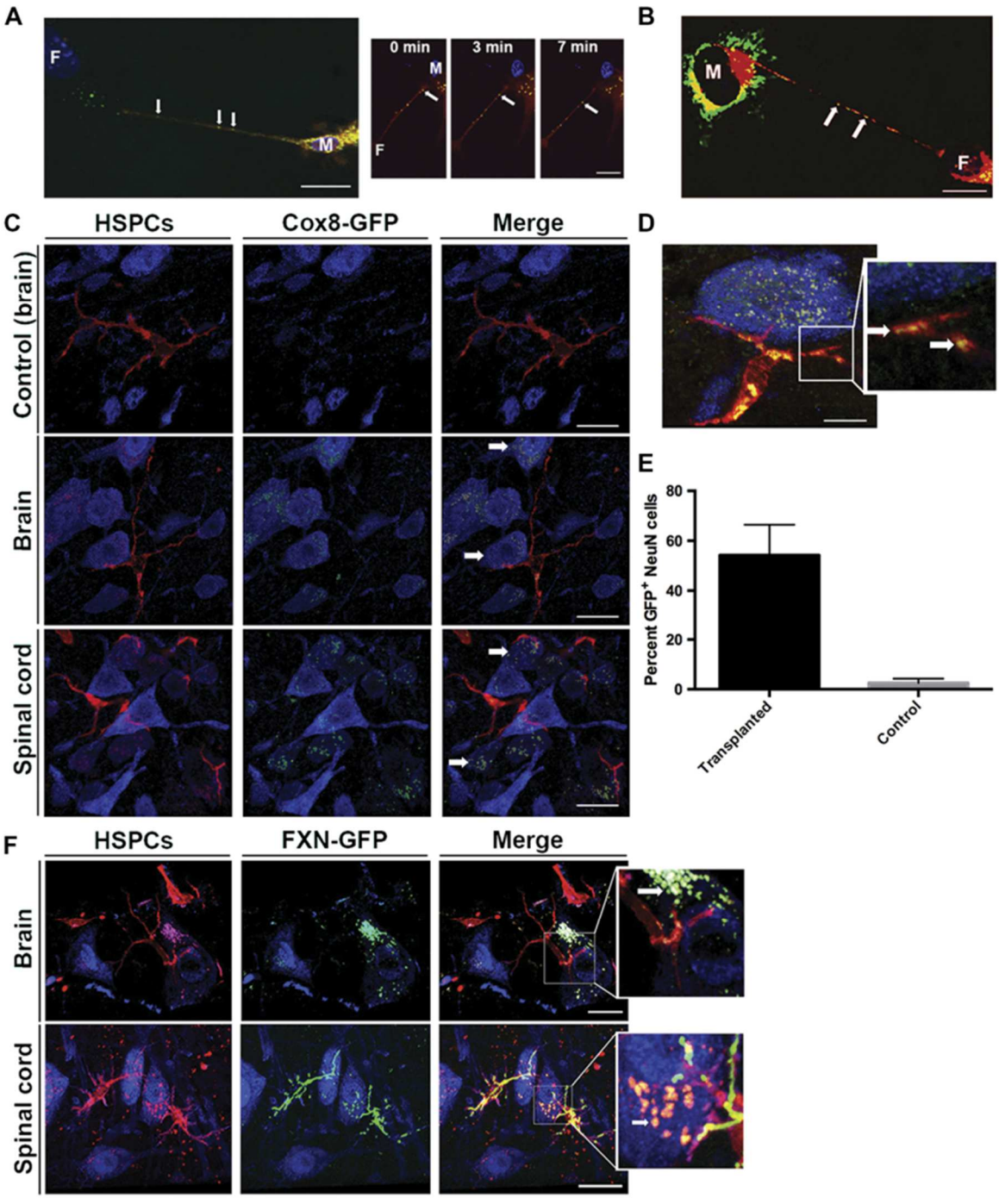
A
F
M
0 min
3 min
7 min
M
F
B
M
F
C
HSPCs
Cox8-GFP
Merge
Control (brain)
Brain
Spinal cord
D
E
Percent GFP+ NeuN cells
80
60
40
20
0
Transplanted
Control
F
HSPCs
FXN-GFP
Merge
Brain
Spinal cord

2.3: Discussion

There is a pressing need to identify effective therapies for FRDA, a debilitating neurodegenerative disease for which there remains no treatment. To date, preclinical studies using stem cells or gene therapy have had limited success or have been restricted to assessment of improvements in specific tissues (29, 37–39). A recent in vivo study reported the prevention and reversal of severe cardiomyopathy in a skeletal muscle conditional frataxin-knockout mouse model after intravenous injection of AAV9 (adeno-associated virus serotype 9)–hFXN complementary DNA (cDNA) (29). Here, we demonstrated that a single transplant of wild-type mouse HSPCs into young adult YG8R mice prevented the development of FRDA pathology, including neurobehavioral deficits, muscle weakness, and degeneration of DRG sensory neurons. The key advantage of exogenous HSPC transplantation is the capacity of these cells to permanently repopulate the bone marrow and migrate from their niche to differentiate into phagocytic cell types within multiple tissues (17). HSPCs may even be able to transmigrate across the blood-brain barrier and engraft within the CNS as differentiated microglia (24, 25, 40, 41). This phenomenon is enhanced by tissue injury (24, 42, 43) or by using busulfan-mediated myeloablation instead of total body irradiation (44). We show that transplanted wild-type mouse HSPCs differentiated into microglial cells in the CNS of the YG8R recipient mice and into macrophages in the DRGs, peripheral nerves, skeletal muscle, and heart, the primary sites of FRDA pathology.

We showed a reduction in oxidative stress in HSPC-treated YG8R mouse tissues compared to that in tissues of YG8R nontransplanted mice or animals transplanted with YG8R HSPCs. Oxidative stress is a major component of FRDA pathogenesis and may account for neuronal degeneration (45). Oxidative stress has also recently been shown to induce DNA damage and elevation of poly(adenosine 5′-diphosphate–ribose) polymerase 1 (PARP1) expression in frataxin-

deficient microglial cells, which resulted in increased microglial activation (46). Because PARP1 activation leads to increased inflammatory cytokine expression in microglial cells (47), these findings suggest that oxidative stress may induce neuroinflammatory-mediated neurodegeneration in FRDA. Hence, the robust neurological phenotypic rescue we observed in HSPC-transplanted YG8R mice may be, in part, due to the replacement of the frataxin-deficient microglial cells by wild-type microglia. Mitochondrial function was assessed by mitochondrial PCR array profiling in the cerebrum of YG8R mice. Our findings showed a number of upregulated genes (>2-fold change) in YG8R mice compared to wild-type mice (13 of 84 genes). In contrast, very few changes in expression were identified between wild-type mice and HSPC-transplanted YG8R mice (four genes), and none was identified with a significant difference. Among the significantly up-regulated genes in YG8R mice versus wild-type mice, there were 25 genes from the solute mitochondrial carrier protein family ($P < 0.05$) (48), including Mipep, an important component of the human mitochondrial import machinery implicated in developmental delay (49), and the fatty acid transporter Cpt1b, which is up-regulated in posttraumatic stress disorder (50).

Cellular iron metabolism dysregulation was first demonstrated in FRDA by Lamarche and colleagues (31), who reported the presence of iron deposits in cardiomyocytes of patients. Here, we demonstrated the presence of abundant iron deposits in heart sections from nontransplanted YG8R control mice, whereas very few were observed in wildtype mice or YG8R mice transplanted with wild-type mouse HSPCs, suggesting that there was normal iron metabolism in the transplanted YG8R mice. In contrast, preclinical and clinical data using an iron chelator as a potential therapeutic agent showed a limited beneficial effect on some neurological functions but worsening of gait and posture (51).

We propose that a frataxin transfer mechanism is involved in FRDA phenotypic rescue after wild-type mouse HSPC transplantation to YG8R mice. After hFXN-GFP–expressing murine HSPC transplantation into YG8R mice, we observed the transfer of human frataxin-GFP from the mouse HSPC-derived microglia/macrophages to YG8R mouse neurons in the brain, spinal cord, and DRGs and to myocytes in the skeletal muscle and heart. We also demonstrated the transfer of the mitochondrial protein Cox8, suggesting nonselective transfer of mitochondrial proteins. This raises several questions that remain to be answered. First, are entire mitochondria transferred from donor phagocytic cells to neurons or is this transfer limited to mitochondrial proteins? Second, is the main route of transfer through vesicular exchange or intercellular membrane connections? We previously reported that HSPC-derived macrophages in recipient mouse kidney could deliver cystinosin-containing lysosomes to proximal tubular cells through tunneling nanotubes in a mouse model of cystinosis (17). In this context, tunneling nanotubes crossing the basement membrane of kidney tubular cells seemed to be the only route possible across the continuous, dense tubular basement membrane. The transfer of mitochondria through tunneling nanotubes has been previously shown in vitro in response to cellular stress (52). Here, we showed in vitro that frataxin and Cox8 mitochondrial proteins could be transferred from donor macrophages to frataxin-deficient fibroblasts. In vivo, we observed the mitochondrial proteins frataxin-GFP and Cox8-GFP within recipient YG8R mouse neurons, with about 50% of neurons containing Cox8-GFP in the spinal cord. There are several potential routes for this transfer, including vesicular exchange of genetic material (53), release of mitochondria-containing vesicles (54), or as shown recently, transfer from astrocytes to neurons in a cerebral ischemia mouse model (55). An alternative possibility is the microglia-to-neuron transfer of mitochondria through microglial branch extensions directly in contact with neurons. Microglial processes are dynamic, actively retracting

and expanding, and capable of making direct contact with neurons, especially during injury (56, 57).

There are two main limitations to our study. First, the mild delayed cardiac phenotype of YG8R mice fails to accurately reflect FRDA disease progression in human patients. Second, we were unable to demonstrate the route and mechanism of frataxin correction after transplantation in vivo. Further extensive studies with alternative animal models of FRDA will be required before definitive conclusions can be drawn.

Our findings demonstrate that a single infusion of wild-type mouse HSPCs into the YG8R FRDA mouse model resulted in the engraftment and differentiation of these cells into microglia/macrophages in the brain, spinal cord, DRGs, skeletal muscle, and heart, leading to the rescue of the disease phenotype. Our work suggests that this strategy could be a potential approach for treating FRDA.

2.4: Methods

Study design. The goals of this study were (i) to investigate whether wild-type mouse HSPC transplantation could prevent progressive deficits in the YG8R mouse model of FRDA, (ii) to determine whether wild-type mouse HSPC transplantation could prevent tissue damage caused by frataxin deficiency, and (iii) to investigate the mechanism by which HSPCderived cells participated in the rescue of the FRDA phenotype. We transplanted 13 2-month-old YG8R FRDA mice with wild-type mouse HSPCs and compared them to 16 wild-type mice and 4 nontransplanted YG8R FRDA mice. To ensure that neither irradiation nor transplantation was responsible for the improved phenotype observed in the transplanted mice, we also included five YG8R mice transplanted with mouse FRDA HSPCs. Two months after transplantation, we measured donor HSPC engraftment, which ranged between 35 and 96% engraftment. Neurobehavioral testing (open field, rotarod, gait, and grip strength) was performed for all the groups at 5 and 9 months of age by a behavioral core facility in a blinded fashion. Mice were euthanized at 9 months of age, and tissues were collected for cellular, molecular, and histological analyses.

Animals. YG8R mice with a deletion of murine Fxn gene (mFxn) and expressing a mutant human FXN gene (hFXN) containing 190 + 90 GAA-repeat expansion were generated in a C57BL/6J background, as previously described (10, 58). Breeding pairs consisted of females heterozygous for Fxn and males heterozygous for Fxn and hemizygous for FXN [B6. Cg-Fxntm1Mkn Tg(FXN)YG8Pook/J] and were purchased from the Jackson Laboratory. YG8R and wild-type mice used as controls for these studies were obtained from these breeders. Genotyping was performed using the following primers: mfxn, 5′-CTTCCCTCTACCCTGCCTTC3′ (forward) and 5′- GGAGAACAGTGGACACAGTAACA-3′ (reverse); PGK-NEO, 5′-

CATCGCCTTCTATCGCCTTCT-3′; FXN, 5′-GGGCAGATAAAGGAAGGAGATAC-3′ (forward) and 5′-ACGATAGGGCAACACCAATAA-3′ (reverse). Transgenic mice constitutively expressing GFP [C57BL/6- Tg(ACTB-EGFP)1Osb/J] or DsRed [B6.Cg-Tg(CAG-DsRed*MST) 1Nagy/J] were also purchased from the Jackson Laboratory. The mtGFP-Tg transgenic mice [C57BL/6J-Tg(CAG-Cox8/EGFP)49Rin] expressing the Cox8-GFP mitochondrial fusion protein (35, 36) were provided by the RIKEN BioResource Center through the National BioResource Project of the Ministry of Education, Culture, Sports, Science and Technology (MEXT). mtGFP-Tg mice were backcrossed with DsRed-Tg mice to produce DsRed-mtGFP-Tg mice. Genotyping for mtGFP was carried out by PCR, as previously described (36). Mice were maintained in a temperature- and humidity-controlled animal facility, with a 12-hour light/dark cycle and free access to water and food. Both male and female mice were used in all experiments. All mice were bred at the University of California, San Diego (UCSD) vivarium, and all protocols were approved by the UCSD Institutional Animal Care and Use Committee.

Frataxin-GFP lentivirus construction, production, and titer. The self-inactivating LV, pCCL-EFS-X-WPRE (pCCL)–GFP, was used for stable gene transfer in HSPCs and macrophages. The vector backbone contains the intron-less human elongation factor 1a promoter to drive transgene expression (59, 60). The human FXN cDNA (633 base pairs; clone ID 5300379, GE Healthcare) corresponding to the canonical frataxin (isoform I) found in mitochondria (61) was amplified by PCR using the primers 5′-TTAGGATCCATGTGGACTCTCG-3′(forward) and 5′-AGAGGATCCAGCATCTTTTCCG-3′ (reverse) and inserted into pCCL-GFP at the Bam HI restriction site in phase with the GFP cDNA. LV was produced and titered as previously described (62).

Bone marrow cell isolation, transduction, transplantation, and engraftment. Bone marrow cells were flushed from the femurs of 6- to 8-week-old YG8R, GFP transgenic, DsRed transgenic, or DsRed mtGFP transgenic mice. HSPCs were isolated by immunomagnetic separation using antiSca1 antibody conjugated to magnetic beads (Miltenyi Biotec). Sca1+ cells were directly transplanted by tail vein injection of 1 × 106 cells resuspended in 100 ml of phosphate-buffered saline (PBS) into lethally irradiated (7 gray; X-Rad 320, PXi) YG8R mice. Before transplantation, Sca1+ cells from the DsRed transgenic mice were first transduced with LV-hFXN-GFP using a multiplicity of infection (MOI) of 10 in the presence of polybrene (4 mg/ml) in RetroNectin-coated (20 g/ml) 24-well plates at a density of 2 × 106 cells per well for 16 hours in StemSpan medium (STEMCELL Technologies) supplemented with stem cell factor, thrombopoietin, FLT3 ligand (100 ng/ml each), and interleukin6 (20 ng/ml) cytokines (PeproTech). Bone marrow cell engraftment of the transplanted cells was measured in peripheral blood 2 months after transplantation; blood samples freshly harvested from the tails were treated with red blood cell lysis buffer (eBioscience) and subsequently analyzed by flow cytometry (BD Accuri C6, BD Biosciences) to determine the proportion of GFP- or DsRed-expressing cells.

Neurobehavioral tests. Wild-type mice, YG8R mice, YG8R mice transplanted with mfxn−/− hFXN+ HSPCs, and YG8R mice transplanted with either wild-type mouse GFP or DsRed/mtGFP-labeled HSPCs were tested at both 5 and 9 months of age before being sacrificed for tissue analysis. Rotarod analysis was performed using a Rota-Rod Series 8 apparatus (Ugo Basile). The rod was a knurled plastic dowel (diameter, 6.0 cm) set at a height of 30 cm. During training, the mice were placed on the stationary rotarod for 30 s before the trial was initiated. Then, each mouse was given

four trials per day, with a 60-s intertrial interval on the accelerating rotarod (4 to 40 rpm over 5 min). The latency to fall was recorded for each trial. Locomotor activity was measured using an automated monitoring system (Kinder Associates). Polycarbonate cages (42 × 22 × 20 cm) containing a thin layer of bedding material were placed into frames (25.5 × 47 cm) mounted with photocell beams. Each mouse was placed into the open field, and all movements were recorded over a 60-s testing period. Grip strength was measured using a device consisting of a 10-cm-long Tshaped bar connected to a digital dynamometer (Ugo Basile). Animals were held by the tail and placed before the bar, allowed to grip the bar with their forelimbs, and then gently pulled backward until the bar was released. Ten consecutive measurements were made for each animal, and both the average and maximal readouts were recorded. Gait measure (stride length) was collected using an automated gait analysis system (CatWalk, Noldus Instruments). Animals were placed at one end of the walkway and allowed to run down the length of the walkway, as two light sources illuminated the surface contact of paws with the glass floor, producing an image of a paw print. During locomotion, the glass walkway was filmed from below by a video camera. The CatWalk software program was used to analyze recorded footage, define individual paw prints (for example, left forepaw and right hindpaw), and give readouts of multiple parameters of gait. Testing was administered daily for 5 days. Only unbroken bouts of locomotion, during which animals ran down the walkway at a consistent speed, were used for analysis.

Primary fibroblast and macrophage isolation and transduction. Fibroblasts were generated from skin biopsies of neonate of YG8R mice. Cultures were maintained using high-glucose Dulbecco's modified Eagle's medium (Life Technologies) supplemented with 10% fetal bovine serum (FBS; Gibco, Life Technologies) and 1% penicillin/streptomycin (PenStrep; Gibco) at 37°C

under 5% CO2. Primary macrophages from DsRed mtGFP mice were derived from bone marrow cells. Bone marrow cells were flushed from the femurs of 6- to 8-week-old mice and kept in culture in RPMI 1640 with 10% FBS, 1% PenStrep, and 10% L929 conditioned medium (29) at 37°C under 5% CO2. For macrophage transduction with pCCL-FXN-eGFP, the IC-21 macrophage cell line was used (American Type Culture Collection catalog #TIB-186) and cultured in RPMI 1640 (Gibco). Six-well plates were coated with RetroNectin (20 ml/ml; Takara Bio) following the manufacturer's instructions. IC-21 macrophages were plated at a density of 250,000 cells in 2 ml per well and transduced with pCCL-FXN-eGFP using an MOI of 15. Medium was changed 24 hours after transduction.

Live imaging. YG8R fibroblasts were cocultured with DsRed Cox8-GFP or macrophages stably transduced with a lentivirus expressing hFXN-GFP, as previously described (17). Briefly, 75,000 fibroblasts were cocultured with an equal number of macrophagesin glass-bottomed culture dishes (MatTek Corp.). hFXN-GFP cocultures were stained with 50 nM MitoTracker (Invitrogen) for 45 min before imaging. Confocal live imaging was performed 1 and 2 days later using PerkinElmer UltraView Vox Spinning Disk Confocal with ×40 [numerical aperture (NA), 1.30] and ×60 (NA, 1.42) oil objective at 37°C under 5% CO2. Images were captured, processed, and analyzed using the Volocity software (PerkinElmer).

Mouse frataxin quantitative reverse transcription PCR. Total RNA was prepared from snap-frozen skeletal muscle, brain, and heart biopsies using the RNeasy Lipid and Fibrous Tissue kits (Qiagen) according to the manufacturer's instructions. cDNA was then prepared using iScript

cDNA Synthesis kit (Bio-Rad). Commercial TaqMan probes specific to mouse frataxin were used to quantitate expression (Applied Biosystems).

Measurement of oxidative stress. Protein lysates from tissues directly snap-frozen in liquid nitrogen after dissection were prepared using radioimmunoprecipitation assay buffer (Sigma-Aldrich) containing proteases inhibitors (Roche), as previously described (63). For each assay, 20 mg of protein was used after total protein concentration was determined using bicinchoninic acid (BCA) assay. Proteins were then derivatized by adding 1× 2,4- dinitrophenylhydrazine solution contained in the OxyBlot Protein Oxidation Detection kit (Chemicon International) according to the manufacturer's instructions. Samples were applied to electrophoresis and transferred to a polyvinylidene difluoride membrane. After blocking with 1% BSA/PBS–Tween 20, membrane was incubated with rabbit anti-dinitrophenyl antibody, followed by a goat anti-rabbit horseradish peroxidase conjugate, and visualized using the ECL kit (Pierce). Protein amounts were normalized using an anti-tubulin (ab6161, Abcam) antibody, and band intensity was quantified using the ImagePro software (Media Cybernetics).

Mouse mitochondria. RT2 Profiler PCR Array RNA was isolated from the cerebrum using the RNeasy Lipid Tissue Mini kit (Qiagen), and 0.5 mg of the sample was then reverse-transcribed with the iScript cDNA Synthesis kit (Bio-Rad). Samples were mixed with SYBR green, equally loaded into all wells of the Mouse Mitochondria RT2 Profiler PCR Array (catalog no. PAMM-087Z, Qiagen), and amplified as per the manufacturer's recommendation on the CFX96 thermocycler (Bio-Rad). Ct data were exported, and fold change was calculated using the DCt method between sample genes and a panel of housekeeping controls.

Lactate/pyruvate analysis. Muscle biopsies (10 mg) were homogenized in ice in 1 ml of ice-cold 40% acetonitrile (containing 0.1% formic acid/40% methanol/20% H2O) using a tissue grinder (Dounce), followed by centrifugation for 10 min at 13,000g. The extraction solution contained a stable isotope of lactate (13C3 sodium lactate, Cambridge Isotope Laboratories Inc.). Supernatants were removed, dried in a SpeedVac/lyophilizer system, and resuspended in 150 ml of 0.1% formic acid. Pellets were redissolved in 0.1 N NAOH, and protein content was measured using BCA assay. Five microliters of each resuspended supernatant was injected on a C18- PFP HPLC column (MAC-MOD Analytical), as previously described (64), and coupled to an API 4000 triple quadrupole mass spectrometer (AB Sciex). Molecular reaction monitoring for lactate (89 > 43), 13C3 lactate (92 > 45), and pyruvate (87 > 43 and 87 > 87) was used during the acquisition. Lactate and pyruvate peaks were both normalized to 13C3 lactate. Both lactate and pyruvate were further normalized to protein content (in milligrams) before calculation of thefinal lactate/pyruvate (L/P) peak area ratios used in Fig. 3B. Because the ratio is expressed in terms of normalized peak areas, the ratio values should not be confused with those determined from absolute concentration measurements, as performed in previous studies measuring L/P but still effective for examining relative differences between cohorts.

Vacuole imaging and quantification. DRGs from L5 were collected, sectioned at 30-mm intervals using a cryostat, and mounted on gelatin-coated slides. DRG sections were stained with thionin (Nissl stain) for visualization of neuronal cell bodies. Three DRGs per subject were acquired at a magnification of ×60 using a BZX700 fluorescence microscope (Keyence). The presence of vacuoles in each DRG was traced and measured by a blinded experimenter in duplicate

using ImageJ; vacuoles were defined as extremely circular white (Nissl-negative) areas with smooth edges within DRG neurons. The number of vacuoles and area of vacuolar space relative to entire area of each DRG section were compared across genotypes.

Heart histology and iron quantification. For histological preparations, terminally anesthetized mice were fixed by intracardial perfusion with 10% formalin. Fixed tissues were dissected, embedded in paraffin wax, and sectioned by standard methods. Sections were deparaffinized and stained using Perl's technique to detect ferric iron, as previously described (10). Whole-heart sections were imaged on an Keyence fluorescence microscope, and a single wide-field image was stitched together. Using the ImagePro Premier software (Media Cybernetics), quantification of iron staining was assessed by isolating the blue channel, measuring the area of signal, and then dividing from the total area of the section. Values were reported normalized to wild type.

Immunofluorescence and image acquisition. Heart and muscle tissues were fixed in 5% paraformaldehyde (PFA), equilibrated in 20% sucrose overnight, and frozen in Tissue-Tek optimal cutting temperature (OCT) medium at −80°C (Sakura Finetek USA); 10-mm sections were cut. The DRG, brain, and spinal cord tissue were fixed in PFA, cryopreserved in 30% sucrose, and frozen in OCT medium. For DRGs, tissue was cut into 20-mm sections and directly mounted to gelatin-coated slides. For the brain and spinal cord, tissue was sectioned to 30 mm and collected as free-floating sections. For immunofluorescence, tissues were incubated with the following antibodies: rat anti-CD68 (1:100; 137001, BioLegend), biotin rat anti-MHCII (1:100; 553622, BD Pharmigen), rabbit anti-GFP (1:500; ab290, Abcam), chicken anti-GFP (1:1500; ab13970, Abcam), rabbit anti-Iba1 (1:1500; #019-19741, Wako), goat anti-mCherry (1:1000; AB0040,

Sicgen), mouse anti-NeuN (1:500; MAB377, Millipore), rabbit anti-MBP (1:200; AB980, Millipore), mouse anti-NF200 (1:500; MAB5262, Millipore), mouse anti–a-actinin (1:400; Sigma-Aldrich), rabbit anti–von Willebrand factor (1:300; Chemicon), DAPI (1:500; Molecular Probes), and BODIPY-phalloidin (1:100; Molecular Probes). The appropriate Alexa Fluor–conjugated secondary antibodies (Invitrogen) were used for the visualization of antigens. Images were acquired using an LSM 880 confocal microscope with Airyscan (Zeiss), a Keyence BZ-X710 digital microscope system for high-resolution stitching images of tissue sections, or an Olympus FV1000 confocal microscope for live imaging. Confocal image stacks were analyzed with the Imaris software (Bitplane, Oxford Instruments).

Quantification of neuronal correction. The entire gray matter region of lumbar spinal cord sections from three YG8R mice transplanted with Cox8-GFP HSPCs and an nontransplanted control was stained with NeuN and imaged at 20× on an LSM 880 confocal microscope (Zeiss). NeuN+ neuronal cells were outlined and counted using the ImagePro Plus software (Media Cybernetics) and then assessed for GFP positivity, which was reported as a percentage of total NeuN cells (fig. S4). All acquisition, filtration, and processing steps were performed identically on the GFP channel between all samples.

Optical clearing of mouse spinal cord. A 6-mm segment of the cervical spinal cord from a mouse at 3 months after transplantation with DsRed+ HSPCs was processed for optical clearing, as previously described (65). Briefly, PFA-fixed tissue was infused with hydrogel monomer solution (4% PFA, 4% acrylamide, and 0.05% bis-acrylamide) and was thermally polymerized. Lipids were then passively extracted in SDS-containing borate buffer at 37°C for 4 weeks until the tissue was

cleared. Clarified tissue was incubated in RapiClear CS for 1 day and mounted using a WillCo dish. Tissues were then imaged using an Olympus FV1200 system equipped with a 10× water immersion objective (NA, 0.6; working distance, 3 mm; stack size, 1.65 mm; step size, 5 mm).

Statistics. We did not exclude any animals from our experiments. Experimenters were blinded to the genotype of the specific sample to every extent possible. We did not perform any power calculation analysis. All data displayed normal variance, except DRG vacuole measurements. For normal data and mitochondrial PCR array data, we performed one-way ANOVA, followed by post hoc Student's t test, to determine the statistical significance using GraphPad Prism 7.01 (GraphPad Software). Oxidative stress measurements used one-tailed t tests with the assumption that YG8R mouse tissue oxidation would be higher. For vacuole measurements, we used the Mann-Whitney nonparametric test corrected for multiple testing by the Bonferroni correction. In vitro experiments were performed in biological triplicates. Error bars denote SEM. Significance is indicated as follows: *P < 0.05, **P < 0.005, and ***P < 0.0005.

2.5: Acknowledgements

Chapter 2, in full, is a reprint of the material as it appears in Science Translational Medicine 2017. *Rocca, Celine J., Spencer M. Goodman, Jennifer N. Dulin, Joseph H. Haquang, Ilya Gertsman, Jordan Blondelle, Janell L. M. Smith, Charles J. Heyser, and Stephanie Cherqui. "Transplantation of Wild-type Mouse Hematopoietic Stem and Progenitor Cells Ameliorates Deficits in a Mouse Model of Friedreich's Ataxia." 9.413 (2017).* The dissertation author was a co-investigator and the second author of this paper.

2.6: References

1. V. Campuzano, L. Montermini, M. D. Moltò, L. Pianese, M. Cossée, F. Cavalcanti, E. Monros, F. Rodius, F. Duclos, A. Monticelli, F. Zara, J. Cañizares, H. Koutnikova, S. I. Bidichandani, C. Gellera, A. Brice, P. Trouillas, G. De Michele, A. Filla, R. De Frutos, F. Palau, P. I. Patel, S. Di Donato, J.-L. Mandel, S. Cocozza, M. Koenig, M. Pandolfo, Friedreich's ataxia: Autosomal recessive disease caused by an intronic GAA triplet repeat expansion. Science 271, 1423–1427 (1996).

2. H. Koutnikova, V. Campuzano, F. Foury, P. Dollé, O. Cazzalini, M. Koenig, Studies of human, mouse and yeast homologues indicate a mitochondrial function for frataxin. Nat. Genet. 16, 345–351 (1997).

3. S. Adinolfi, C. Iannuzzi, F. Prischi, C. Pastore, S. Iametti, S. R. Martin, F. Bonomi, A. Pastore, Bacterial frataxin CyaY is the gatekeeper of iron-sulfur cluster formation catalyzed by IscS. Nat. Struct. Mol. Biol. 16, 390–396 (2009).

4. J. D. Cook, K. Z. Bencze, A. D. Jankovic, A. K. Crater, C. N. Busch, P. B. Bradley, A. J. Stemmler, M. R. Spaller, T. L. Stemmler, Monomeric yeast frataxin is an iron-binding protein. Biochemistry 45, 7767–7777 (2006).

5. O. Gakh, S. Park, G. Liu, L. Macomber, J. A. Imlay, G. C. Ferreira, G. Isaya, Mitochondrial iron detoxification is a primary function of frataxin that limits oxidative damage and preserves cell longevity. Hum. Mol. Genet. 15, 467–479 (2006).

6. M. H. Parkinson, S. Boesch, W. Nachbauer, C. Mariotti, P. Giunti, Clinical features of Friedreich's ataxia: Classical and atypical phenotypes. J. Neurochem. 126 (suppl. 1), 103–117 (2013).

7. M. Pandolfo, Friedreich ataxia: The clinical picture. J. Neurol. 256 (suppl. 1), 3–8 (2009).

8. A. H. Koeppen, J. E. Mazurkiewicz, Friedreich ataxia: Neuropathology revised. J. Neuropathol. Exp. Neurol. 72, 78–90 (2013).

9. K. Solbach, O. Kraff, M. Minnerop, A. Beck, L. Schöls, E. R. Gizewski, M. E. Ladd, D. Timmann, Cerebellar pathology in Friedreich's ataxia: Atrophied dentate nuclei with normal iron content. Neuroimage Clin. 6, 93–99 (2014).

10. S. Al-Mahdawi, R. M. Pinto, D. Varshney, L. Lawrence, M. B. Lowrie, S. Hughes, Z. Webster, J. Blake, J. M. Cooper, R. King, M. A. Pook, GAA repeat expansion mutation mouse models of Friedreich ataxia exhibit oxidative stress leading to progressive neuronal and cardiac pathology. Genomics 88, 580–590 (2006).

11. S. Anjomani Virmouni, V. Ezzatizadeh, C. Sandi, M. Sandi, S. Al-Mahdawi, Y. Chutake, M. A. Pook, A novel GAA-repeat-expansion-based mouse model of Friedreich's ataxia. Dis. Model. Mech. 8, 225–235 (2015).

12. S. Anjomani Virmouni, C. Sandi, S. Al-Mahdawi, M. A. Pook, Cellular, molecular and functional characterisation of YAC transgenic mouse models of Friedreich ataxia. PLOS ONE 9, e107416 (2014).

13. H. P. Gaide Chevronnay, V. Janssens, P. Van Der Smissen, C. J. Rocca, X. H. Liao, S. Refetoff, C. E. Pierreux, S. Cherqui, P. J. Courtoy, Hematopoietic stem cells transplantation can normalize thyroid function in a cystinosis mouse model. Endocrinology 157, 1363–1371 (2016).

14. C. J. Rocca, A. Kreymerman, S. N. Ur, K. E. Frizzi, S. Naphade, A. Lau, T. Tran, N. A. Calcutt, J. L. Goldberg, S. Cherqui, Treatment of inherited eye defects by systemic hematopoietic stem cell transplantation. Invest. Ophthalmol. Vis. Sci. 56, 7214–7223 (2015).

15. K. Syres, F. Harrison, M. Tadlock, J. V. Jester, J. Simpson, S. Roy, D. R. Salomon, S. Cherqui, Successful treatment of the murine model of cystinosis using bone marrow cell transplantation. Blood 114, 2542–2552 (2009).

16. B. A. Yeagy, F. Harrison, M.-C. Gubler, J. A. Koziol, D. R. Salomon, S. Cherqui, Kidney preservation by bone marrow cell transplantation in hereditary nephropathy. Kidney Int. 79, 1198–1206 (2011).

17. S. Naphade, J. Sharma, H. P. Gaide Chevronnay, M. A. Shook, B. A. Yeagy, C. J. Rocca, S. N. Ur, A. J. Lau, P. J. Courtoy, S. Cherqui, Brief reports: Lysosomal cross-correction by hematopoietic stem cell-derived macrophages via tunneling nanotubes. Stem Cells 33, 301–309 (2015).

18. S. Domhan, L. Ma, A. Tai, Z. Anaya, A. Beheshti, M. Zeier, L. Hlatky, A. Abdollahi, Intercellular communication by exchange of cytoplasmic material via tunneling nano-tube like structures in primary human renal epithelial cells. PLOS ONE 6, e21283 (2011).

19. S. Sisakhtnezhad, L. Khosravi, Emerging physiological and pathological implications of tunneling nanotubes formation between cells. Eur. J. Cell Biol. 94, 429–443 (2015).

20. K. C. Vallabhaneni, H. Haller, I. Dumler, Vascular smooth muscle cells initiate proliferation of mesenchymal stem cells by mitochondrial transfer via tunneling nanotubes. Stem Cells Dev. 21, 3104–3113 (2012).

21. B.-H. T. Ton, Q. Chen, G. Gaina, C. Tucureanu, A. Georgescu, C. Strungaru, M.-L. Flonta, D. Sah, V. Ristoiu, Activation profile of dorsal root ganglia Iba-1 (+) macrophages varies with the type of lesion in rats. Acta Histochem. 115, 840–850 (2013).

22. A. Romero, E. Romero-Alejo, N. Vasconcelos, M. M. Puig, Glial cell activation in the spinal cord and dorsal root ganglia induced by surgery in mice. Eur. J. Pharmacol. 702, 126–134 (2013).

23. A. B. Schmitt, G. A. Brook, A. Buss, W. Nacimiento, J. Noth, G. W. Kreutzberg, Dynamics of microglial activation in the spinal cord after cerebral infarction are revealed by expression of MHC class II antigen. Neuropathol. Appl. Neurobiol. 24, 167–176 (1998).

24. J. Priller, A. Flügel, T. Wehner, M. Boentert, C. A. Haas, M. Prinz, F. Fernández-Klett, K. Prass, I. Bechmann, B. A. de Boer, M. Frotscher, G. W. Kreutzberg, D. A. Persons, U. Dirnagl, Targeting gene-modified hematopoietic cells to the central nervous system: Use of green fluorescent protein uncovers microglial engraftment. Nat. Med. 7, 1356–1361 (2001).

25. M. A. Eglitis, É. Mezey, Hematopoietic cells differentiate into both microglia and macroglia in the brains of adult mice. Proc. Natl. Acad. Sci. U.S.A. 94, 4080–4085 (1997).

26. J. B. Schulz, T. Dehmer, L. Schöls, H. Mende, C. Hardt, M. Vorgerd, K. Bürk, W. Matson, J. Dichgans, M. F. Beal, M. B. Bogdanov, Oxidative stress in patients with Friedreich ataxia. Neurology 55, 1719–1721 (2000).

27. J. Kim, J. P. Moody, C. K. Edgerly, O. L. Bordiuk, K. Cormier, K. Smith, M. F. Beal, R. J. Ferrante, Mitochondrial loss, dysfunction and altered dynamics in Huntington's disease. Hum. Mol. Genet. 19, 3919–3935 (2010).

28. B. H. Robinson, Lactic acidemia and mitochondrial disease. Mol. Genet. Metab. 89, 3–13 (2006).

29. M. Perdomini, B. Belbellaa, L. Monassier, L. Reutenauer, N. Messaddeq, N. Cartier, R. G. Crystal, P. Aubourg, H. Puccio, Prevention and reversal of severe mitochondrial cardiomyopathy by gene therapy in a mouse model of Friedreich's ataxia. Nat. Med. 20, 542–547 (2014).

30. F. Weidemann, S. Störk, D. Liu, K. Hu, S. Herrmann, G. Ertl, M. Niemann, Cardiomyopathy of Friedreich ataxia. J. Neurochem. 126 (suppl. 1), 88–93 (2013).

31. J. B. Lamarche, M. Côté, B. Lemieux, The cardiomyopathy of Friedreich's ataxia morphological observations in 3 cases. Can. J. Neurol. Sci. 7, 389–396 (1980).

32. H. Puccio, D. Simon, M. Cossée, P. Criqui-Filipe, F. Tiziano, J. Melki, C. Hindelang, R. Matyas, P. Rustin, M. Koenig, Mouse models for Friedreich ataxia exhibit cardiomyopathy, sensory nerve defect and Fe-S enzyme deficiency followed by intramitochondrial iron deposits. Nat. Genet. 27, 181–186 (2001).

33. S. C. Bodine, L. M. Baehr, Skeletal muscle atrophy and the E3 ubiquitin ligases MuRF1 and MAFbx/atrogin-1. Am. J. Physiol. Endocrinol. Metab. 307, E469–E484 (2014).

34. J. Rodriguez, B. Vernus, I. Chelh, I. Cassar-Malek, J. C. Gabillard, A. Hadj Sassi, I. Seiliez, B. Picard, A. Bonnieu, Myostatin and the skeletal muscle atrophy and hypertrophy signaling pathways. Cell. Mol. Life Sci. 71, 4361–4371 (2014).

35. H. Shitara, M. Shimanuki, J.-I. Hayashi, H. Yonekawa, Global imaging of mitochondrial morphology in tissues using transgenic mice expressing mitochondrially targeted enhanced green fluorescent protein. Exp. Anim. 59, 99–103 (2010).

36. H. Shitara, H. Kaneda, A. Sato, K. Iwasaki, J.-I. Hayashi, C. Taya, H. Yonekawa, Non-invasive visualization of sperm mitochondria behavior in transgenic mice with introduced green fluorescent protein (GFP). FEBS Lett. 500, 7–11 (2001).

37. F. Lim, G. M. Palomo, C. Mauritz, A. Giménez-Cassina, B. Illana, F. Wandosell, J. Díaz-Nido, Functional recovery in a Friedreich's ataxia mouse model by frataxin gene transfer using an HSV-1 amplicon vector. Mol. Ther. 15, 1072–1078 (2007).

38. P. M. Vyas, W. J. Tomamichel, P. M. Pride, C. M. Babbey, Q. Wang, J. Mercier, E. M. Martin, R. M. Payne, A TAT–frataxin fusion protein increases lifespan and cardiac function in a conditional Friedreich's ataxia mouse model. Hum. Mol. Genet. 21, 1230–1247 (2012).

39. J. Jones, A. Estirado, C. Redondo, J. Pacheco-Torres, M.-S. Sirerol-Piquer, J. M. Garcia-Verdugo, S. Martinez, Mesenchymal stem cells improve motor functions and decrease neurodegeneration in ataxic mice. Mol. Ther. 23, 130–138 (2015).

40. T. R. Brazelton, F. M. V. Rossi, G. I. Keshet, H. M. Blau, From marrow to brain: Expression of neuronal phenotypes in adult mice. Science 290, 1775–1779 (2000).

41. É. Mezey, K. J. Chandross, G. Harta, R. A. Maki, S. R. McKercher, Turning blood into brain: Cells bearing neuronal antigens generated in vivo from bone marrow. Science 290, 1779–1782 (2000).

42. R. C. Rennert, M. Sorkin, R. K. Garg, G. C. Gurtner, Stem cell recruitment after injury: Lessons for regenerative medicine. Regen. Med. 7, 833–850 (2012).

43. C. V. Borlongan, L. E. Glover, N. Tajiri, Y. Kaneko, T. B. Freeman, The great migration of bone marrow-derived stem cells toward the ischemic brain: Therapeutic implications for stroke and other neurological disorders. Prog. Neurobiol. 95, 213–228 (2011).

44. F. L. Wilkinson, A. Sergijenko, K. J. Langford-Smith, M. Malinowska, R. F. Wynn, B. W. Bigger, Busulfan conditioning enhances engraftment of hematopoietic donorderived cells in the brain compared with irradiation. Mol. Ther. 21, 868–876 (2013).

45. T. Yokota, K. Igarashi, T. Uchihara, K.-i. Jishage, H. Tomita, A. Inaba, Y. Li, M. Arita, H. Suzuki, H. Mizusawa, H. Arai, Delayed-onset ataxia in mice lacking a-tocopherol transfer protein: Model for neuronal degeneration caused by chronic oxidative stress. Proc. Natl. Acad. Sci. U.S.A. 98, 15185–15190 (2001).

46. Y. Shen, M. Z. McMackin, Y. Shan, A. Raetz, S. David, G. Cortopassi, Frataxin deficiency promotes excess microglial DNA damage and inflammation that is rescued by PJ34. PLOS ONE 11, e0151026 (2016).

47. R. I. Martínez-Zamudio, H. C. Ha, PARP1 enhances inflammatory cytokine expression by alteration of promoter chromatin structure in microglia. Brain Behav. 4, 552–565 (2014).

48. F. Palmieri, The mitochondrial transporter family (SLC25): Physiological and pathological implications. Pflugers Arch. 447, 689–709 (2004).

49. M. K. Eldomery, Z. C. Akdemir, F.-N. Vögtle, W.-L. Charng, P. Mulica, J. A. Rosenfeld, T. Gambin, S. Gu, L. C. Burrage, A. Al Shamsi, S. Penney, S. N. Jhangiani, H. H. Zimmerman, D. M. Muzny, X. Wang, J. Tang, R. Medikonda, P. V. Ramachandran, L.-J. Wong, E. Boerwinkle, R. A. Gibbs, C. M. Eng, S. R. Lalani, J. Hertecant, R. J. Rodenburg, O. A. Abdul-Rahman, Y. Yang, F. Xia, M. C. Wang, J. R. Lupski, C. Meisinger, V. R. Sutton, MIPEP recessive variants cause a syndrome of left ventricular non-compaction, hypotonia, and infantile death. Genome Med. 8, 106 (2016).

50. L. Zhang, H. Li, X. Hu, D. M. Benedek, C. S. Fullerton, R. D. Forsten, J. A. Naifeh, X. Li, H. Wu, K. N. Benevides, T. Le, S. Smerin, D. W. Russell, R. J. Ursano, Mitochondria-focused gene expression profile reveals common pathways and CPT1B dysregulation in both rodent stress model and human subjects with PTSD. Transl. Psychiatry 5, e580 (2015).

52. K. Liu, K. Ji, L. Guo, W. Wu, H. Lu, P. Shan, C. Yan, Mesenchymal stem cells rescue injured endothelial cells in an in vitro ischemia–reperfusion model via tunneling nanotube like structure-mediated mitochondrial transfer. Microvasc. Res. 92, 10–18 (2014).

53. K. Ridder, S. Keller, M. Dams, A.-K. Rupp, J. Schlaudraff, D. Del Turco, J. Starmann, J. Macas, D. Karpova, K. Devraj, C. Depboylu, B. Landfried, B. Arnold, K. H. Plate, G. Höglinger, H. Sültmann, P. Altevogt, S. Momma, Extracellular vesicle-mediated transfer of genetic information between the hematopoietic system and the brain in response to inflammation. PLOS Biol. 12, e1001874 (2014).

54. M. N. Islam, S. R. Das, M. T. Emin, M. Wei, L. Sun, K. Westphalen, D. J. Rowlands, S. K. Quadri, S. Bhattacharya, J. Bhattacharya, Mitochondrial transfer from bone-marrow–derived stromal cells to pulmonary alveoli protects against acute lung injury. Nat. Med. 18, 759–765 (2012).

55. K. Hayakawa, E. Esposito, X. Wang, Y. Terasaki, Y. Liu, C. Xing, X. Ji, E. H. Lo, Transfer of mitochondria from astrocytes to neurons after stroke. Nature 535, 551–555 (2016).

56. M.-È. Tremblay, R. L. Lowery, A. K. Majewska, Microglial interactions with synapses are modulated by visual experience. PLOS Biol. 8, e1000527 (2010).

57. H. Wake, A. J. Moorhouse, S. Jinno, S. Kohsaka, J. Nabekura, Resting microglia directly monitor the functional state of synapses in vivo and determine the fate of ischemic terminals. J. Neurosci. 29, 3974–3980 (2009).

58. S. Al-Mahdawi, R. M. Pinto, P. Ruddle, C. Carroll, Z. Webster, M. Pook, GAA repeat instability in Friedreich ataxia YAC transgenic mice. Genomics 84, 301–310 (2004).

59. T. Dull, R. Zufferey, M. Kelly, R. J. Mandel, M. Nguyen, D. Trono, L. Naldini, A third-generation lentivirus vector with a conditional packaging system. J. Virol. 72, 8463–8471 (1998).

60. D. Zychlinski, A. Schambach, U. Modlich, T. Maetzig, J. Meyer, E. Grassman, A. Mishra, C. Baum, Physiological promoters reduce the genotoxic risk of integrating gene vectors. Mol. Ther. 16, 718–725 (2008).

61. S. Pérez-Luz, A. Gimenez-Cassina, I. Fernández-Frías, R. Wade-Martins, J. Diaz-Nido, Delivery of the 135 kb human frataxin genomic DNA locus gives rise to different frataxin isoforms. Genomics 106, 76–82 (2015).

62. F. Harrison, B. A. Yeagy, C. J. Rocca, D. B. Kohn, D. R. Salomon, S. Cherqui, Hematopoietic stem cell gene therapy for the multisystemic lysosomal storage disorder cystinosis. Mol. Ther. 21, 433–444 (2013).

63. V. Campuzano, L. Montermini, Y. Lutz, L. Cova, C. Hindelang, S. Jiralerspong, Y. Trottier, S. J. Kish, B. Faucheux, P. Trouillas, F. J. Authier, A. Dürr, J.-L. Mandel, A. Vescovi, M. Pandolfo, M. Koenig, Frataxin is reduced in Friedreich ataxia patients and is associated with mitochondrial membranes. Hum. Mol. Genet. 6, 1771–1780 (1997).

64. I. Gertsman, J. A. Gangoiti, B. A. Barshop, Validation of a dual LC-HRMS platform for clinical metabolic diagnosis in serum, bridging quantitative analysis and untargeted metabolomics. Metabolomics 10, 312–323 (2014).

Chapter 3: Cellular and molecular mechanisms of TNT formation and intercellular trafficking

The following section 3.1, in full, is a reprint of material that appears in *Scientific Reports* on October 10, 2019.

3.1: TNTs and macrophage polarization

3.1.1: Introduction

Intercellular communication is essential to maintain and potentially restore homeostasis in multicellular organisms. Tunneling nanotubes (TNTs) are one interaction pathway consisting of long actin-rich membranous extensions capable of forming cytosolic connections between distant cells (1–3) . TNTs have been observed in vitro and in vivo facilitating transfer of molecular cargos ranging from electrical signals to organelles to pathogens (4–6) . Mechanistic investigations of hematopoietic stem and progenitor cell (HSPC) transplantation therapy for the lysosomal storage disorder cystinosis revealed HSPC-derived macrophages deliver functional lysosomal protein cystinosin through TNTs to diseased tissue, resulting in lifelong prevention of disease progression in the mouse model (7–9) .

Cystinosin is ubiquitously expressed within the lysosomal membrane to export cystine into the cytosol (10). However, loss-of-function mutations in the CTNS gene cause lysosomal cystine accumulation and crystallization leading to multi-organ failure (11,12). Current therapies merely ameliorate symptoms and delay disease progression (13). Our group has pioneered the use of HSPC transplantation as a promising new therapy for cystinosis with translation of this approach into an autologous gene-corrected HSPC transplantation clinical trial for human cystinosis patients underway (14–16).

Due to cystinosin being a non-secreted transmembrane protein, the ubiquitous prevention of pathogenic cell damage using HSPCs was unexpected until the mechanism of trafficking was shown to involve TNT-mediated delivery of healthy lysosomes from HSPC-derived macrophages to diseased tissue (7) . While many studies have demonstrated how pathogens like HIV (17) or malignancies like gliomas (18) can hijack TNTs, the structures also present an intriguing potential delivery system of therapeutic proteins to treat genetic diseases (19). Following HSPC transplantation, kidney macrophages formed TNTs that crossed the basement membrane and rescued proximal tubule cells by delivering cystinosin-bearing lysosomes (7) . The same mechanism has also been observed in the cornea and thyroid of transplanted cystinotic mice (8,9) , as well as in the X-linked tubulopathy Dent disease (20). In addition, studies of HSPC transplantation as treatment for the mitochondrial neurodegenerative disorder Friedreich's Ataxia reveal microglial correction of neurons, potentially through TNTs (21). Taken together, these data indicate a prolific ability of phagocytic cells to widely disseminate therapeutic molecules via TNT trafficking.

The plasticity of macrophages allows them to fulfill numerous biological functions ranging from proinflammatory roles in both arms of the immune system to immunomodulatory activities vis-à-vis tissue repair, homeostasis and resolution of inflammation. Traditionally, these distinct phenotypic behaviors have been classified as either proinflammatory mediators of a type I immune response (M1 or classical activation) versus. immunomodulatory tissue-remodelers (M2 or alternative) (22,23). However, this model risks oversimplification of a seamless phenotypic spectrum into a false dichotomy masking in vivo macrophage complexity, where these subtypes are dynamically changing in response to the cues received from the microenvironment, and thus never cleanly delineated (24,25).

In the current study, we investigated macrophage-mediated TNT formation and intercellular trafficking. Using novel image analysis platforms, we report that in vitro proinflammatory macrophage stimulation suppressed both TNT-like protrusion formation as well as intercellular organelle trafficking. In contrast, macrophages co-cultured with diseased Ctns−/− fibroblasts exhibited increased lysosomal and mitochondrial intercellular trafficking along with more frequent formation of larger protrusions. These data suggest that diseased cells stimulate TNT formation towards a thicker phenotype, which has been shown to more effectively transport organelles such as macrophages and intracellular vesicles (26). Unexpectedly, in vivo enrichment of proinflammatory macrophages showed similar disease rescue following Rac2−/− HSPC transplantation in Ctns−/− mice compared to wild-type (WT) mice. This discrepancy between mice and co-cultures highlights the well-known dangers of relying solely on in vitro polarization models where cytokine stimulation pushes macrophages to non-physiological polarization phenotypes. That said, increased macrophage-derived thicker TNT formation and trafficking activity seen in unstimulated cystinotic co-cultures effectively models in vivo observations of enhanced macrophage recruitment and intercellular lysosomal delivery after HSPC transplantation (7). Using both cells and transplanted mice, we can therefore probe aspects of TNTs induced when stress on a separate cellular population is stimulating macrophage TNT formation in a paracrine fashion. Ultimately, a detailed understanding of these processes could ultimately better explain and enhance the effective delivery of non-secreted genetic products.

3.1.2: Results

Macrophage membrane protrusions are suppressed by proinflammatory stimulation but enhanced by co-culture with diseased cells. Previous work has uncovered that proinflammatory bone marrow derived macrophages (BMDMs) display a more rounded ameboid morphology compared to unstimulated or anti-inflammatory cells (27). To investigate tunneling nanotube (TNT) formation in this context, we treated primary murine BMDMs and the immortalized IC-21 peritoneal macrophage cell line with either LPS/IFNγ, directing differentiation towards proinflammatory M1-like cells, M(LPS/IFNγ), or with IL-4/IL-10 for differentiation towards immunomodulatory M2-like macrophages, M(IL-4/IL-10). Using a variety of assays to characterize expression of well-established macrophage polarization markers, we rigorously validated our in vitro polarization experimental system. First, we analyzed differentially expressed mRNAs and proteins, observing increased expression of numerous proinflammatory markers such as inducible nitric oxide synthase (iNos), interleukin-6 (Il-6) and interleukin-1β (Il-1β) following LPS/IFNγ treatment, as well as upregulation of anti-inflammatory markers such as Cd206, Ym1 and Fizz1 after IL-4/IL-10 stimulation (Fig. 3.1a,b, Supplemental File 2, Fig. S1) (28,29). Furthermore, M(IL-4/IL-10) displayed greater enzymatic activity of arginase-1 (ARG1), an important biosynthetic regulator of tissue repair, while M(LPS/IFNγ) increased extracellular secretion of monocyte chemoattractant protein 1 (MCP1) (Fig. 3.1c,d), a potent proinflammatory chemokine that regulates migration and infiltration of macrophages (30). Finally, polarized BMDMs were analyzed by flow cytometry where we observed expected changes in expression of proinflammatory markers CD80 and CD126 or anti-inflammatory CD206 (Fig. 3.1e) (31). To assess macrophage viability following polarization, we also measured cell proliferation using WST-1, which decreased following LPS/IFNγ but not IL-4/IL-10 stimulation in both BMDMs

($P = 0.0015$) and IC-21 macrophages ($P < 0.0001$) compared to non-treated controls (Fig. 3.1f). In contrast, apoptosis measured by Annexin V and Propidium Iodide-stained cells did not vary between treatment groups (data not shown). Taken together, in vitro treatment yields the anticipated changes in marker expression at both the mRNA and protein levels, confirming that our system replicates the expected polarization findings.

Figure 3.1: LPS/IFNγ polarization suppresses protrusion formation in BMDMs and IC-21 macrophages. (a) Bar graph representing mRNA expression of M(LPS/IFNγ) and M(IL4/IL10) markers relative to housekeeping control Gapdh in BMDMs and IC-21 macrophages after 48-hour pro- and anti-inflammatory macrophage polarization compared to non-treated cells (n = 5). (b) Representative immunoblots depicting polarization-associated signature protein expression in pro- and anti-inflammatory IC-21 macrophages and untreated controls. MCP1 and iNOS are M(LPS/IFNγ) markers, while ARG1 and CD206 are M(IL-4/IL-10) markers. CD68 is a pan-macrophage marker, and tubulin serves as the loading control (n = 2–4). (c) Graph depicts normalized colorimetric measurements of the M(IL-4/IL-10) marker ARG1 enzymatic activity from cell lysate following independent polarization treatments (n = 3). (d) Bar graph depicting normalized MCP1 cytokine secretion into media following polarization as measured by ELISA (n = 3). (e) Bar graphs representing flow cytometry analysis showing frequency of expression of M(LPS/IFNγ) markers CD80 and CD126 or M(IL-4/IL-10) marker CD206 following BMDM polarization (n = 3). (f) Bar graphs presenting normalized colorimetric absorbance values measuring cell proliferation using WST-1 cell proliferation reagent in BMDMs and IC-21 macrophages acquired three days post polarization treatment (n = 3). (g) Representative wide-field fluorescent images of control vs. M(LPS/IFNγ)- or M(IL4/IL10)-polarized BMDMs and IC-21 macrophages. Larger micrographs are stitched images of 5 × 5 individual tile. Zoomed inserts demonstrate automated image processing selecting for protrusion-positive (green) or negative (red) cells. See Supplemental File 2, Fig. S1 for method description and examples. (h) Percentile quantification of protrusion-positive cells in polarized BMDMs and IC-21 macrophages. Each data point in the box-and-whisker histogram is one stitched region with five regions analyzed per experiment (n = 3). (i) Representative fluorescent images of eGFP+ IC-21 co-cultures grown for three days with either WT (left) or Ctns−/− (right) DsRed+ fibroblasts. Boxed insert shows automated protrusion detection analysis with percentage of eGFP+ protrusion-positive cells shown in histogram (n = 3). (j) Representative fluorescent images of polarized eGFP+ IC-21 macrophage and Ctns−/− DsRed+ fibroblast co-cultures. Histogram illustrates percentage of control or M(LPS/IFNγ) and M(IL4/IL10) macrophages with protrusions (n = 3). All scale bars: 500 μM. All bar graphs shown as mean ± standard deviation (SD). P values were determined by either one-way ANOVA or student's t-tests. *P < 0.05, **P < 0.01, ***P < 0.001, ****P < 0.0001.

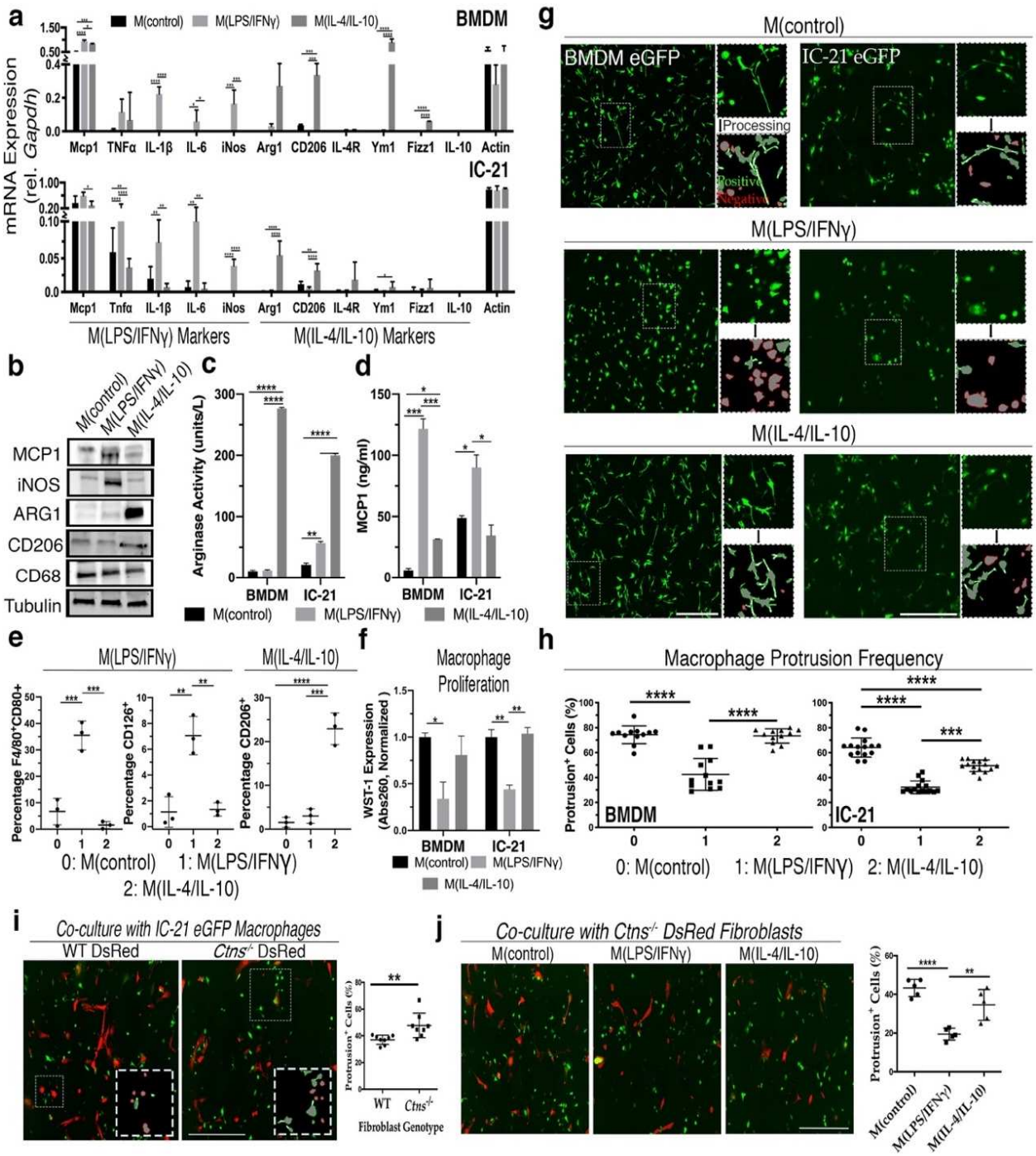
a
BMDM
M(control)
M(LPS/IFNγ)
M(IL-4/IL-10)
mRNA Expression (rel. Gapdh)
Mcp1 TNFα IL-1β IL-6 iNos Arg1 CD206 IL-4R Ym1 Fizz1 IL-10 Actin
IC-21
Mcp1 Tnfα IL-1β IL-6 iNos Arg1 CD206 IL-4R Ym1 Fizz1 IL-10 Actin
M(LPS/IFNγ) Markers
M(IL-4/IL-10) Markers
b
M(control)
M(LPS/IFNγ)
M(IL-4/IL-10)
MCP1
iNOS
ARG1
CD206
CD68
Tubulin
c
Arginase Activity (units/L)
BMDM IC-21
M(control) M(LPS/IFNγ) M(IL-4/IL-10)
d
MCP1 (ng/ml)
BMDM IC-21
g
M(control)
BMDM eGFP
IC-21 eGFP
Processing
Positive
Negative
M(LPS/IFNγ)
M(IL-4/IL-10)
e
M(LPS/IFNγ)
M(IL-4/IL-10)
Percentage F4/80+CD80+
Percentage CD126+
Percentage CD206+
0: M(control) 1: M(LPS/IFNγ)
2: M(IL-4/IL-10)
f
Macrophage Proliferation
WST-1 Expression (Abs260, Normalized)
BMDM IC-21
M(control) M(LPS/IFNγ)
M(IL-4/IL-10)
h
Macrophage Protrusion Frequency
Protrusion+ Cells (%)
BMDM
IC-21
0: M(control) 1: M(LPS/IFNγ) 2: M(IL-4/IL-10)
i
Co-culture with IC-21 eGFP Macrophages
WT DsRed
Ctns-/- DsRed
Protrusion+ Cells (%)
WT Ctns-/-
Fibroblast Genotype
j
Co-culture with Ctns-/- DsRed Fibroblasts
M(control)
M(LPS/IFNγ)
M(IL-4/IL-10)
Protrusion+ Cells (%)
M(control)
M(LPS/IFNγ)
M(IL-4/IL-10)

Upon imaging of treated cells, we also observed the expected shift of M(LPS/IFNγ) morphology to a more rounded phenotype in both BMDMs and IC-21 (Fig. 3.1g). We developed an image analysis workflow using ImagePro Premier to automatically detect and quantify fluorescent membrane protrusions using customizable morphological filtration based on characteristics such as length, width and circularity (Supplemental File 2, Fig. S2). By analyzing larger stitched images acquired using the wide-field Keyence fluorescence microscope, our high-throughput method enables automated, rapid and unbiased analysis of fluorescent cellular protrusions from dozens to hundreds of cells at once. Using this algorithm, we observed a significant reduction of approximately 50% in the protrusion frequency of BMDMs and IC-21 macrophages following LPS/IFNγ stimulation compared to non-treated macrophages ($P < 0.001$) (Fig. 3.1h). In contrast, M(IL-4/IL-10) BMDM protrusion frequency was statistically indistinguishable from control, while IC-21 displayed a modest decrease.

We sought to extend on our protrusion frequency findings by stimulating BMDMs with each cytokine or stimulant individually. We observe that either LPS or IFNγ by themselves are equally effective as when combined to reduce protrusion formation compared to untreated or M(IL-4/IL-10) (Supplemental File 2, Fig. S3). Furthermore, just as M(IL-4/IL-10) BMDMs, we again detected no difference in protrusion frequency for either M(IL-4) or M(IL-10) BMDM relative to untreated controls. Recent evidence suggests that tuberculosis infection triggers an increase in M(IL-10) macrophage TNT formation, but direct stimulation of BMDMs with IL-10 does not seem to recapitulate this phenotype (32).

We previously reported that co-culture of IC-21 macrophages with murine cystinotic fibroblasts appeared to increase the formation of TNTs (7). We replicated these experiments using our new automated imaging system and observed an increase in membrane protrusion formation

in IC-21 macrophages co-cultured with diseased murine Ctns−/− fibroblasts compared to wildtype fibroblasts ($P = 0.007$) (Fig. 3.1i). Proinflammatory stimulation of these co-cultures yielded a reduction in macrophage-derived protrusion formation with no obvious morphological changes in fibroblasts (Fig. 3.1j), confirming our previous data (Fig. 3.1h). Taken together, these data indicate proinflammatory M(LPS/IFNγ) macrophages generate fewer membrane protrusions than the immunomodulatory M(IL-4/IL-10) cells, and that diseased cystinotic cells enhanced protrusion formation in macrophages upon co-culture.

Macrophage-derived membrane protrusions resemble tunneling nanotubes. As no TNT-specific markers have been identified, we investigated the identity of macrophage-derived membrane protrusions based primarily on their morphology; TNTs are long, highly dynamic actin-rich tubes extending out from the plasma membrane without contacting the underlying substratum (33,34). Cytoskeletal immunostaining of macrophage co-cultures revealed that all protrusions were actin-rich, while some also contained a tubulin core (Fig. 3.2a), a unique feature of thicker TNTs generated by macrophages mediating organelle transfer (26). Protrusions were visualized in three dimensions via high-resolution imaging of Z-stacks and generation of 3D-reconstructions using ImagePro (Fig. 3.2b, Supplemental Videos 3.1 and 3.2). Both BMDMs and IC21 macrophages were found to have eGFP-positive protrusions extending above the substratum. Termini of the eGFP protrusions were observed directly adjacent to DsRed fibroblast cell bodies potentially indicating membrane fusion and facilitation of TNT stabilization through intercellular membrane connections. In addition, we treated BMDMs co-cultured with Ctns−/− fibroblasts with cytochalasin B (cytoB), an actin destabilizing agent reported to prevent TNT formation and to inhibit organelle trafficking (35,36). Treatment with cytoB for 24 hours eliminated membrane

protrusions from BMDMs with the extensions being restored several days following removal of cytoB (Fig. 3.2c).

In order to further characterize protrusions, we analyzed the shape and size of the automatically detected regions. We seeded and imaged equal numbers of eGFP BMDMs either alone or in co-culture with DsRed Ctns−/− fibroblasts. We first used our image analysis workflow to determine that co-cultures had a higher percentage of cells with protrusions than BMDMs alone ($P = 0.046$) (Fig. 3.2d). Using the automatically detected regions as guides, we blindly separated complete protrusions from the cell body, then used ImagePro to measure the resultant regions. From both conditions combined, we measured 242 individual protrusions and found that the mean protrusion area was 380.5 ± 145.4 μm2 and mean length was 45.00 ± 15.41 μm. As TNTs are extremely diverse, there is considerable variation on what "standard" dimensions between cell types (37). That said, most authors report an average TNT length between 17.7 μm (Jurkat T cells) and 44 μm (ARPE-19 retinal pigment epithelial cells), while the longest protrusions can reach up to 120 μm, confirming our measurements are compatible with TNTs (34,38). Unexpectedly, we also determined that protrusions generated from co-cultured macrophages were larger, longer and more elongated, meaning that they were less circular and had a larger ratio of the major to minor axis (Fig. 3.2e). These data not only confirm that a sizable fraction of protrusions appear to be of appropriate size to be considered TNTs but also highlights how the presence of diseased cystinotic cells affects protrusion morphology, as well as frequency. This is particularly interesting considering that previous work has shown that thicker macrophage TNTs preferentially transport organelles (26).

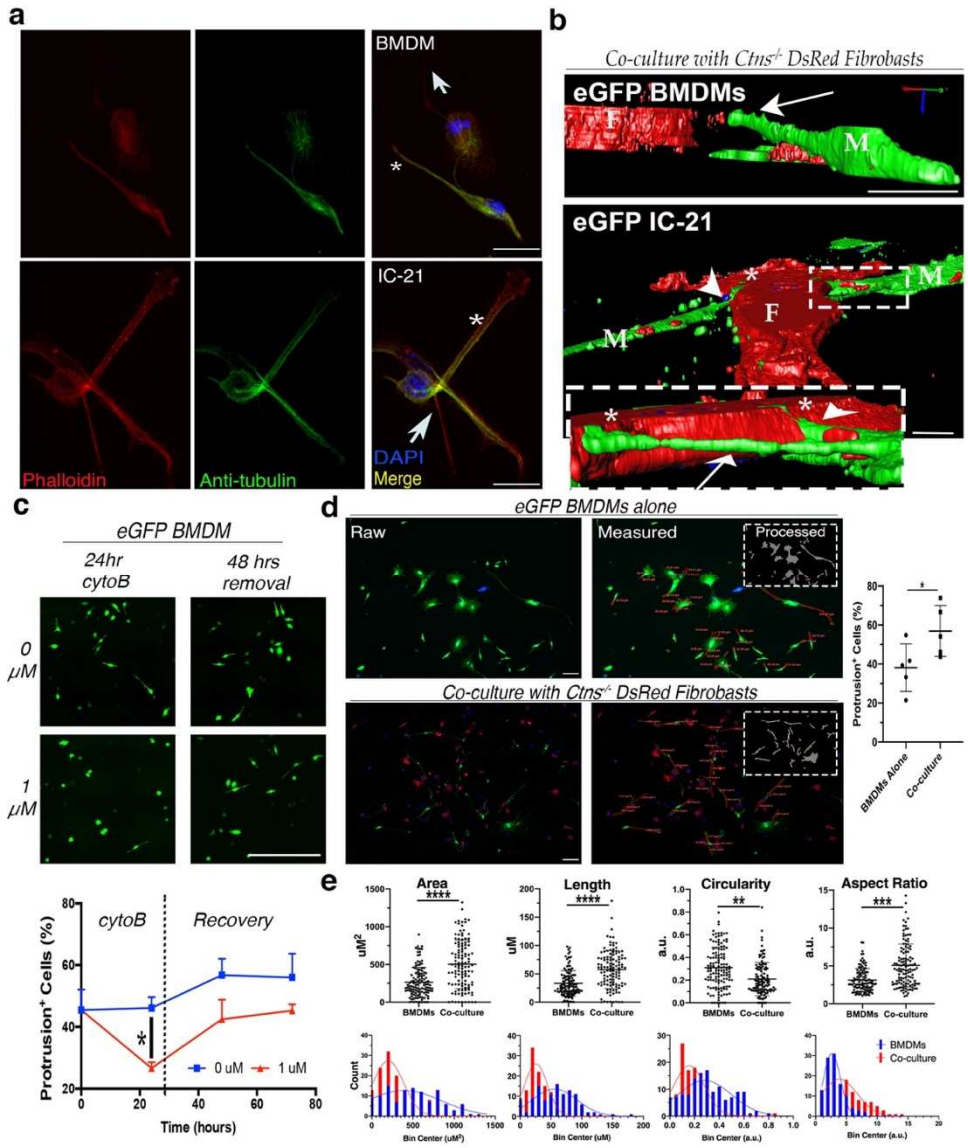

Figure 3.2: Some macrophage protrusions resemble TNT structure, behavior, and morphology. (a) Confocal micrographs of BMDMs and IC-21 cells after immunostaining for cytoskeletal components - actin (red) and tubulin (green). Thinner (arrows) and thicker (stars) protrusions indicated in both cell types. Scale bars: 10 µM. (b) 3D Z-stack reconstructions of eGFP+ BMDM or IC-21 cells (labeled M) co-cultured with Ctns−/− DsRed+ fibroblasts (labeled F). Boxed insert highlights protrusions extending above dish surface (arrows) and resting along the substratum (arrowhead). Scale bars: 10 µM. (c) Representative stitched micrographs depicting eGFP+ BMDMs following treatment and removal of cytochalsin B (cytoB) compared to untreated controls. XY graph shows percentage of protrusion-positive cells in each condition over time (n = 3 regions per treatment). Scale bar: 500 µM. (d) Representative raw confocal micrographs and measured images for eGFP BMDMs alone and in co-culture with Ctns−/− DsRed+ fibroblasts. Raw images were first processed for automated protrusion detection (insert) and the box-and-whisker plot (right) displays percentile quantification of protrusion-positive cells for BMDMs alone and in co-culture. Protrusion detection software rarely captures complete shape, so results were used as a guide in order to blindly manually separate protrusions from cell bodies by cutting along the estimation of normal membrane curvature. ImagePro was then used to measure protrusions; area measurements shown on top image and length on bottom. Scale bar: 100 µM. (e) Box-and-whisker plot (top) and frequency histogram (bottom) depicting area, length, circularity and aspect ratio protrusion measurements for BMDMs alone vs. in co-culture. Circularity is calculated as the ratio of the object compared to a circle with diameter equal to object's maximum Feret diameter, and represented on a scale from 0–1.0, with 1.0 being a perfect circle. Aspect ratio is the ratio of the major and minor axis of an eclipse equivalent to the object, with a higher value meaning a more elongated object. P values determined by one-way ANOVA or student's t-tests. *P < 0.05, **P < 0.01, ***P < 0.001, ****P < 0.0001

Finally, we analyzed expression of several genes involved in TNT formation following macrophage polarization to assess any differential expression of TNT-associated genes (Supplemental File 2, Fig. S4). In M(LPS/IFNγ) BMDMs, we observe increased mRNA expression of the MHC class II protein leukocyte specific transcript 1 (Lst1). In contrast, M(LPS/IFNγ) BMDMs displayed decreased expression of the Rho-family GTPase cell division control protein 42 homolog (Cdc42). We did not detect any changes in other TNT-linked genes such as M-Sec, a component of the exocyst complex that directly promotes TNT formation nor did we detect any changes in protein expression (data not shown) (39). Such changes in TNT marker expression after polarization are intriguing but thorough study of protein activity and localization would be required to uncover any mechanistic links between polarization and TNT formation. As such, in terms of protrusion characterization, a focus on structure, behavior and morphology is the more reliable method to indicate that a good fraction of the macrophage-derived protrusions automatically observed in our co-culture conditions represent bona fide TNTs.

Co-culture of macrophages with cystinotic cells increased not only lysosomal but mitochondrial intercellular transfer as well. To investigate the potential impact of macrophage polarization on TNT-mediated intercellular organelle trafficking, Ctns−/− and WT DsRed+ fibroblasts were co-cultured with IC-21 macrophages stably transduced with the fusion proteins cystinosin-eGFP or frataxin-eGFP, a mitochondrial iron chelator defective in Friedreich's ataxia40. In vitro live imaging previously revealed transfer of cystinosin-eGFP-bearing lysosomes or frataxin-eGFP-bearing mitochondria from macrophages to diseased murine Ctns−/− or Fxn−/− fibroblasts, respectively (7,8). High-magnification 3D-reconstructions confirmed the presence of eGFP-positive organelles within the cytoplasm of DsRed+ fibroblasts, as demonstrated by 3D renderings and orthogonal projections (Supplemental File 2, Fig. S5a,b, Supplemental Videos 3.3

and 3.4). Lysosomal transfer was confirmed to occur through TNT-like structures (Supplemental File 2, Fig. S5c, Supplemental Video 3.5).

We quantified the efficiency of lysosomal and mitochondrial transfer from the macrophages to the fibroblasts using another image analysis algorithm similar to the one we developed for TNT quantification, which measures the frequency of eGFP puncta ("donor") within a region of interest (ROI) defined by DsRed+ "recipient" cell (Supplemental File 2, Fig. S6). Co-cultures of 75,000 cystinosin-eGFP or frataxin-eGFP-expressing IC-21 macrophages and 50,000 DsRed+ WT or Ctns−/− fibroblasts were grown for three days and then fixed; fibroblasts cultured alone were used as controls (Fig. 3.3a). Fluorescent imaging revealed significantly higher numbers of both cystinosin-eGFP lysosomes ($P = 0.042$) and frataxin-eGFP mitochondria ($P = 0.019$) in Ctns−/− fibroblasts compared to WT fibroblasts (Fig. 3.3b,c, Supplemental File 2, Fig. S6c). Further, we treated macrophages for co-culture experiments to determine if either macrophage subtype impacts the efficacy of intercellular trafficking. We observed a significantly decreased presence of cystinosin-eGFP-positive lysosomes within fibroblasts co-cultured with M(LPS/IFNγ) macrophages ($P = 0.045$) (Fig. 3.3d).

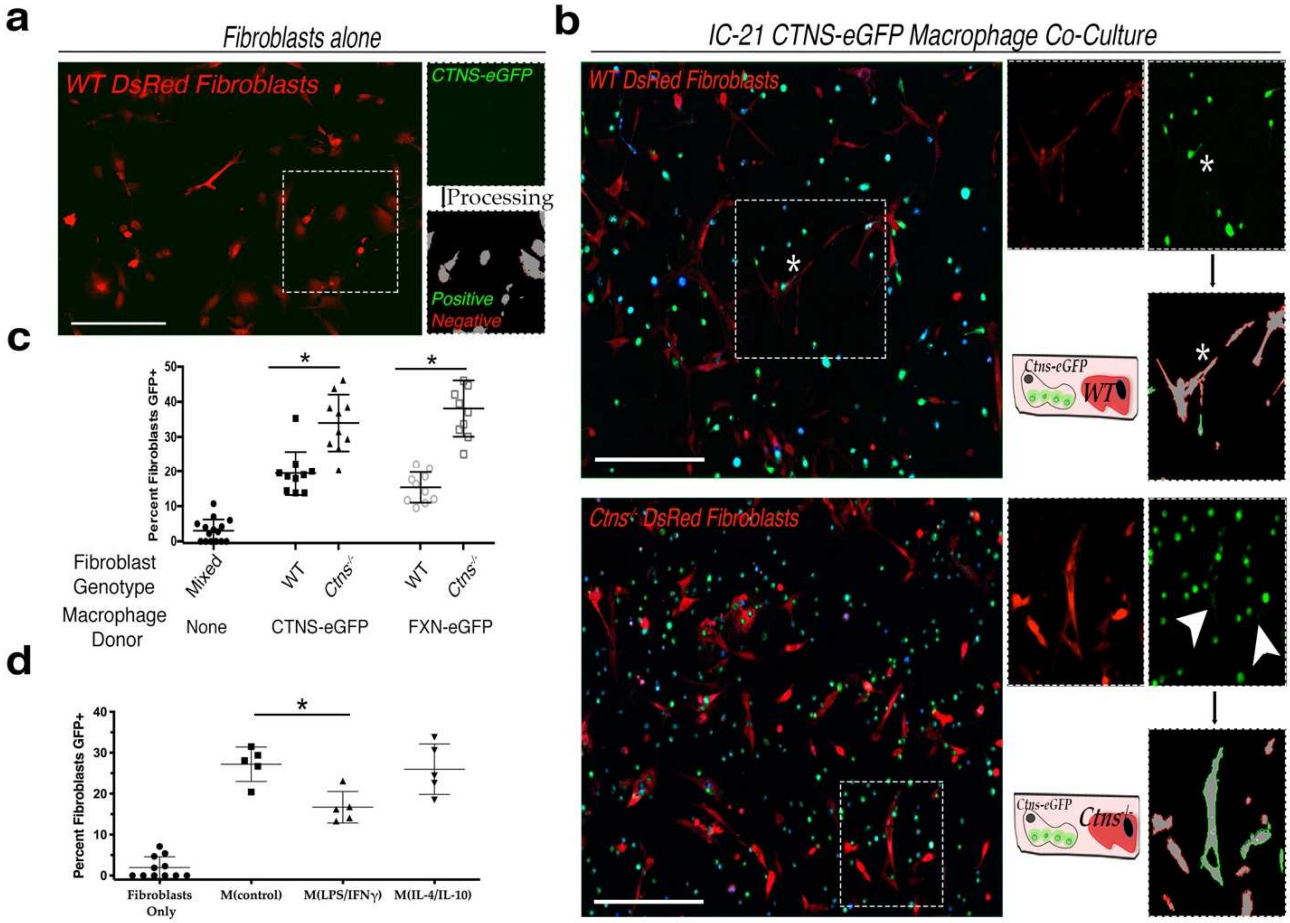

Figure 3.3: Intercellular trafficking of cystinosin-eGFP lysosomes and frataxin-eGFP mitochondria is increased to diseased Ctns−/− fibroblasts and diminished following proinflammatory polarization of co-cultured macrophages. (a) Representative stitched fluorescent micrograph of essential co-culture background control with only recipient DsRed+ fibroblasts. Boxed insert depicts automated image processing showing donor-positive (green) and donor-negative cells (red). See Supplemental File 2, Fig. S3 for automation methodology. (b) Representative fluorescent images of IC-21 cystinosin-eGFP co-cultures with either WT or Ctns−/− DsRed+ fibroblasts. Zoomed inserts highlight automated transfer quantification. Arrowheads indicate eGFP signal within DsRed+ fibroblasts. Stars indicate excluded signal due to cellular overlap. (c) Percentile quantitation of cystinosin- or frataxin-eGFP+ fibroblasts via automated image analysis. Each data point represents percent of donor-positive recipient cells in one stitched image (n = 3). All co-culture conditions have significantly more donor eGFP signal than background control with only fibroblasts ($P < 0.05$). (d) Frequency of cystinosin-eGFP trafficking in macrophage and fibroblast co-cultures following polarization with comparison to fibroblasts alone control. Histogram showing percentage of fibroblasts automatically determined positive for eGFP signal (n = 5). All scale bars are 500 µM. All graphs shown as mean ± SD. P values determined by one-way ANOVA or student's t-tests. *$P < 0.05$, **$P < 0.01$

To corroborate our findings using another robust assay, we performed flow cytometry on co-cultures to analyze dual eGFP- and DsRed-positive cells; both cell types cultured alone were used as gating controls (Fig. 3.4a and Supplemental File 2, Fig. S7a). Consistent with our fluorescent imaging results, a significant increase of approximately 70–90% of the dual-positive

population was observed in co-cultures of Ctns−/− fibroblasts with both cystinosin-eGFP ($P = 0.0168$) or frataxin-eGFP ($P = 0.0371$) macrophages as compared to WT fibroblast co-cultures (Fig. 3.4b). Another control of eGFP+ and DsRed+ cells mixed immediately prior to sorting did not yield dual-positive cells, indicating that prolonged co-culture is necessary to facilitate cellular interaction resulting in the generation of an eGFP+DsRed+ population (Supplemental File 2, Fig. S7b). Furthermore, proinflammatory macrophage polarization also dramatically decreased the transfer of cystinosin-eGFP and frataxin-eGFP (Fig. 3.4c). Altogether, these data show that diseased cells enhance transfer of lysosomes and mitochondria from macrophages to the fibroblasts, while proinflammatory polarization inhibits this process.

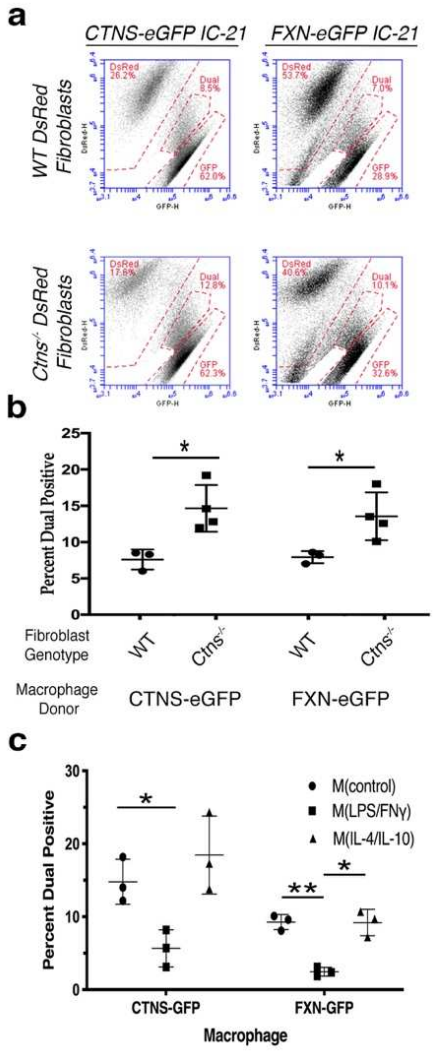

Figure 3.4: Flow cytometry confirms that intercellular trafficking is increased to diseased Ctns−/− fibroblasts and suppressed by proinflammatory polarization. (a) Representative FACS plots of DsRed (y-axis) and eGFP (x-axis) for 50,000 cells following co-culture of either cystinosin- or frataxin-eGFP and WT or Ctns−/− DsRed+ fibroblasts. Signal between eGFP and DsRed gates classified as a "dual-positive" eGFP+DsRed+ population. See Supplemental File 2, Fig. S4 for sorting and gating strategy. (b) Percentage quantification of eGFP+DsRed+ dual-positive cells in cystinosin- or frataxin-eGFP macrophage co-cultures with WT or Ctns−/− DsRed+ fibroblasts. Replicates consisted of co-cultures with fibroblasts derived from multiple mice (n = 4). (c) Quantification of dual-positive cell frequency after polarization treatment of co-cultures with cystinosin- or frataxin-eGFP and Ctns−/− DsRed+ fibroblasts (n = 3). All graphs shown as mean ± SD. P values determined by one-way ANOVA or student's t-tests. *P < 0.05, **P < 0.01.

HSPC-derived macrophages within the kidney of transplanted Ctns−/− mice appear to preferentially express M(LPS/IFNγ) markers. As in vitro polarization indicates that proinflammatory M(LPS/IFNγ) macrophages have impaired TNT formation and organelle transfer, we assessed the in vivo macrophage phenotype following HSPC transplantation in

Ctns−/− mice. We transplanted WT eGFP HSPCs into Ctns−/− recipient mice via tail vein injection as previously described (14) and analyzed macrophage polarization markers by performing immunostaining on kidney sections (Supplemental File 2, Fig. S8). We observed robust colocalization between the eGFP+ HSPC progeny and the pan-macrophage marker CD68 (Supplemental File 2, Fig S8a). Unexpectedly, more abundant co-localization was detected between the stem cell progeny and markers for M(LPS/IFNγ) such as CD16/32 or MHCII, than with anti-inflammatory markers ARG1, CD206 or CD163 (Supplemental File 2, Fig. S8b). Antibodies were tested on other tissues such as tumors to ascertain positive immunoreactivity (Supplemental File 2, Fig. S8c). These data suggest that in vivo proinflammatory macrophages are responsible for tissue preservation after WT HSPC transplantation in cystinosis.

Disruption of anti-inflammatory macrophage polarization with Rac2−/− HSPCs has no effect on HSPC transplantation efficacy or TNT formation. To determine if proinflammatory macrophages are responsible for tissue preservation in cystinosis following HSPC transplantation, we genetically perturbed macrophage polarization to assess if deficiencies prevented rescue of the cystinosis phenotype following HSPC transplantation. The Rac2−/− mouse model, disrupting the hematopoietic-specific Rho family GTPase Rac2, was chosen due to its functions in actin cytoskeletal reorganization and macrophage polarization (41,42). Since RAC2 was shown to drive M(IL-4/IL-10) macrophage differentiation, the proinflammatory M(LPS/IFNγ) macrophage population was enriched in knockout Rac2−/− mice (43–45). A very similar family member, RAC1, also has a role in the biogenesis of macrophage protrusions including invadopodia, lamellipodia and TNTs (42,46).

To test if Rac2 elimination has any effect on HSPC transplantation efficacy, HSPCs isolated from Rac2−/− eGFP-transgenic mice were transplanted into 2-month-old Ctns−/−

recipient mice. Ctns−/− mice transplanted with WT eGFP+ or Ctns−/− eGFP+ HSPCs proven effective or ineffective at prevention of cystinosis, respectively, were used as controls (14). HSPCs engraftment was measured by quantifying eGFP+ peripheral blood cells, which did not significantly differ between the three transplanted groups (average for WT −71.5%, Ctns−/− −75.6% and Rac2−/− −65.9%). Mice were sacrificed six months post-transplantation, and samples were collected for biochemical and phenotypic characterization. Assessment of tissue cystine content in WT HSPC recipients resulted in a dramatic reduction in cystine load in the liver, spleen, and kidneys relative to Ctns−/− HSPC-transplanted animals, as expected (Fig. 3.5a). Surprisingly, transplanted Rac2−/− HSPCs resulted in a decrease of cystine content to the same magnitude as WT HSPC controls. In addition, rescue of Ctns expression in tissues was similar in WT and Rac2−/− HSPC-transplanted Ctns−/− mice (Fig. 3.5b). Taken together, these data indicate that Rac2−/− HSPC transplantation is fully capable of restoring functional cystinosin to diseased tissue.

We then analyzed kidney sections by immunofluorescence for immune cell infiltration and observed co-localization between Rac2−/− eGFP HSPC progeny and macrophage markers such as F4/80 or CD68 (Fig. 3.5c), indicating that typical macrophage differentiation remained unaltered. We also detected eGFP TNT-like protrusions within kidneys of both Rac2−/− and WT HSPC recipients that stained positive for actin, another hallmark of TNTs (Fig. 3.5d). These data confirm that knockout HSPC-derived cells retain the ability to form TNT-like protrusions in vivo.

Finally, we investigated the protrusive behavior and polarization phenotype of BMDMs isolated from Rac2−/− eGFP mice in vitro. We quantified co-cultures of freshly isolated WT eGFP+ and Rac2−/− eGFP+ BMDMs with Ctns−/− fibroblasts using our protrusion detection imaging algorithm (Supplemental File 2, Fig. S1) and observed no significant differences in protrusion frequency between WT- and Rac2−/−- BMDMs ($P = 0.0472$; Fig. 3.5e). We then

analyzed polarization markers and confirmed that in contrast with WT BMDMs, Rac2−/− BMDMs skew towards M(LPS/IFNγ) without any extrinsic stimulation (Fig. 3.5f–h). However, we note that the magnitude of change in mRNA expression of genes was overall either less dramatic (Tnfα, Il-10 or Fizz1) than the M(LPS/IFNγ) macrophages treatment in vitro (Fig. 3.1a) or were not significantly different between genotypes (iNos, Arg1 or Il-6) (Fig. 5f). Even so, a robust increase in MCP1 secretion and significantly decreased ARG1 enzymatic activity compared to WT BMDMs further confirmed the proinflammatory phenotype of the Rac2−/− macrophages (Fig. 5g,h). However, Rac2−/− eGFP BMDMs still formed tubes resembling TNTs consisting of actin and tubulin cytoskeletons (Fig. 3.5i) found lying above the substratum surface (data not shown). Taken together, these results indicate that while the polarization phenotype of Rac2−/− eGFP+ BMDMs is skewed towards a M(LPS/IFNγ) phenotype, both formation of TNT-like protrusions and Rac2−/− HSPCs transplantation efficacy remain unaffected.

Figure 3.5: Enrichment of proinflammatory macrophages in vivo by transplantation of Rac2−/− HSPCs has no effect on efficacy in Ctns−/− mice or on BMDM TNT formation in vitro. (a) Histograms representing cystine content in spleens, livers and female kidneys as measured by mass spectrometry in Ctns−/− mice transplanted with WT HSPCs (n = 5), Ctns−/− HSPCs (n = 4), and Rac2−/− HSPCs (n = 4). Only female kidneys are shown, as previous observations indicate that kidneys need to be analyzed by sex16, and only 2 males were in the smallest recipient group. (b) mRNA quantitation of murine Ctns expression of transplanted Ctns−/− mice in spleen, liver and kidney. Histograms represent changes in Ctns expression relative to housekeeping control Gapdh. (c) Representative confocal micrograph of kidney sections of Ctns−/− mice transplanted with either WT or Rac2−/− HSPCs (green), probed with the macrophage marker F4/80 (red) and the nuclear stain DAPI (blue). Arrows indicate colocalization between eGFP HSPC progeny and F4/80 expression. (d) Confocal micrograph depicting kidney sections of a Ctns−/− mouse transplanted with WT (top) or Rac2−/− (bottom) eGFP HSPCs reveals thin eGFP TNT-like protrusions extending away from the cell body. Frozen sections were stained with anti-GFP to enhance visibility of HSPC progeny, and then probed with rhodamine phallodin to highlight actin within TNT-like structures (arrows). Scale bars: 10 μM. (e) BMDMs isolated from WT or Rac2−/− bone marrow were co-cultured with Ctns−/− DsRed+ fibroblasts and assesed for frequency of protrusions using automated analysis software (see Supplemental Fig. S1). Histogram displays quantification of percentage of BMDMs positive for protrusions (n = 3). Scale bar: 500 μM. (f) Bar graph displays mRNA expression of each individual pro- and anti-inflammatory macrophage polarization gene relative to housekeeping control Gapdh in WT or Rac2−/− BMDMs (n = 3). (g) Bar graph shows measurement of proinflammatory MCP1 cytokine secretion in conditioned media derived from WT or Rac2−/− BMDMs assessed using ELISA (n = 3). (h) Bar graph represents colorimetric measurements of M(IL-4/IL-10) marker ARG1 enzymatic activity in WT or Rac2−/− BMDMs normalized by comparison to blank with a standard curve (n = 3). (i) Confocal micrograph of Rac2−/− BMDM cytoskeletal immunostaining of tubulin (green) and actin (red) reveals some Rac2−/− BMDM protrusions only have actin (arrowhead) with others also containing tubulin (arrows). All scale bars are 10 μM except otherwise noted. All graphs shown as mean ± SD. P values were determined by one-way ANOVA or students t-tests. *$P < 0.05$, **$P < 0.01$, ***$P < 0.001$, ****$P < 0.0001$.

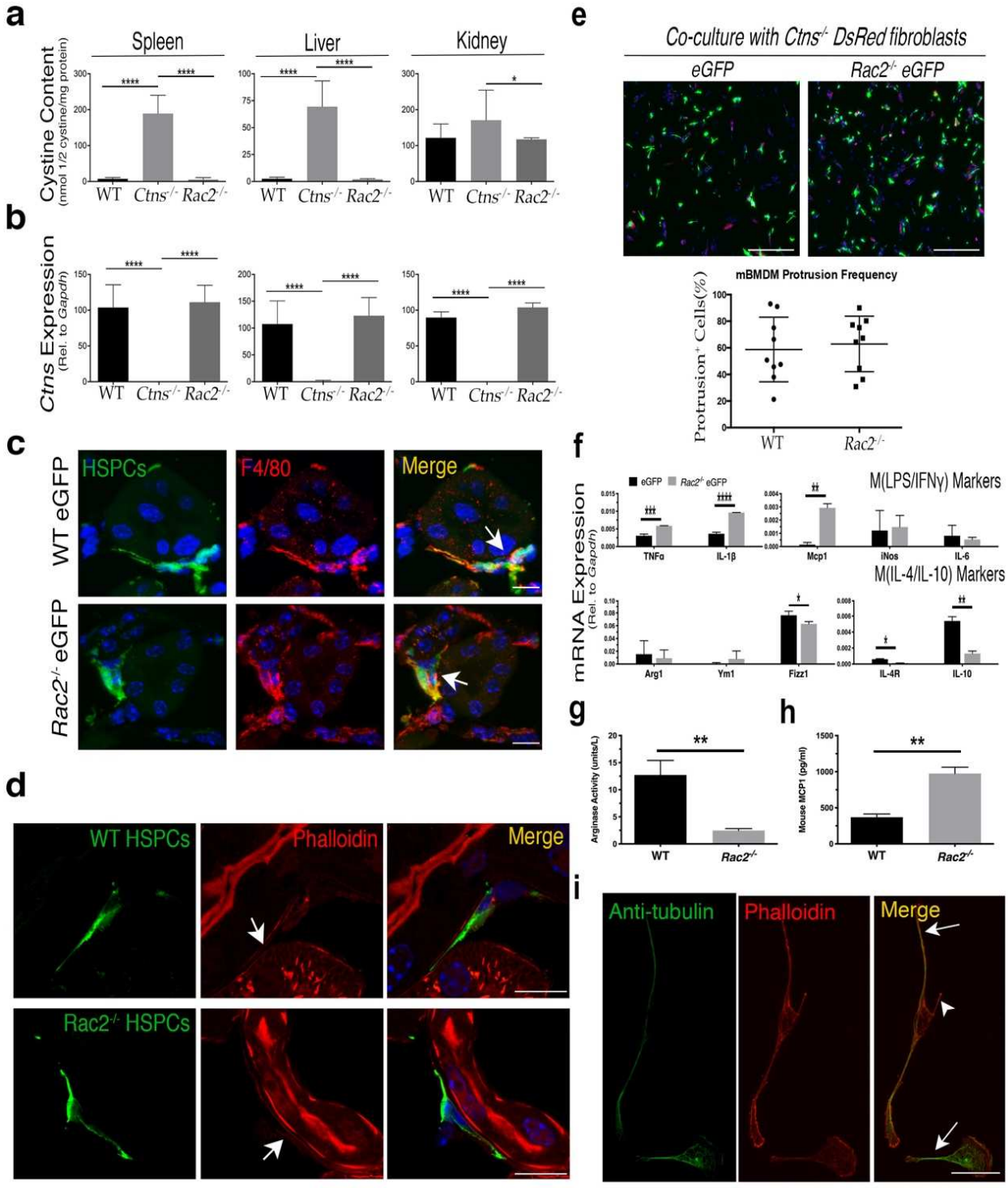
a
Spleen
Liver
Kidney
Cystine Content
(nmol 1/2 cystine/mg protein)
WT
Ctns-/-
Rac2-/-
b
Ctns Expression
(Rel. to Gapdh)
c
WT eGFP
Rac2-/- eGFP
HSPCs
F4/80
Merge
d
WT HSPCs
Phalloidin
Merge
Rac2-/- HSPCs
e
Co-culture with Ctns-/- DsRed fibroblasts
eGFP
Rac2-/- eGFP
mBMDM Protrusion Frequency
Protrusion+ Cells(%)
f
mRNA Expression
(Rel. to Gapdh)
eGFP
Rac2-/- eGFP
M(LPS/IFNγ) Markers
TNFα
IL-1β
Mcp1
iNos
IL-6
M(IL-4/IL-10) Markers
Arg1
Ym1
Fizz1
IL-4R
IL-10
g
Arginase Activity (units/L)
h
Mouse MCP1 (pg/ml)
i
Anti-tubulin
Phalloidin
Merge

3.1.3: Discussion

In the present study, we investigated the phenotype of the HSPC-derived macrophages responsible for intercellular trafficking through TNTs. Several decades of research into macrophage subpopulations has elucidated differences in cytokine production, glucose metabolism, secondary messengers, stimulatory conditions, cellular morphology and numerous other factors which collectively lead to differences in macrophage biological activity, potentially including TNT-mediated trafficking (27,28). Using established assays in conjunction with novel imaging workflows, we observed a reduction in TNT formation and organelle transfer following LPS/IFNγ polarization, suggesting optimal TNT trafficking is impaired with increased proinflammatory stimulation. Unlike other imaging analysis platforms, our protrusion detection methodology requires no antibody staining or fixation and can function at relatively low magnification (40x), enabling large numbers of cells to be quickly and automatically analyzed without bias (47,48). Development of these tools not only increased our understanding of the morphological dynamics of macrophage polarization but also highlighted the potential for further study of cellular protrusion dynamics. This ImagePro Premier workflow could potentially allow quantitative analysis of other fluorescently-labeled cellular extensions such as filopodia, neuronal axons, or invadopodia in cancer.

Following HSPC transplantation in vivo, tissue-integrated macrophages appeared to adopt a predominantly proinflammatory phenotype (Supplemental Fig. S8). In addition, HSPCs isolated from the Rac2−/− mouse model were enriched for a M(LPS/IFNγ) macrophage population but appeared to be as efficient in rescuing cystine build-up in the Ctns−/− mice as WT HSPCs. Our findings correlate with a recent study that demonstrated increased recruitment of proinflammatory

immune cells in cystinosis, further highlighting the crucial role that inflammation plays in this disorder (49). In addition, the dissonance between our in vitro and in vivo results reflects mounting evidence that the in vitro paradigm of macrophage activity can be a potentially misleading oversimplification (25). Further studies applying similar methodology to more complex in vitro models such as 3D culturing or iPSC-derived organoids or spheroids may help to bridge the gap between findings from cell culture and mouse models. That said, in vitro polarization can easily push cells beyond physiological levels of polarization. For example, the mRNA expression of important inflammatory mediators, including the master cytokine regulator TNFα, increased in M(LPS/IFNγ) IC-21 macrophages by over an order of magnitude; however, the magnitude of increase between Rac2−/− and WT BMDMs was far more modest. In terms of TNT-like protrusion formation, the reduced disruption of polarization induced by lack of RAC2 might be mitigated by redundant pathways or signaling. Alternatively, these results could show that RAC2 itself has no role in TNT formation. In contrast, siRNA-mediated knockdown of RAC1 results in a reduction of TNTs (50). Although the two proteins are quite similar (92%), Miskolci et al. report substantial differences in their subcellular localization – upon stimulation, RAC1 is primarily localized to the periphery, while RAC2 was distributed throughout the cell (51,52). Altogether, these data reveal that induction and function of TNT-like protrusions can be achieved by macrophages across the physiological spectrum of polarization, but is impaired when exogenous stimulation pushes cells to an extreme physiological state.

Like all cellular protrusions, TNTs require extensive modification and reorganization of the cytoskeleton to distort the plasma membrane and generate the protrusive force necessary to reshape the cell, elongate, and dynamically maintain the protrusion once formed1. Evidence also strongly implicates macrophage polarization in differentially modulating cytoskeletal dynamics

and reorganization (53,54). These shared pathways suggest polarization-induced alterations in expression and/or activity of TNT-regulator proteins could be responsible for the reduction in TNT-like protrusion formation following proinflammatory stimulation. We observed a reduction in M(LPS/IFNγ) BMDM mRNA expression of the known TNT inducer Lst1 which acts as a scaffold to recruit many proteins including filamin and the small GTPase RalA to the plasma membrane in order to generate and maintain TNTs (55) (Supplemental Fig. S4). We also observed that proinflammatory BMDMs have decreased mRNA expression of Cdc42, a Rho-family GTPase involved in macrophage polarization which binds N-WASP to control actin branching through Arp2/3 (42,56). In macrophages along with Jurkat and HeLa cells, inhibition of Cdc42 reduces TNT formation and intercellular trafficking (39,50,57). Interestingly, in neurons Cdc42 actually negatively regulates TNTs and trafficking while promoting filopodial formation51. While one can speculate that the reduction of M(LPS/IFNγ) protrusion formation could be due to the increase of Lst1 disrupting normal formation of membrane focal points and/or because of the decrease of Cdc42 actin branching activity, drawing such mechanistic conclusions requires far more evidence than mRNA marker expression. That said, even though a direct connection between these expression changes and TNTs remain unclear, our data does support the central role of actin regulating Rho-family GTPases in TNT formation and provides further evidence of their involvement in macrophage polarization.

A major functional consequence of proinflammatory macrophage polarization was also a clear reduction in intercellular trafficking following induction of this phenotype (Fig. 3). Macrophages specifically are known to frequently form TNTs that are “thicker” and contain a tubulin core in addition to actin, which are known to be responsible for organelle trafficking7,26. Correspondingly, we observed an increase in protrusion frequency, size, length and elongated

shape when BMDMs were cultured with cystinotic cells compared to macrophages alone (Fig. 2d,e). This observation combined with the shared reduction of trafficking and TNT-like protrusion formation following in vitro LPS/IFNγ polarization strongly supports the idea that TNTs form a major artery of intercellular delivery of lysosomes and mitochondria. Interestingly, not only were more cystinosin-eGFP-bearing lysosomes delivered to the diseased cells, which lack the lysosomal transmembrane protein cystinosin, but an increase in transfer of frataxin-eGFP-bearing mitochondria was also observed to cystinotic cells. Two hypotheses could explain these findings: (i) TNTs facilitate widespread delivery of cellular organelles to diseased cells so the fact that there are more thick TNTs inevitably leads to more trafficking of all cargos. No known TNT "gating" mechanisms have been identified to disprove this hypothesis, although overall protrusion structure has been shown to affect the types of molecular cargos transferred26; (ii) Cystinosis also causes mitochondrial dysfunction characterized by dysregulation of the cyclic AMP cycle and impaired autophagy (58,59). Therefore, it is also possible that whatever unknown media-soluble factor(s) causing increased TNT-like protrusion formation and thicker morphology also stimulates transfer of mitochondria as well as lysosomes. Whatever the cause may ultimately be, the finding that diseased cells increased macrophage-derived thick TNT formation and intercellular trafficking activity represents exciting new possibilities for the study of TNTs. A major thread of research from numerous groups has focused on how TNTs are involved in the transfer of harmful pathogenic molecules – ranging from HIV infection in T cells to cancer cell invasion to spreading misfolded tau protein aggregates (17,34,60). Thus, our findings that diseased cystinotic cells cause macrophages to increase TNT-mediated trafficking highlights the idea of TNTs as delivery system for regenerative medicine as opposed to mediating the spread of deleterious agents.

In this study, we investigated the phenotype of macrophages responsible for the widespread dissemination of molecular cargo via TNTs both in vitro and in vivo. We developed novel imaging tools allowing for automatic and unbiased quantification of cellular protrusions as well as intercellular trafficking efficacy in order to investigate these behaviors in the context of polarized macrophages. Given the apparent widespread and versatile nature of macrophage TNT transport, it is likely that many molecular products beyond functional lysosomes or mitochondrial proteins are transferred via TNTs; cargos that may not be readily secreted and thus be more difficult to deliver widely. Thus, understanding the mechanisms and cellular type that are responsible for TNT-mediated delivery will enhance the efficacy of numerous potential ex vivo therapeutic approaches targeting a wide variety of loss-of-function organelle disorders.

3.1.4: Methods

Mice and ethics statement. C57BL/6 Rac2−/− mice were provided by Dr. Durden (Moores Cancer Center, University of California, San Diego) and C57BL/6 Ctns−/− mice were provided by Dr. Antignac (Inserm U983, Paris, France). Enhanced green fluorescent protein (eGFP; C57BL/6-Tg(ACTB-EGFP)1Osb/j) and DsRed (B6.Cg-Tg(CAG-DsRed*MST)1Nagy/J) transgenic mice were purchased from The Jackson Laboratory (Bar Harbor, ME). Ctns−/− mice were cross-bred to both DsRed and GFP to produce Ctns−/− strains constitutively expressing either DsRed or GFP reporter genes as previously described14,16. All strains and mouse procedures were approved by the University of California, San Diego (UCSD) in accordance with the guidelines set forth by the Institutional Animal Care and Use Committee (Protocol ID S12288).

Macrophage and fibroblast isolation and culture. BMDMs were isolated from C57BL/6 mice according to standard protocols as described previously61. Briefly, mice were sacrificed using isoflurane, femurs and tibias were removed, and bone marrow was flushed using PBS with 1% fetal bovine serum (FBS). Cells were cultured at 37 °C and 5% CO2 in complete RPMI-1640 media (10% FBS, 2% penicillin/streptomycin) supplemented with 20% mCSF-containing L929-conditioned medium for seven days on tissue-culture (TC) treated plastic, with a media change at day 3. BMDMs were grown for no more than three passages and subcultured by scraping. For in vitro polarization experiments, BMDMs or IC-21 were cultured for at least 48 hours in complete media with either 100 ng/mL LPS and 50 ng/mL IFNγ or 10 ng/mL IL-4 and IL-10 (BioLegend) for M(LPS/IFNγ) and M(IL-4/IL-10) polarization, respectively. Primary fibroblasts were isolated from neonatal mouse skin biopsies by allowing them to grow out of small skin pieces (~0.5 cm2)

attached to the culture dishes for several days prior to skin removal and subculture in complete DMEM media (10% FBS, 2% penicillin/streptomycin).

Co-culture growth and imaging. 75,000 macrophages and 50,000 fibroblasts were cultured together in 6-well dishes under polarization conditions for two days. Cells were washed with warm PBS and fixed for 10 mins at 37 °C in 4% paraformaldehyde (PFA). Cells were washed in PBS again and imaged at 40X on the BZX-700 Fluorescent Microscope (Keyence). Five large image stitches (5 × 5) were generated per experimental condition, with acquisition settings held constant within experimental runs.

Imaging analysis: protrusion quantification. Stitched images were calibrated in ImagePro Premier (Media Cybernetics) for automated quantification of protrusion frequency. eGFP+ macrophages were size-selected by filtration of objects with an area 100 μm2 or larger and then masked to reduce noise artifacts (Supplemental File 2, Supplemental Fig. S1a, Step I). Protrusions were isolated by repeatedly passing a morphological erosion filter (2 × 2 square, 7 passes) over the image which erased peripheral cellular signal, followed by applying a dilation that restored signal to the central cell body (Step II). Subtracting the processed image from the original mask resulted in selection of regions protruding from the main cell body, which can be filtered by a highly variable set of size parameters to yield either thin TNT-like structures or other thicker protrusions (Supplemental File 2, Supplemental Fig. S1b) (filters for TNTs: 20 μm2 minimum area, 10 μm2 minimum longest axis, 0.6 maximum circularity, 1.9 box area minimum). Finally, the selected protrusion area was overlaid with the original image and cells were classified as either protrusion-positive or -negative based on signal intensity; overlap of protrusion and cell body yielded a

positive result (Step III - IV). All segmentation, adjustment and filtration factors were trained and optimized blind to condition and applied automatically to batch images using ImagePro Premier macros.

Imaging analysis: transfer quantification. Stitched images were imported as above and split into "donor" and "recipient" (DsRed) channels. Donors included genetically-encoded, fluorescently-labeled organelles like cystinosin-eGFP lysosomes and frataxin-eGFP mitochondrial protein, as well as transient stains (for example, Wheat Germ Agglutin (WGA) labels of the plasma membrane). Recipient cell outline was selected (minimum area 100 μm2) and applied as a region of interest (ROI) to the donor channel. Any signal within this ROI was adjusted and selected, taking caution to use controls lacking any donor signal to establish fluorescent background (Supplemental File 2, Supplemental Fig. S3b, top). Filtered donor signal was combined with original recipient outline and signal overlap was used again to classify recipients as donor-positive or -negative. Exclusion of any signal at the boundary of recipient cells, as well as size filtration of donor molecules (maximum area 25 μm2), helped reduce false-positive imaging artifacts.

Flow cytometry. Co-cultures were seeded as described previously, but onto non-tissue culture-treated plastics to enable trypsinization of macrophages. Co-cultures were washed in ice-cold PBS, trypsinized at room temperature (RT) and rapidly rinsed in cold media before centrifugation at 4 °C. Cells were resuspended in cold PBS and vortexed, then run through the BD Accuri C6 cytometer (BD Biosciences). Debris was filtered by SSC/FSC gating with 50,000 cellular events collected. Macrophages and fibroblasts without any fluorescent tags were used to establish an exclusion region from final co-culture sort, while eGFP+, DsRed+ and dual-positive gates were

drawn with each cell type seeded alone. For macrophage polarization markers, BMDMs were polarized as described, then scraped and resuspended in ice cold FACS buffer (1% FBS, 0.1% sodium azide in PBS). Cells were treated with Fc block (BD Biosciences) for 10 mins before incubation for 1 hr on ice in the dark with appropriate antibodies. Cells were washed three times in FACS buffer before immediately reading on the cytometer. Antibodies are as follows: F4/80 PE (Biolegend 565410), CD80 FITC (Biolegend 104706), CD126/IL6Rα APC (115811), CD206 PE (Biolegend 141795).

Quantitative PCR. To measure gene expression in BMDMs/IC-21 and explanted tissues, total RNA was extracted with TRIzol Reagent (Invitrogen) per manufacturer's recommendations. A total of 1 μg isolated RNA was reverse transcribed into cDNA with the iScript cDNA synthesis kit (Bio-Rad). Real-time PCR was performed using iTaq Universal SYBR Green on a CFX96 thermocycler (Bio-Rad) under the following conditions: 95 °C (30 s), 40 cycles of 95 °C (5 s) and 60 °C (30 s), then 65 °C (5 s) and finally 95 °C (5 s). Reaction mixture consisted of 3 μL cDNA (5 ng/ul), 0.6 μL forward and reverse primer (10 μM), 1.8 μL H20 and 5 μL SYBR green. Samples were normalized to Glyceraldehyde 3-phosphate dehydrogenase (Gapdh) and analyzed according to the delta/delta Ct method. All primer sequences are shown in Supplemental Table S1.

Immunoblotting. Total protein was harvested and resuspended in 1% SDS from cultures of 1 × 106 BMDMs and IC-21 using TRIzol Reagent (Invitrogen) per manufacturers protocol and quantified using the Pierce BCA Protein Assay kit (Thermo Fisher Scientific). 10–20 μg of protein was subjected to SDS-PAGE, transferred to a PVDF membrane, blocked in 5% Protein Blocking Reagent (Azure) for 1 hr at RT and then probed overnight with primary antibodies at 4 °C.

Antibodies included M(LPS/IFNγ) markers iNOS (abcam ab3523; 1:1,000) and MCP1(CST 2029S; 1:500), M(IL-4/IL-10) markers ARG1 (Santa Cruz sc-20150; 1:200), CD206 (abcam ab64693; 1:500), macrophage marker CD68 (abcam ab53444; 1:500) and loading control Gapdh (abcam ab8245; 1:1,000). The following day, blots were washed three times in Protein Wash Buffer (Azure) and probed with HRP-conjugated secondary antibody of the appropriate species at 1:2,500 for one hour at room temperature. Blots were then washed three times in Protein Wash Buffer and once with TBS, developed with Radiance Plus ECL Reagent (Azure), and imaged on the c600 Imager (Azure).

ELISA and arginase activity assays. Conditioned media for ELISA experiments were generated by culture of 200,000 IC-21 or BMDM in polarization media for two days and then centrifuged at 2,000 g for 10 mins to remove cell debris. MCP1 SimpleStep ELISA (abcam ab208979) was performed on 1:2,000 diluted media in duplicate per manufactures recommendation. Arginase enzymatic activity was quantitated using 1 × 106 polarized macrophages using a colorimetric assay according to manufactures protocol (Sigma-Aldrich).

Cell proliferation and apoptosis. Metabolically active cells were measured using the Cell Proliferation Reagent WST-1 (Roche) by seeding 5,000 IC-21 or BMDMs in 100 μL per well in triplicate in two identical 96 well plates. After treatment, 10 μL of WST-1 was added to all cell and blank wells of one plate, while the other was changed back into normal macrophage media. Absorbance was measured at 260 nm, following one hour of incubation and a corresponding standard curve was generated with blank-subtracted values normalized to untreated controls. The other plate was processed identically several days later.

Cytochalasin B. Cytochalasin B (Sigma) was diluted from stock to form 1,000X solution in DMSO and seeded with 100,000 macrophages. Treated and control cells were imaged as above at 24 hours post-seeding, followed by a drug washout with fresh media. At 24- and 48-hour post-removal, cells were again imaged at the same locations.

Immunofluorescence. Cells were seeded onto glass coverslips for high-resolution imaging. After growth, cells were rinsed in PBS and fixed in warm 4% PFA for 15 min at 37 °C. Cells were blocked in blocking buffer (1% BSA, 5% goat serum, 0.3% triton X-100) for 1 hour at RT, and probed with primary anti-tubulin antibody (abcam ab6160; 1:500) diluted in antibody buffer (1% BSA, 0.3% triton X-100) overnight at 4 °C. Following three washes of PBS, cells were incubated in secondary antibody and phalloidin (1:200) for 1 hour at RT. Cells were again rinsed, mounted on glass overnight in Prolong Gold with DAPI (Invitrogen), and imaged the following day.

HSPC isolation, transplantation, and cystine measurements. HSPCs were isolated and transplanted into lethally irradiated recipient mice as previously described (16). In brief, bone marrow cells were flushed from the tibia and femurs of 6 to 8-week old WT, Ctns−/− and Rac2−/− eGFP mice. HSPCs were isolated by immunomagnetic separation using magnetic beads conjugated to anti-ScaI antibody (Miltenyi Biotec). Isolated HSPCs were directly transplanted via tail vein injection of 100 μL containing 1 × 106 HSPCs into Ctns−/− mice subjected to a lethal 7 Gy irradiation the previous day. Engraftment was assessed by percentage of eGFP+ cells in peripheral blood at 2- and 4-month post-transplantation. At six months post-transplantation, recipient mice were sacrificed and kidney, liver, and spleen samples were isolated and analyzed

by qPCR and mass spectrometry for murine Ctns expression and overall cystine load as previously described15.

Statistics. All statistical analyses were performed in Prism (GraphPad). Student's t-test was performed for comparisons of two groups, while one-way analysis of variance (ANOVA) was employed for comparisons of three or more conditions. Outliers were identified and excluded from larger protrusion measurement dataset by the ROUT method62. All graphs display mean ± standard deviation.

3.1.5: Acknowledgements

Chapter 3.1, in whole, is a reprint of the material as it appears in *Goodman, S., Naphade, S., Khan, M., Sharma, J. & Cherqui, S. Macrophage polarization impacts tunneling nanotube formation and intercellular organelle trafficking. Sci Rep 9, 14529, doi:10.1038/s41598-019-50971-x (2019).* The dissertation author was the primary investigator and author of this paper.

3.1.6: References

1. Ariazi, J., A. Benowitz, V. De Biasi, M.L. Den Boer, S. Cherqui, H. Cui, N. Douillet, E.A. Eugenin, D. Favre, S. Goodman, K. Gousset, D. Hanein, D.I. Israel, S. Kimura, R.B. Kirkpatrick, N. Kuhn, C. Jeong, E. Lou, R. Mailliard, S. Maio, G. Okafo, M. Osswald, J. Pasquier, R. Polak, G. Pradel, B. de Rooij, P. Schaeffer, V.A. Skeberdis, I.F. Smith, A. Tanveer, N. Volkmann, Z. Wu, and C. Zurzolo, *Tunneling Nanotubes and Gap Junctions-Their Role in Long-Range Intercellular Communication during Development, Health, and Disease Conditions.* Front Mol Neurosci, 2017. **10**: p. 333.

2.Rustom, A., R. Saffrich, I. Markovic, P. Walther, and H.H. Gerdes, *Nanotubular highways for intercellular organelle transport.* Science, 2004. **303**(5660): p. 1007-10.

3.Wang, X., M.L. Veruki, N.V. Bukoreshtliev, E. Hartveit, and H.H. Gerdes, *Animal cells connected by nanotubes can be electrically coupled through interposed gap-junction channels.* Proc Natl Acad Sci U S A, 2010. **107**(40): p. 17194-9.
4.Gousset, K., L. Marzo, P.H. Commere, and C. Zurzolo, *Myo10 is a key regulator of TNT formation in neuronal cells.* J Cell Sci, 2013. **126**(Pt 19): p. 4424-35.

5.Chinnery, H.R., E. Pearlman, and P.G. McMenamin, *Cutting edge: Membrane nanotubes in vivo: a feature of MHC class II+ cells in the mouse cornea.* J Immunol, 2008. **180**(9): p. 5779-83.

6.Gurke, S., J.F. Barroso, E. Hodneland, N.V. Bukoreshtliev, O. Schlicker, and H.H. Gerdes, *Tunneling nanotube (TNT)-like structures facilitate a constitutive, actomyosin-dependent exchange of endocytic organelles between normal rat kidney cells.* Exp Cell Res, 2008. **314**(20): p. 3669-83.

7.Naphade, S., J. Sharma, H.P. Gaide Chevronnay, M.A. Shook, B.A. Yeagy, C.J. Rocca, S.N. Ur, A.J. Lau, P.J. Courtoy, and S. Cherqui, *Brief reports: Lysosomal cross-correction by hematopoietic stem cell-derived macrophages via tunneling nanotubes.* Stem Cells, 2015. **33**(1): p. 301-9.

8.Rocca, C.J., A. Kreymerman, S.N. Ur, K.E. Frizzi, S. Naphade, A. Lau, T. Tran, N.A. Calcutt, J.L. Goldberg, and S. Cherqui, *Treatment of Inherited Eye Defects by Systemic Hematopoietic Stem Cell Transplantation.* Invest Ophthalmol Vis Sci, 2015. **56**(12): p. 7214-23.

9.Gaide Chevronnay, H.P., V. Janssens, P. Van Der Smissen, C.J. Rocca, X.H. Liao, S. Refetoff, C.E. Pierreux, S. Cherqui, and P.J. Courtoy, *Hematopoietic Stem Cells Transplantation Can Normalize Thyroid Function in a Cystinosis Mouse Model.* Endocrinology, 2016. **157**(4): p. 1363-71.

10.Kalatzis, V., S. Cherqui, C. Antignac, and B. Gasnier, *Cystinosin, the protein defective in cystinosis, is a H(+)-driven lysosomal cystine transporter.* EMBO J, 2001. **20**(21): p. 5940-9.

11.Emma, F., G. Nesterova, C. Langman, A. Labbe, S. Cherqui, P. Goodyer, M.C. Janssen, M. Greco, R. Topaloglu, E. Elenberg, R. Dohil, D. Trauner, C. Antignac, P. Cochat, F. Kaskel, A. Servais, E. Wuhl, P. Niaudet, W. Van't Hoff, W. Gahl, and E. Levtchenko, *Nephropathic cystinosis: an international consensus document.* Nephrol Dial Transplant, 2014. **29 Suppl 4**: p. iv87-94.

12.Cherqui, S., C. Sevin, G. Hamard, V. Kalatzis, M. Sich, M.O. Pequignot, K. Gogat, M. Abitbol, M. Broyer, M.C. Gubler, and C. Antignac, *Intralysosomal cystine accumulation in mice lacking cystinosin, the protein defective in cystinosis.* Mol Cell Biol, 2002. **22**(21): p. 7622-32.

13.Medic, G., M. van der Weijden, A. Karabis, and M. Hemels, *A systematic literature review of cysteamine bitartrate in the treatment of nephropathic cystinosis.* Curr Med Res Opin, 2017. **33**(11): p. 2065-2076.

14.Syres, K., F. Harrison, M. Tadlock, J.V. Jester, J. Simpson, S. Roy, D.R. Salomon, and S. Cherqui, *Successful treatment of the murine model of cystinosis using bone marrow cell transplantation.* Blood, 2009. **114**(12): p. 2542-52.

15.Yeagy, B.A., F. Harrison, M.C. Gubler, J.A. Koziol, D.R. Salomon, and S. Cherqui, *Kidney preservation by bone marrow cell transplantation in hereditary nephropathy.* Kidney Int, 2011. **79**(11): p. 1198-206.

16.Harrison, F., B.A. Yeagy, C.J. Rocca, D.B. Kohn, D.R. Salomon, and S. Cherqui, *Hematopoietic stem cell gene therapy for the multisystemic lysosomal storage disorder cystinosis.* Mol Ther, 2013. **21**(2): p. 433-44.

17.Eugenin, E.A., P.J. Gaskill, and J.W. Berman, *Tunneling nanotubes (TNT) are induced by HIV-infection of macrophages: a potential mechanism for intercellular HIV trafficking.* Cell Immunol, 2009. **254**(2): p. 142-8.

18.Osswald, M., G. Solecki, W. Wick, and F. Winkler, *A malignant cellular network in gliomas: potential clinical implications.* Neuro Oncol, 2016. **18**(4): p. 479-85.
19.Bruzauskaite, I., D. Bironaite, E. Bagdonas, V.A. Skeberdis, J. Denkovskij, T. Tamulevicius, V. Uvarovas, and E. Bernotiene, *Relevance of HCN2-expressing human mesenchymal stem cells for the generation of biological pacemakers.* Stem Cell Res Ther, 2016. **7**(1): p. 67.

20.Gabriel, S.S., H. Belge, A. Gassama, H. Debaix, A. Luciani, T. Fehr, and O. Devuyst, *Bone marrow transplantation improves proximal tubule dysfunction in a mouse model of Dent disease.* Kidney Int, 2017. **91**(4): p. 842-855.

21.Rocca, C.J., S.M. Goodman, J.N. Dulin, J.H. Haquang, I. Gertsman, J. Blondelle, J.L.M. Smith, C.J. Heyser, and S. Cherqui, *Transplantation of wild-type mouse hematopoietic stem and progenitor cells ameliorates deficits in a mouse model of Friedreich's ataxia.* Sci Transl Med, 2017. **9**(413).

22.Mills, C.D., K. Kincaid, J.M. Alt, M.J. Heilman, and A.M. Hill, *M-1/M-2 macrophages and the Th1/Th2 paradigm.* J Immunol, 2000. **164**(12): p. 6166-73.

23.Ying, W., P.S. Cheruku, F.W. Bazer, S.H. Safe, and B. Zhou, *Investigation of macrophage polarization using bone marrow derived macrophages.* J Vis Exp, 2013(76).

24.Murray, P.J., J.E. Allen, S.K. Biswas, E.A. Fisher, D.W. Gilroy, S. Goerdt, S. Gordon, J.A. Hamilton, L.B. Ivashkiv, T. Lawrence, M. Locati, A. Mantovani, F.O. Martinez, J.L. Mege, D.M. Mosser, G. Natoli, J.P. Saeij, J.L. Schultze, K.A. Shirey, A. Sica, J. Suttles, I. Udalova, J.A. van Ginderachter, S.N. Vogel, and T.A. Wynn, *Macrophage activation and polarization: nomenclature and experimental guidelines.* Immunity, 2014. **41**(1): p. 14-20.

25.Martinez, F.O. and S. Gordon, *The M1 and M2 paradigm of macrophage activation: time for reassessment.* F1000Prime Rep, 2014. **6**: p. 13.

26.Onfelt, B., S. Nedvetzki, R.K. Benninger, M.A. Purbhoo, S. Sowinski, A.N. Hume, M.C. Seabra, M.A. Neil, P.M. French, and D.M. Davis, *Structurally distinct membrane nanotubes between human macrophages support long-distance vesicular traffic or surfing of bacteria.* J Immunol, 2006. **177**(12): p. 8476-83.

27.McWhorter, F.Y., T. Wang, P. Nguyen, T. Chung, and W.F. Liu, *Modulation of macrophage phenotype by cell shape.* Proc Natl Acad Sci U S A, 2013. **110**(43): p. 17253-8.

28.Wang, N., H. Liang, and K. Zen, *Molecular mechanisms that influence the macrophage m1-m2 polarization balance.* Front Immunol, 2014. **5**: p. 614.

29.Tatano, Y., T. Shimizu, and H. Tomioka, *Unique macrophages different from M1/M2 macrophages inhibit T cell mitogenesis while upregulating Th17 polarization.* Sci Rep, 2014. **4**: p. 4146.

30.Van den Bossche, J., W.H. Lamers, E.S. Koehler, J.M. Geuns, L. Alhonen, A. Uimari, S. Pirnes-Karhu, E. Van Overmeire, Y. Morias, L. Brys, L. Vereecke, P. De Baetselier, and J.A. Van Ginderachter, *Pivotal Advance: Arginase-1-independent polyamine production stimulates the expression of IL-4-induced alternatively activated macrophage markers while inhibiting LPS-induced expression of inflammatory genes.* J Leukoc Biol, 2012. **91**(5): p. 685-99.

31.Raggi, F., S. Pelassa, D. Pierobon, F. Penco, M. Gattorno, F. Novelli, A. Eva, L. Varesio, M. Giovarelli, and M.C. Bosco, *Regulation of Human Macrophage M1-M2 Polarization Balance by Hypoxia and the Triggering Receptor Expressed on Myeloid Cells-1.* Front Immunol, 2017. **8**: p. 1097.

32.Souriant, S., L. Balboa, M. Dupont, K. Pingris, D. Kviatcovsky, C. Cougoule, C. Lastrucci, A. Bah, R. Gasser, R. Poincloux, B. Raynaud-Messina, T. Al Saati, S. Inwentarz, S. Poggi, E.J. Morana, P. Gonzalez-Montaner, M. Corti, B. Lagane, I. Vergne, C. Allers, D. Kaushal, M.J. Kuroda, M.D.C. Sasiain, O. Neyrolles, I. Maridonneau-Parini, G. Lugo-Villarino, and C. Verollet, *Tuberculosis Exacerbates HIV-1 Infection through IL-10/STAT3-Dependent Tunneling Nanotube Formation in Macrophages.* Cell Rep, 2019. **26**(13): p. 3586-3599 e7.

33.Sowinski, S., J.M. Alakoskela, C. Jolly, and D.M. Davis, *Optimized methods for imaging membrane nanotubes between T cells and trafficking of HIV-1.* Methods, 2011. **53**(1): p. 27-33.

34.Abounit, S. and C. Zurzolo, *Wiring through tunneling nanotubes--from electrical signals to organelle transfer.* J Cell Sci, 2012. **125**(Pt 5): p. 1089-98.

35.Bukoreshtliev, N.V., X. Wang, E. Hodneland, S. Gurke, J.F. Barroso, and H.H. Gerdes, *Selective block of tunneling nanotube (TNT) formation inhibits intercellular organelle transfer between PC12 cells.* FEBS Lett, 2009. **583**(9): p. 1481-8.

36.Wang, X. and H.H. Gerdes, *Transfer of mitochondria via tunneling nanotubes rescues apoptotic PC12 cells.* Cell Death Differ, 2015. **22**(7): p. 1181-91.

37.Austefjord, M.W., H.H. Gerdes, and X. Wang, *Tunneling nanotubes: Diversity in morphology and structure.* Commun Integr Biol, 2014. **7**(1): p. e27934.

38.Wittig, D., X. Wang, C. Walter, H.H. Gerdes, R.H. Funk, and C. Roehlecke, *Multi-level communication of human retinal pigment epithelial cells via tunneling nanotubes.* PLoS One, 2012. **7**(3): p. e33195.

39.Hase, K., S. Kimura, H. Takatsu, M. Ohmae, S. Kawano, H. Kitamura, M. Ito, H. Watarai, C.C. Hazelett, C. Yeaman, and H. Ohno, *M-Sec promotes membrane nanotube formation by interacting with Ral and the exocyst complex.* Nat Cell Biol, 2009. **11**(12): p. 1427-32.

40.Busi, M.V. and D.F. Gomez-Casati, *Exploring frataxin function.* IUBMB Life, 2012. **64**(1): p. 56-63.

41.Roberts, A.W., C. Kim, L. Zhen, J.B. Lowe, R. Kapur, B. Petryniak, A. Spaetti, J.D. Pollock, J.B. Borneo, G.B. Bradford, S.J. Atkinson, M.C. Dinauer, and D.A. Williams, *Deficiency of the hematopoietic cell-specific Rho family GTPase Rac2 is characterized by abnormalities in neutrophil function and host defense.* Immunity, 1999. **10**(2): p. 183-96.

42.Aflaki, E., N.A. Balenga, P. Luschnig-Schratl, H. Wolinski, S. Povoden, P.G. Chandak, J.G. Bogner-Strauss, S. Eder, V. Konya, S.D. Kohlwein, A. Heinemann, and D. Kratky, *Impaired Rho GTPase activation abrogates cell polarization and migration in macrophages with defective lipolysis.* Cell Mol Life Sci, 2011. **68**(23): p. 3933-47.

43.Joshi, S., A.R. Singh, M. Zulcic, L. Bao, K. Messer, T. Ideker, J. Dutkowski, and D.L. Durden, *Rac2 controls tumor growth, metastasis and M1-M2 macrophage differentiation in vivo.* PLoS One, 2014. **9**(4): p. e95893.

44.Joshi, S., A.R. Singh, S.S. Wong, M. Zulcic, M. Jiang, A. Pardo, M. Selman, J.S. Hagood, and D.L. Durden, *Rac2 is required for alternative macrophage activation and bleomycin induced pulmonary fibrosis; a macrophage autonomous phenotype.* PLoS One, 2017. **12**(8): p. e0182851.

45.Ridley, A.J., *Rho GTPases and actin dynamics in membrane protrusions and vesicle trafficking.* Trends Cell Biol, 2006. **16**(10): p. 522-9.

46.Symons, M., *Rho family GTPases: the cytoskeleton and beyond.* Trends Biochem Sci, 1996. **21**(5): p. 178-81.

47.Rostam, H.M., P.M. Reynolds, M.R. Alexander, N. Gadegaard, and A.M. Ghaemmaghami, *Image based Machine Learning for identification of macrophage subsets.* Sci Rep, 2017. **7**(1): p. 3521.

48.Alfonso-Garcia, A., T.D. Smith, R. Datta, T.U. Luu, E. Gratton, E.O. Potma, and W.F. Liu, *Label-free identification of macrophage phenotype by fluorescence lifetime imaging microscopy.* J Biomed Opt, 2016. **21**(4): p. 46005.

49.Lobry, T., R. Miller, N. Nevo, C.J. Rocca, J. Zhang, S.D. Catz, F. Moore, L. Thomas, D. Pouly, A. Bailleux, I.C. Guerrera, M.C. Gubler, C.W. Wilson, R.H. Mak, T. Montier, C. Antignac, and S. Cherqui, *Interaction between galectin-3 and cystinosin uncovers a pathogenic role of inflammation in kidney involvement of cystinosis.* Kidney Int, 2019.

50.Hanna, S.J., K. McCoy-Simandle, V. Miskolci, P. Guo, M. Cammer, L. Hodgson, and D. Cox, *The Role of Rho-GTPases and actin polymerization during Macrophage Tunneling Nanotube Biogenesis.* Sci Rep, 2017. **7**(1): p. 8547.

51.Delage, E., D.C. Cervantes, E. Penard, C. Schmitt, S. Syan, A. Disanza, G. Scita, and C. Zurzolo, *Differential identity of Filopodia and Tunneling Nanotubes revealed by the opposite functions of actin regulatory complexes.* Sci Rep, 2016. **6**: p. 39632.

52.Miskolci, V., B. Wu, Y. Moshfegh, D. Cox, and L. Hodgson, *Optical Tools To Study the Isoform-Specific Roles of Small GTPases in Immune Cells.* J Immunol, 2016. **196**(8): p. 3479-93.

53.Pergola, C., K. Schubert, S. Pace, J. Ziereisen, F. Nikels, O. Scherer, S. Huttel, S. Zahler, A.M. Vollmar, C. Weinigel, S. Rummler, R. Muller, M. Raasch, A. Mosig, A. Koeberle, and O. Werz, *Modulation of actin dynamics as potential macrophage subtype-targeting anti-tumour strategy.* Sci Rep, 2017. **7**: p. 41434.

54.Jonsson, F., C.B. Gurniak, B. Fleischer, G. Kirfel, and W. Witke, *Immunological responses and actin dynamics in macrophages are controlled by N-cofilin but are independent from ADF.* PLoS One, 2012. **7**(4): p. e36034.

55.Schiller, C., K.N. Diakopoulos, I. Rohwedder, E. Kremmer, C. von Toerne, M. Ueffing, U.H. Weidle, H. Ohno, and E.H. Weiss, *LST1 promotes the assembly of a molecular machinery responsible for tunneling nanotube formation.* J Cell Sci, 2013. **126**(Pt 3): p. 767-77.

56.Higgs, H.N. and T.D. Pollard, *Regulation of actin polymerization by Arp2/3 complex and WASp/Scar proteins.* J Biol Chem, 1999. **274**(46): p. 32531-4.

57.Arkwright, P.D., F. Luchetti, J. Tour, C. Roberts, R. Ayub, A.P. Morales, J.J. Rodriguez, A. Gilmore, B. Canonico, S. Papa, and M.D. Esposti, *Fas stimulation of T lymphocytes promotes rapid intercellular exchange of death signals via membrane nanotubes.* Cell Res, 2010. **20**(1): p. 72-88.

58.Sansanwal, P., B. Yen, W.A. Gahl, Y. Ma, L. Ying, L.J. Wong, and M.M. Sarwal, *Mitochondrial autophagy promotes cellular injury in nephropathic cystinosis.* J Am Soc Nephrol, 2010. **21**(2): p. 272-83.

59.Bellomo, F., A. Signorile, G. Tamma, M. Ranieri, F. Emma, and D. De Rasmo, *Impact of atypical mitochondrial cyclic-AMP level in nephropathic cystinosis.* Cell Mol Life Sci, 2018. **75**(18): p. 3411-3422.

60.Hanna, S.J., K. McCoy-Simandle, E. Leung, A. Genna, J. Condeelis, and D. Cox, *Tunneling nanotubes, a novel mode of tumor cell-macrophage communication in tumor cell invasion.* J Cell Sci, 2019. **132**(3).

61.Zhang, X., R. Goncalves, and D.M. Mosser, *The isolation and characterization of murine macrophages.* Curr Protoc Immunol, 2008. **Chapter 14**: p. Unit 14 1.

62.Motulsky, H.J. and R.E. Brown, *Detecting outliers when fitting data with nonlinear regression - a new method based on robust nonlinear regression and the false discovery rate.* BMC Bioinformatics, 2006. **7**: p. 123.

3.2: Transcriptomic analysis of HSPC derived kidney immune cells

3.2.1: Introduction

Our findings linking macrophage polarization to TNT-like protrusion formation represent a very focused, molecular genetics-based approach at exploring the mechanics and outcomes of intercellular trafficking in the context of cystinosis. Such a strategy has the advantage of understanding the relevant processes – in this case, the effect of polarization on macrophage lysosomal trafficking during co-culture *in vitro* – but is also inherently low-throughput as well as constrained by the limitations of an *in vitro* system, namely difficulty in translation to mice or humans. To complement this approach, and hopefully avoid discordance between *in vitro* and *in vivo* conclusions, as exemplified by the lack of a Rac2 KO HSPC phenotype in Chapter 3.1, we moved to take a more global look at the gene expression profiles of HSPC-derived immune cells from the kidneys of transplanted cystinotic animals.

In collaboration with Dr. Eniko Sajti from Dr. Chris Glass' group, we designed, tested and optimized a complex multichannel FACS panel to isolate various immune populations such as macrophages, monocytes, neutrophils and dendritic cells from the kidney. We then preformed RNAseq upon these samples in an attempt to understand any transcriptional differences between genotypes or cell types. Our initial goal was to use animals transplanted with DsRed HSPCs in conjunction with this panel to lineage trace donor-derived kidney-resident immune cells, and potentially make comparisons to host non-colored cells. However, due to technical challenges at both the FACS and RNAseq stages, this goal proved more elusive than expected. We tried instead to simply compare kidney immune populations between WT and CN mice, without any

transplantation or DsRed. This approach was successful in uncovering several promising differentially expressed genes, but the overall depth and quality of NGS was still sub-optimal.

At the commencement of this project, very little was published in regards to NGS approaches to analyzing kidney macrophages, or immune cells in general. Recent publications using single cell RNAseq as well as bulk sequencing of the entire organ has shown great promise, so an adjustment of our approach is likely necessary to improve sample quality (1-2). Even so, while our effort to gain a global idea of expression profiles of kidney immune cells requires further optimization, we were able to isolate some exciting genes which may play an undiscovered role in cystinosis inflammatory pathogenesis.

3.2.2: Findings

Development of a multichannel FACS panel to isolate HSPC-derived immune populations from the kidney. To begin our investigation of the transcriptome of HSPC-derived kidney resident immune cells, irradiated cystinotic mice were transplanted with DsRed HSPCs at 2-months of age and then allowed to age for 4-6 months as previously described (3). Essential controls included non-transplanted cystinotic littermates as well as age-matched DsRed and WT mice.

Our overall experimental strategy was to sacrifice and perfuse these mice, dissect and decapsulate the kidney, manually mince the organs with a razor blade and then gently digest the kidney slurry into a single cell suspension in a digestion buffer containing collagenase 4, DNAse I and flavoperidol to inhibit RNA transcription during staining and sorting (Figure 3.6 A). We then cleaned up our cell samples by first lysing red blood cells (RBCs) and then using Percoll gradient centrifugation to enrich for larger $CD45^+$ immune cells. Finally, we then stained our cells with a

9-color selection panel (7 antibodies, DsRed, and a viability stain to ensure the validity of our isolated cells; Figure 3.6 B). We also prepared single-stained beads to establish a compensation matrix and full-minus-one controls to determine optimal gating.

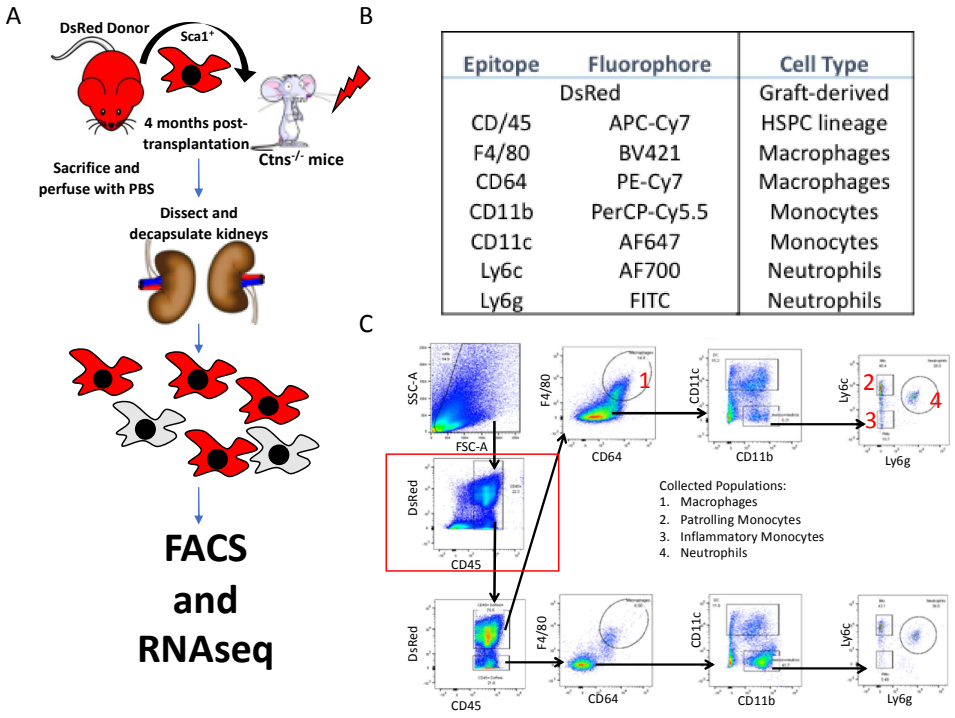

Epitope	Fluorophore	Cell Type
DsRed		Graft-derived
CD/45	APC-Cy7	HSPC lineage
F4/80	BV421	Macrophages
CD64	PE-Cy7	Macrophages
CD11b	PerCP-Cy5.5	Monocytes
CD11c	AF647	Monocytes
Ly6c	AF700	Neutrophils
Ly6g	FITC	Neutrophils

Figure 3.6: Experimental design and FACS gating strategy for isolation of HSPC-derived kidney-resident immune populations. A) Ctns-/- mice were irradiated and transplanted with DsRed HSPCs at ~2 months of age. 4-6 months later, mice were sacrificed and kidneys dissected and gently digested into a single cell suspension, prior to staining for FACS sorting on the Aria II. B) Antibody panel for isolation of HSPC immune progeny including macrophages, monocytes and neutrophils. DsRed served as a marker for donor-derived cells, while Zombie Aqua was used as a live/dead selection. C) Gating strategy to isolate immune populations. Following standard SSC/FSC and live/dead staining, populations were separated according to CD45 and DsRed expression. In transplanted animals, CD45+ cells could be either DsRed positive (donor derived) or DsRed-negative (endogenous host).

Using the AriaII FACS sorter, four populations of cells could be isolated and collected; macrophages, inflammatory monocytes, patrolling monocytes, and neutrophils. Our gating and sorting strategy began by focusing on live cells with were then assessed for the hematopoietic marker CD45 (Figure 3.6 C, boxed graph). Subpopulations of $CD45^{+}$ were then classified based on maker expression, for example $CD64^{+}F4/80^{+}$ cells were collected as macrophages. From transplanted animals, our design allowed sorting based on DsRed positivity, in principle allowing

comparison of donor (Figure 3.6 C, top) *vs*. endogenous (Figure 3.6 C, bottom) cell populations. In the controls, only DsRed negative cells were acquired (WT, untransplanted CN) or positive for the DsRed animals.

We processed four total groups as described, a total of 34 mice consisting 8 DsRed transplanted cystinotic animals, 9 untransplanted cystinotic littermates, 10 WT controls and 7 DsRed controls (Table 3.1). Based on previous experience with low-input RNAseq from cell culture and other tissues, we expected to be able to acquire meaningful data with as few as a thousand cells. Our yield varied widely between cell type – $CD64^{+}F4/80^{+}$ macrophages were promising and the most numerous with usually at least 10,000 cells, while the other three populations were typically an order of magnitude lower. We noted tremendous variability between groups as well, for example $Ly6g^{+}Ly6c^{+}$ patrolling monocytes Part 1 of Group 4 averaged ~16,000, but in Part 2 of Group 5 were extremely rare with an average of 172 cells acquired. Intra-group variation was an issue as well, certain mice had astronomically high neutrophils like DS-BC47L, which likely indicates an inflammatory response to a pathogen. Such variance likely explains the lack of any significant differences between genotypes of either absolute cell count or relative cell percentage of total CD45+ hematopoietic cells (data not shown). Finally, our original design to acquire both DsRed-positive and negative cells from transplanted animals failed due to vanishingly rare DsRed-negative cells – only macrophages were acquirable at all, and even those had a paltry maximum of 1,027 cells.

Table 3.1: RNAseq Trial 1: Immune cell types and yield following FACS sorting of kidneys. Group organization and demographic information such as sex, date of birth and age at death shown in left columns, along with genotype (WT = WT, DS = WT DsRed, CN = untransplanted cystinotic, TRP = cystinotic transplanted with DsRed HSPCs). At right are the four sorted populations and yield from each animal – text in red is DsRed positive cells. In many cases multiple aliquots were frozen for both RNAseq as well as ATACseq analysis – the numbers displayed are for each single RNAseq aliquot.

	UCSD ID	Sex	Genotype	D.O.B	Age (months)	HARVESTED POPULATIONS							
						P1 Cell Type	Count	P2 Cell Type	Count	P3 Cell Type	Count	P4 Cell Type	Count
GROUP 1 (12/20/16)	WT442 RR	M	WT	4/14/16	8.3	Macrophage (DsRed-)	15,826	Inflammatory Monocytes (DsRed-)	6,882	Patrolling Monocytes (DsRed-)	1,330	Neutrophils (DsRed-)	6,231
	DS366R	F	DS	6/24/16	6.0	Macrophage (DsRed+)	18,512	Inflammatory Monocytes (DsRed+)	1,826	Patrolling Monocytes (DsRed+)	3,492	Neutrophils (DsRed+)	4,486
	CN647RL	M	CN	6/2/16	6.7	Macrophage (DsRed-)	12,179	Inflammatory Monocytes (DsRed-)	1,403	Patrolling Monocytes (DsRed-)	213	Neutrophils (DsRed-)	2,764
	CN643L	F	TRP	6/2/16	6.7	Macrophage (DsRed+)	14,879	Inflammatory Monocytes (DsRed+)	331	Patrolling Monocytes (DsRed+)	1,057	Macrophage (DsRed-)	442
GROUP 2 (5/17/17)	WT523L	M	WT	10/31/16	6.6	Macrophage (DsRed-)	11,809	Inflammatory Monocytes (DsRed-)	1,432	Patrolling Monocytes (DsRed-)	542	Neutrophils (DsRed-)	3,393
	WT524RL	M	WT	10/31/16	6.6	Macrophage (DsRed-)	9,906	Inflammatory Monocytes (DsRed-)	1,814	Patrolling Monocytes (DsRed-)	763	Neutrophils (DsRed-)	2,573
	CN712L	M	CN	11/24/16	5.8	Macrophage (DsRed-)	6,460	Inflammatory Monocytes (DsRed-)	1,793	Patrolling Monocytes (DsRed-)	626	Neutrophils (DsRed-)	6,251
	CN713RL	M	CN	11/24/16	5.8	Macrophage (DsRed-)	5,638	Inflammatory Monocytes (DsRed-)	2,299	Patrolling Monocytes (DsRed-)	1,110	Neutrophils (DsRed-)	4,016
	CN708	M	TRP	11/24/16	5.8	Macrophage (DsRed-)	27	Inflammatory Monocytes (DsRed+)	1,418	Macrophage (DsRed+)	5,078	Patrolling Monocytes (DsRed+)	9,413
GROUP 3 (2/13/18)	WT551RR	M	WT	5/17/17	9.1	Macrophage (DsRed-)	15,006	Inflammatory Monocytes (DsRed-)	1,749	Patrolling Monocytes (DsRed-)	369	Neutrophils (DsRed-)	2,321
	WT572RL	M	WT	7/3/17	7.5	Macrophage (DsRed-)	24,721	Inflammatory Monocytes (DsRed-)	4,246	Patrolling Monocytes (DsRed-)	991	Neutrophils (DsRed-)	5,685
	DS392 RL	M	DS (donor)	5/2/17	9.6	Macrophage (DsRed+)	21,019	Inflammatory Monocytes (DsRed+)	4,150	Patrolling Monocytes (DsRed+)	1,082	Neutrophils (DsRed+)	3,201
	DS397R	M	DS (donor)	6/6/17	8.4	Macrophage (DsRed+)	23,680	Inflammatory Monocytes (DsRed+)	2,615	Patrolling Monocytes (DsRed+)	2,757	Neutrophils (DsRed+)	2,724
	CN763RR	M	CN	5/2/17	9.6	Macrophage (DsRed-)	7,446	Inflammatory Monocytes (DsRed-)	2,982	Patrolling Monocytes (DsRed-)	391	Neutrophils (DsRed-)	1,592
	CN-I	M	CN	6/22/17	7.9	Macrophage (DsRed-)	9,544	Inflammatory Monocytes (DsRed-)	1,157	Patrolling Monocytes (DsRed-)	270	Neutrophils (DsRed-)	1,579
	CN 762 L	M	TRP	5/2/17	9.6	Macrophage (DsRed+)	17,060	Macrophage (DsRed-)	1,059	Inflammatory Monocytes (DsRed+)	1,308	Patrolling Monocytes (DsRed+)	627
GROUP 4 Part 1 (11/12/18)	CNAR	M	TRP1	1/18/18	10.5	Macrophage (DsRed+)	13,844	Macrophage (DsRed-)	404	Inflammatory Monocytes (DsRed+)	2,728	Patrolling Monocytes (DsRed+)	13,536
	CNA5-R	M	TRP2	1/18/18	10.5	Macrophage (DsRed+)	39,006	Macrophage (DsRed-)	879	Inflammatory Monocytes (DsRed+)	6,293	Patrolling Monocytes (DsRed+)	43,132
	CNAY-R	M	TRP3	2/18/18	9.4	Macrophage (DsRed+)	21,376	Macrophage (DsRed-)	414	Inflammatory Monocytes (DsRed+)	7,485	Patrolling Monocytes (DsRed+)	20,017
	CNAZ-L	M	TRP4	2/18/18	9.4	Macrophage (DsRed+)	50,933	Macrophage (DsRed-)	902	Inflammatory Monocytes (DsRed+)	7,181	Patrolling Monocytes (DsRed+)	39,049
	DS-BC 47L	M	DS1 (donor)	1/28/18	10.1	Macrophage (DsRed+)	173,867	Inflammatory Monocytes (DsRed+)	8,192	Patrolling Monocytes (DsRed+)	52,346	Neutrophils (DsRed+)	735
	DS-BC 48RL	M	DS2 (donor)	1/28/18	10.1	Macrophage (DsRed+)	99,506	Inflammatory Monocytes (DsRed+)	18,901	Patrolling Monocytes (DsRed+)	103,065	Neutrophils (DsRed+)	6,096
	WT580R	M	WT1	9/3/17	15.0	Macrophage (DsRed-)	116,418	Inflammatory Monocytes (DsRed-)	10,522	Patrolling Monocytes (DsRed-)	787	Neutrophils (DsRed-)	76,239
	GA423	M	WT2	11/14/17	12.6	Macrophage (DsRed-)	29,443	Inflammatory Monocytes (DsRed-)	2,227	Patrolling Monocytes (DsRed-)	570	Neutrophils (DsRed-)	1,242
	GA432	M	WT3	11/14/17	12.6	Macrophage (DsRed-)	76,248	Inflammatory Monocytes (DsRed-)	8,895	Patrolling Monocytes (DsRed-)	1,481	Neutrophils (DsRed-)	8,524
	CNAU-RR	M	CN1	1/18/18	10.5	Macrophage (DsRed-)	18,742	Inflammatory Monocytes (DsRed-)	3,158	Patrolling Monocytes (DsRed-)	883	Neutrophils (DsRed-)	1,557
	CNAW	M	CN2	2/18/18	9.4	Macrophage (DsRed-)	9,769	Inflammatory Monocytes (DsRed-)	2,380	Patrolling Monocytes (DsRed-)	650	Neutrophils (DsRed-)	3,350
GROUP 4 Part 2 (1/10/19)	CN-AT L	F	TRP	1/18/18	11.9	Macrophage (DsRed+)	2,719	Inflammatory Monocytes (DsRed+)	637	Patrolling Monocytes (DsRed+)	349	Macrophage (DsRed-)	179
	DSBC50	F	DS1 (donor)	3/11/18	10.1	Macrophage (DsRed+)	10,938	Inflammatory Monocytes (DsRed+)	2,808	Patrolling Monocytes (DsRed+)	277	Neutrophils (DsRed+)	1,559
	DS2	F	DS2	8/28/18	4	Macrophage (DsRed+)	6,724	Inflammatory Monocytes (DsRed+)	782	Patrolling Monocytes (DsRed+)	196	Neutrophils (DsRed+)	534
	GA426	F	WT1	11/14/17	14	Macrophage (DsRed-)	9,356	Inflammatory Monocytes (DsRed-)	2,315	Patrolling Monocytes (DsRed-)	177	Neutrophils (DsRed-)	459
	GA517	F	WT2	3/25/18	10	Macrophage (DsRed-)	11,932	Inflammatory Monocytes (DsRed-)	1,201	Patrolling Monocytes (DsRed-)	97	Neutrophils (DsRed-)	830
	CN-BA	F	CN1	2/18/18	10.8	Macrophage (DsRed-)	1,070	Inflammatory Monocytes (DsRed-)	1,017	Patrolling Monocytes (DsRed-)	40	Neutrophils (DsRed-)	791
	CN-BB R	F	CN2	2/18/18	10.8	Macrophage (DsRed-)	1,531	Inflammatory Monocytes (DsRed-)	1,059	Patrolling Monocytes (DsRed-)	71	Neutrophils (DsRed-)	609

After samples we returned from the sorter, we carefully lysed cells in Trizol LS to acquire RNA. In many cases, samples were split into aliquots to attempt to maintain relative parity in cell number between genotypes. Samples were frozen at -80^{o}C until we were ready to proceed with NGS analysis.

RNAseq trial I: transplanted animals and controls. After having harvested all four transplant groups, 48 samples were selected for library preparation according to established protocols (4). Samples were submitted for RNAseq at the Institute for Genomic Medicine on the HiSeq 2500. We prepared a selection of all genotypes and cell types, focusing on samples with the highest yield and 2-3 biological replicates per condition.

NGS analysis was performed with the help of the very talented PhD student Rebecca Melton. Initial FASTQC revealed poor quality RNA with possible adaptor contamination. Even after trimming to compensate, a very low percentage of reads actually mapped back to the mouse transcriptome (~10% on average). Much of the rest was either unidentified or bacterial, indicating a potential contamination issue during library preparation. It was unsurprising given the data quality that we did not observe strong expression correlation between supposed biological replicates. Even though macrophages were the "best" data, a heatmap of pairwise correlation shows very few clusters of high correlation, and those that do exist do not track to genotype (Figure 3.7 A).

In an attempt to salvage anything from this dataset, we combined all biological replicates into one sample prior to mapping so that all data for any particular genotype or cell type would be represented as a single sample. Of course, in doing so we lost the ability to preform statistics on replicates. That said, promising data was observed at a single gene level. When we examined the raw number of reads mapping to the Ctns locus, we observed a decrease in untransplanted cystinotic animals compared to all other genotypes (Figure 3.7 B). This indicates at a very basic level that Ctns does not appear to be expressed in cystinotic animals, as expected. We also examined the number of Gapdh reads as a rough normalization and did not detect consistent differences between genotypes (data not shown).

We did examine other potentially differentially expressed genes in addition to Ctns itself. However, the reliability of this data is extremely questionable given the sample quality and extreme processing steps required for analysis. Bearing that in mind, we did generate a list of genes differentially expressed between cell type (Figure 3.7 C). Further conclusions require the ability

to preform statistical analysis between replicates, so unfortunately we are unlikely to be able to go any further with these data.

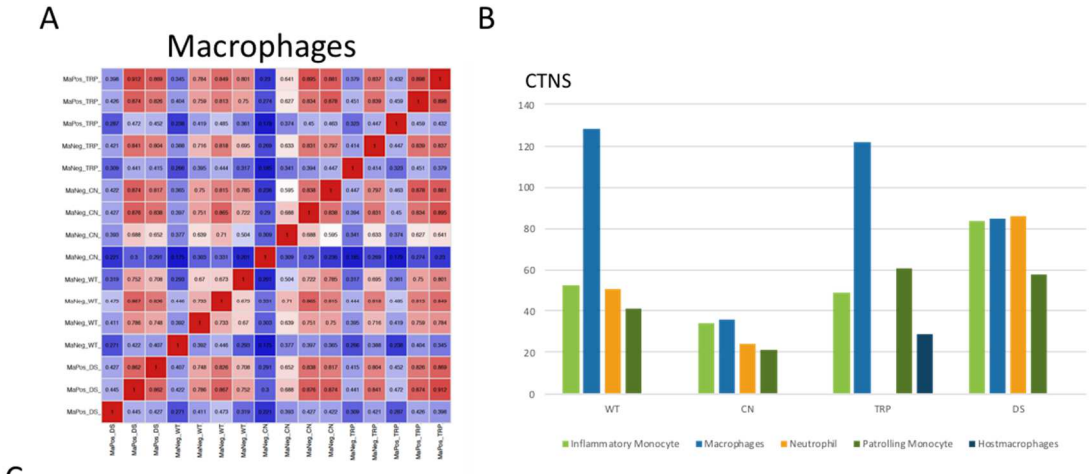

A. Up-Regulated Overlapping Genes						
Hostmacrophage - NeuCN	Cylc1	Xcl1	Wfdc15b	Sostdc1	Egf	Umod
Hostmacrophage - infCN	Retnlg					
MacTRP - NeuCN	Ifi44l	Ugt1a8				
NeuCN - PatCN	Cd200r1	Fnd3c2	Glt28d2	Iqcj	Oog4	Gm11444
NeuCN - infTRP	Gm3139	Ttr				
infCN - infTRP	Slc7a13					

Figure 3.7: Rudimentary transcriptomic analysis of RNAseq Trial 1 samples. A) Heatmap depicting pairwise correlations between different macrophage genotypes. Few clusters of red (r=1) indicate poor correlation in general. B) Number of reads mapping to Ctns locus for different genotypes and cell type. Note that these data were processed so that every biological replicate was mapped as a single sample. Fewer reads in the CN group does indicate a reduction of Ctns expression in the knockouts, as expected. C) Exploratory differential expression mapping. Any conclusions are not statistically validated due to lack of replicates.

Grouped WT v. CN sample acquisition. Our attempts to move forward from these disappointing results were hampered by the still unknown root cause of the sample quality issues. Despite extensive troubleshooting by collaborators, the previously functional low-input RNAseq protocol is no longer operational for both the kidney as well as other projects. While it is possible

that the extraction process from the kidney is uniquely at fault, without the base system working as expected, we cannot troubleshoot in an entirely new organ system.

As an alternative, we decided to pool individual mice together into a single sample to be FACS sorted and proceed with a more standard RNAseq protocol. This approach was designed to increase our cell number and improve the data quality. For the sake of simplifying the system, we simply compared WT and CN mice without any DsRed or transplanted mice in general. While this limits what we can potentially learn, such a strategy is designed to maximize the chance of being able to conclude anything at all. We ran a single group consisting of three pooled samples per genotype, with each sample containing kidneys from 2-3 individual mice (Table 3.2). We collected macrophages, neutrophils and inflammatory monocytes again, but replaced patrolling monocytes with dendritic cells due to a nonfunctional Ly6C antibody. Yields were dramatically improved for macrophages in particular, with other cell types averaging in the low thousands. RNA was processed in Trizol LS as above.

Table 3.2: RNAseq Trial 2: Immune cell types and yield following FACS sorting of Grouped WT v CN kidneys.

	Group	Mouse ID	Sex		DOB	Age at sac (months)	Macrophage yield (P1)	DC Yield (P2)	Monocyte Yield (P3)	Neutrophil Yield (P4)
GROUP 5 WT v CN Grouped (8/29/19)	CN1a	CNDH	M		2/19/19	14.93	~30000	~3.7k	~5.7k	~5.5k
	CN1b	CN78	M		3/13/19	14.20	97,360	9,662	1,639	2,164
		CN79	M		3/13/19	14.20				
	CN2	CN75	F		3/13/19	14.20	61,131	9,439	4,815	4,721
		CN76	F		3/13/19	14.20				
	CN3	CND0	F		3/19/19	14.00	94,424	16,019	10,397	7,661
		CNDP	F		3/19/19	14.00				
		CNDQ	F		3/19/19	14.00				
	WT1	WT648	M		3/4/19	14.50	239,433	15,918	11,574	54,450
		WT663	M		3/4/19	14.50				
	WT2a	KU219	F		4/7/19	13.37	NA			
	WT2b	WT712	F		6/14/19	11.10	38,957	2,426	1,639	2,164
	WT3	DK253	F		4/4/19	13.47	78,715	3,328	3,850	2,615
		DK252	F		4/4/19	13.47				

RNAseq trial 2: Grouped WT v. CN. Library preparation and NGS sequencing was preformed as described above with the addition of a Tapestation quality control check. Only

around ¼ of our samples had reasonable RIN values (>6), exclusively from the macrophages and inflammatory monocytes. Low sample quality is again a perplexing issue – one possibility is that an extended freeze was determinantal. In any case, we prepared and submitted 15 of these samples for sequencing.

Initial QC results were slightly more encouraging than the first trial – we did not detect any likely adaptor contamination and so no trimming was necessary. Furthermore, ~50% of reads mapped back to the mouse reference rather than <10%. However, while we were able to detect ~30,000 unique genes in the first trial, our second run only found ~900 genes, indicating that sequencing depth is quite poor. Technical issues at the sequencing core are potentially responsible as there were difficulties with our initial submission which required re-sequencing.

We initially attempted to use our first RNAseq trial data as a replicate against these new findings, but immediately discarded this idea because any differences in expression between genotypes or cell types were dwarfed by a massive batch effect (data not shown). We therefore only considered data from the second trial, which was more promising. We were able to assess differential expression between replicates without needing to condense to a single sample per genotype (Figure 3.8 A). While we did not see large patterns of expression differences between genotype or cell type, we were able to detect a set of significantly dysregulated genes between WT and CN samples (Figure 3B-C). Of particular interest were a subset of genes which were also independently discovered by DNA array analysis (see Chapter 3.3). We selected these genes – Lyz2, H2-Aa and H2-Eb1 and several others – for further targeted analysis.

A

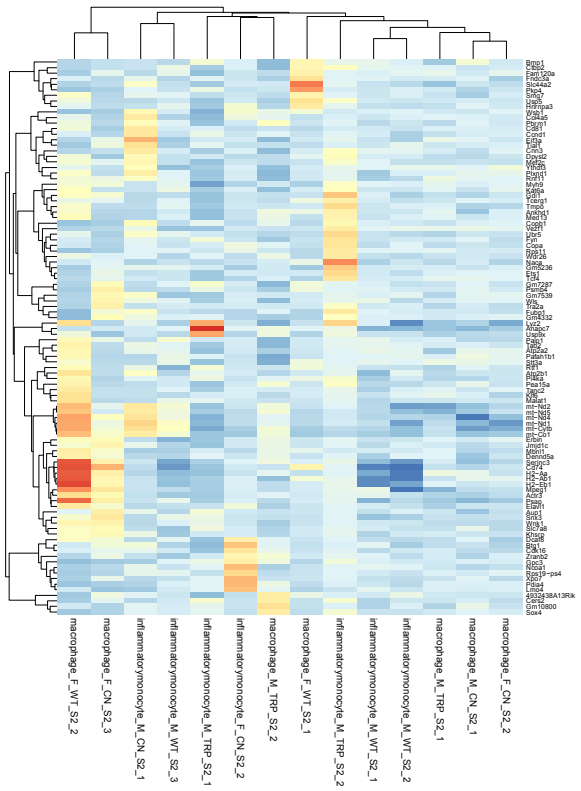

B

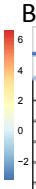

Macrophages: CN v. WT

Gene	logFC	logCPM	F	P	FDR	
H2-Ab1	-4.286	10.681	70.009	2.43E-15	2.25E-12	Down
H2-Eb1	-5.085	11.003	49.981	6.34E-08	2.93E-05	Down
Slc44a2	-3.731	9.932	26.471	1.38E-06	0.0000424	Down
Lyz2	-3.993	11.109	23.732	3.92E-06	0.000906	Down
Serinc3	-5.636	10.401	42.597	5.53E-06	0.00102	Down
Pkp4	-3.345	10.895	17.1	2.30E-04	0.0306	Down
Actr3	-2.76	9.839	13.578	2.33E-04	0.0306	Down

Macrophages: WT v. TRP

Gene	logFC	logCPM	F	P	FDR	
H2-Ab1	5.638	10.681	73.978	4.84E-16	4.47E-13	Up
H2-Eb1	5.248	11.003	39.808	5.26E-07	2.43E-04	Up
Slc44a2	4.477	9.932	26.985	1.12E-06	0.0003449	Up
Lyz2	4.177	11.109	20.164	1.82E-05	0.004202	Up
Serinc3	4.647	10.401	26.017	9.33E-05	0.0172	Up
Sox4	-8.306	10.889	13.311	2.88E-04	0.04445	Down

C

Inflammatory Monocytes: CN v. WT

Gene	logFC	logCPM	F	P	FDR	
Eif3a	3.8402	10.0119	27.3061	1.79E-07	1.65E-04	Up

Inflammatory Monocytes: WT v. TRP

Gene	logFC	logCPM	F	P	FDR	
Lyz2	-5.199	11.108	80.045	1.34E-14	1.23E-11	Down
Usp9x	-4.431	12.345	51.395	3.25E-12	1.50E-09	Down
Anapc7	-7.73	11.72	46.881	1.21E-05	0.00375	Down

Inflammatory Monocytes: CN V. TRP

Gene	logFC	logCPM	F	P	FDR	
Usp9x	-6.226	12.345	28.489	1.52E-07	1.40E-04	Down
Lyz2	-5.378	11.108	22.794	5.82E-06	2.68E-03	Down

Figure 3.8. Transcriptomic analysis of RNAseq Trial 2 samples. A) Heatmap depicting differentially expressed genes between WT and CN macrophages and inflammatory monocytes. B-C) Significantly altered genes with a logFC >2 between genotypes of macrophages (B) or inflammatory monocytes (C).). Transplanted (TRP) samples were acquired in the initial four groups of mice (Table 1) and pooled to run with RNAseq trial 2.

Candidate differentially expressed gene investigation. We designed qPCR primers against differentially expressed genes discovered in our RNAseq analysis. Using RNA isolated from whole WT and CN kidneys, we found that several genes did appear differentially expressed (Figure 3.9 A). We discovered that H2-Ab1 and H2-Eb1, two components of the class II major histocompatibility complex, are upregulated in CN over WT macrophages via RNAseq and also in whole kidney qPCR. These molecules are known to assist in antigen presentation in humoral immunity as well as in contact with polarized T-cell receptors, and deficient mice have been seen to have alterations in MHC II peptide loading (5-8). An upregulation in cystinosis may either be a result of or contribute towards the noted inflammatory aspect of the disease, which our lab has previously linked to the Gal3/MCP1 axis (9). Serinc3, which functions to incorporate serine into

the plasma membrane and plays an important role in restricting HIV infectivity (10-11), is strongly downregulated in whole CN kidney qPCR but upregulated in the RNAseq dataset. Its potential role in cystinosis, while intriguing, is slightly less clear, especially given the differences in directionality of differential expression.

Finally, Lyz2 has been an intriguing molecule to the lab for several years. Lyz2, or Lysozyme C-2, is a bacteriolytic agent against both Gram positive and negative bacteria known to be associated with macrophages (12). Given its active role enhancing immunity, and that we have observed differential expression not only in both inflammatory monocytes and macrophages in our RNAseq data but also previously in a DNA microarray (Chapter 3.4), Lyz2 presents an attractive potential molecular protagonist for inflammation in cystinosis. However, bulk qPCR in the kidney did not detect a difference between WT and CN, although it was trending higher in CN. Again, the discrepancy between the two assays may simply reflect that Lyz2 was enriched in our sorted immune cells. We also tested several other differentially expressed genes from our RNAseq dataset including Slc44a2, Usp9x and Sox4 but observed no significant nor trending differences between genotypes.

We sought to further these experiments beyond mRNA by investigating protein levels or activity. Unfortunately, only one protein had a commercially available antibody – Lyz2. We probed kidney sections of WT and CN mice and observed infrequent puncta signal in both genotypes (Figure 3.9 B). While it is possible that signal is more intense in the WT, this would be difficult to rigorously quantitate due to the relatively rare expression pattern. That said, further experiments into these genes and proteins may serve to highlight some additional as-yet-undiscovered mechanisms by which cystinosis enhances chronic inflammation.

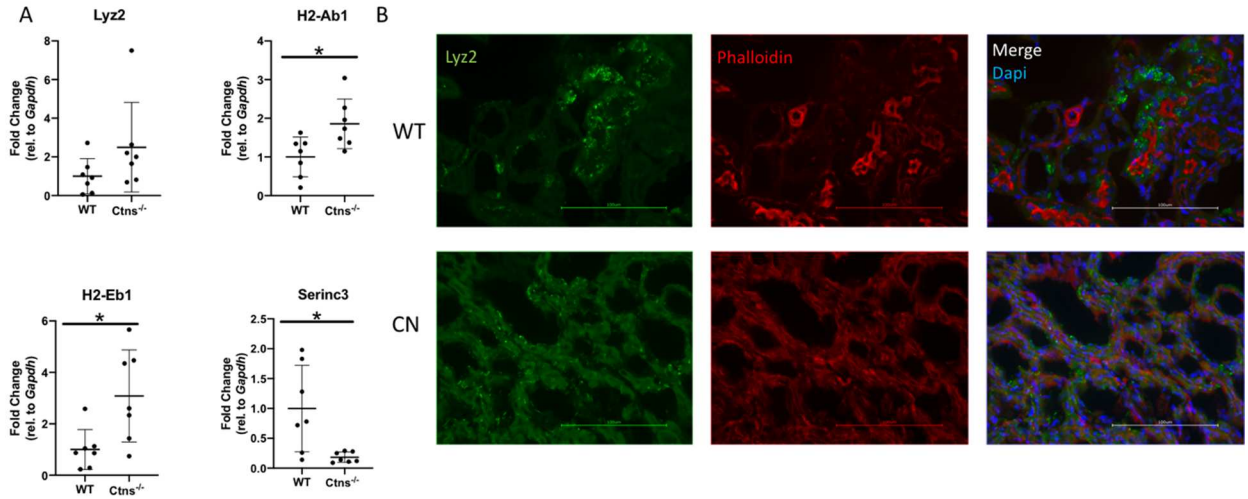

Figure 3.9. Examination of candidate differentially expressed genes between WT and CN. A) qPCR was preformed using gene-specific primers on RNA isolated from whole WT or CN kidneys *=p<0.05. B) Immunofluorescence on frozen kidney sections using anti-Lyz2 antibody (green) and phalloidin (red). Green channels imaged with identical acquisition settings to facilitate quantitation.

3.2.3: Acknowledgements

Chapter 3.2 is based on unpublished work with the coauthors Eniko Sajti, Rebecca Melton, Chris Glass and Stephanie Cherqui. The dissertation author was the primary investigator of this work.

3.2.4: References

1. Zimmerman, Kurt A., Melissa R. Bentley, Jeremie M. Lever, Zhang Li, David K. Crossman, Cheng Jack Song, Shanrun Liu, Michael R. Crowley, James F. George, Michal Mrug, and Bradley K. Yoder. "Single-Cell RNA Sequencing Identifies Candidate Renal Resident Macrophage Gene Expression Signatures across Species." Journal of the American Society of Nephrology 30.5 (2019): 767-81. Print.

2. Clark, Jevin Z., Lihe Chen, Chung-Lin Chou, Hyun Jun Jung, Jae Wook Lee, and Mark A. Knepper. "Representation and Relative Abundance of Cell-type Selective Markers in Whole-kidney RNA-Seq Data." Kidney International 95.4 (2019): 787-96. Print.

3. Syres, Kimberly, Frank Harrison, Matthew Tadlock, James V. Jester, Jennifer Simpson, Subhojit Roy, Daniel R. Salomon, and Stephanie Cherqui. "Successful Treatment of the Murine Model of Cystinosis Using Bone Marrow Cell Transplantation." Blood 114.12 (2009): 2542-552. Print.

4. Sakai, Mashito, Ty D. Troutman, Jason S. Seidman, Zhengyu Ouyang, Nathanael J. Spann, Yohei Abe, Kaori M. Ego, Cassi M. Bruni, Zihou Deng, Johannes C.m. Schlachetzki, Alexi Nott,

Hunter Bennett, Jonathan Chang, Baochau T. Vu, Martina P. Pasillas, Verena M. Link, Lorane Texari, Sven Heinz, Bonne M. Thompson, Jeffrey G. Mcdonald, Frederic Geissmann, and Christopher K. Glass. "Liver-Derived Signals Sequentially Reprogram Myeloid Enhancers to Initiate and Maintain Kupffer Cell Identity." Immunity 51.4 (2019): n. pag. Print.

5. Murray, J.s., T. Schountz, S.r. Ford, M.d. Tawde, S. D. S. Jois, T.j. Siahaan, and J.c. Brown. "Modeling Alternative Binding Registers of a Minimal Immunogenic Peptide on Two Class II Major Histocompatibility Complex (MHC II) Molecules Predicts Polarized T-cell Receptor (TCR) Contact Positions." Journal of Peptide Research 59.3 (2002): 115-22. Print.

6. Kovats, Susan, Catherine E. Grubin, Susan Eastman, Paul Deroos, Ashok Dongre, Luc Van Kaer, and Alexander Y. Rudensky. "Invariant Chain–independent Function of H-2M in the Formation of Endogenous Peptide–Major Histocompatibility Complex Class II Complexes In Vivo." Journal of Experimental Medicine 187.2 (1998): 245-51. Print.

7. Perraudeau, Mohini, Philip R. Taylor, Hans J. Stauss, Ragnar Lindstedt, Anne E. Bygrave, Darryl J. C. Pappin, Stephan Ellmerich, Angela Whitten, Dinah Rahman, Benito Canas, Mark J. Walport, Marina Botto, and Daniel M. Altmann. "Altered Major Histocompatibility Complex Class II Peptide Loading in H2-O-deficient Mice." European Journal of Immunology 30.10 (2000): 2871-880. Print.

8. Alfonso, Christopher, Jung-Ok Han, G. Stuart Williams, and Lars Karlsson. "The Impact of H2-DM on Humoral Immune Responses." *The Journal of Immunology* 167.11 (2001): 6348-355. Print.

9. Lobry, Tatiana, Roy Miller, Nathalie Nevo, Celine J. Rocca, Jinzhong Zhang, Sergio D. Catz, Fiona Moore, Lucie Thomas, Daniel Pouly, Anne Bailleux, Ida Chiara Guerrera, Marie-Claire Gubler, Wai W. Cheung, Robert H. Mak, Tristan Montier, Corinne Antignac, and Stephanie Cherqui. "Interaction between Galectin-3 and Cystinosin Uncovers a Pathogenic Role of Inflammation In kidney Involvement of Cystinosis." Kidney International 96.2 (2019): 350-62. Print.

10. Inuzuka, Madoka, Minako Hayakawa, and Tatsuya Ingi. "Serinc, an Activity-regulated Protein Family, Incorporates Serine into Membrane Lipid Synthesis." *Journal of Biological Chemistry* 280.42 (2005): 35776-5783. Print.

11. Usami, Yoshiko, Yuanfei Wu, and Heinrich G. Göttlinger. "SERINC3 and SERINC5 Restrict HIV-1 Infectivity and Are Counteracted by Nef." *Nature* 526.7572 (2015): 218-23. Print.

12. Markart, Philipp, Nicole Faust, Thomas Graf, Cheng-Lun Na, Timothy E. Weaver, and Henry T. Akinbi. "Comparison of the Microbicidal and Muramidase Activities of Mouse Lysozyme M and P." *Biochemical Journal* 380.2 (2004): 385-92. Print.

3.3: Molecular characterization of TNTs: the role of pleckstrin

3.3.1: Introduction

To complement our cellular investigations into the nature of HSPC-derived immune cells in TNT-based intercellular trafficking of cystinosin, we sought to identify and characterize novel molecular protagonists involved in the process. The molecular machinery employed to generate TNTs remains poorly understood, but at present research has elucidated several key members of a multiprotein complex which acts in an ATP-dependent process to effect changes in the actin cytoskeleton leading to plasma membrane protrusion and TNT generation (1,2). The best characterized component was renamed M-Sec (from Tnfaip2) when it was discovered through RNAi to be essential for TNT formation and proper calcium flux (3). M-Sec was shown to induce cytoskeletal remodeling through association with RalA, a member of the Rho family of GTPases. Two other important family members are Cdc42 and Rac1, which also seem to mediate actin polymerization through several downstream pathways (4). Cdc42 has been reported to promote filopodial formation while decreasing TNTs, demonstrating how increased understanding of molecular components can facilitate differentiation between TNTs and other cellular protrusions (5).

Taking advantage of our well-established *in vitro* and *in vivo* models, we aim to better understand molecular basis of TNT-mediated tissue repair following HSPC transplantation. Using differential DNA array technology, we identified several genes which were commonly upregulated across multiple tissues of HSPC recipients in cells which appeared to undergo cross-correction and intercellular trafficking. Pleckstrin (Plek), a protein initially discovered in platelets but widely expressed across the hematopoietic lineage, was one likely candidate discovered which contains two pleckstrin homology (PH) domains thought to mediate interactions between proteins and

specific residues of the plasma membrane (6). Plek has been seen to induce plasma membrane ruffling, as well as formation of membrane projections (7), which are likely mediated through reorganization of the actin cytoskeleton (8). Based on these data, we therefore believe Plek to be an ideal candidate for involvement in TNT formation. We sought to validate the role of pleckstrin in TNT formation and uncover any detailed molecular interactions involved.

3.3.2: Findings

DNA array profiling of cells active in intercellular transport reveals upregulation of pleckstrin and other genes. Using DsRed Ctns$^{-/-}$ mice transplanted with GFP-HSPC (n=3), we performed gene expression profiling analysis comparing the host cells (DsRed^{+}GFP^{-}), the bone marrow-derived cells (DsRed^{-}GFP^{+}) and the double color cells (DsRed^{+}GFP^{+}) from kidney, liver, and muscle (Figure 3.10 A). We hypothesized that the DsRed^{+}GFP^{+} cells represent the HSC-derived macrophages after bi-directional transfer of lysosomes or phagocytosis, so the "active" macrophages. Eight genes were commonly up-regulated in the DsRed+GFP+ cells from all three tissues (Figure 3.10 B). As pleckstrin displayed the strongest differences between cell type and had known roles at the membrane (7,8), it was selected for further study. We also note that several of the genes (H2-Ab1, H2-Aa and Lyz2) were also detected as upregulated in cystinotic cells via RNAseq (see Chapter 3.2).

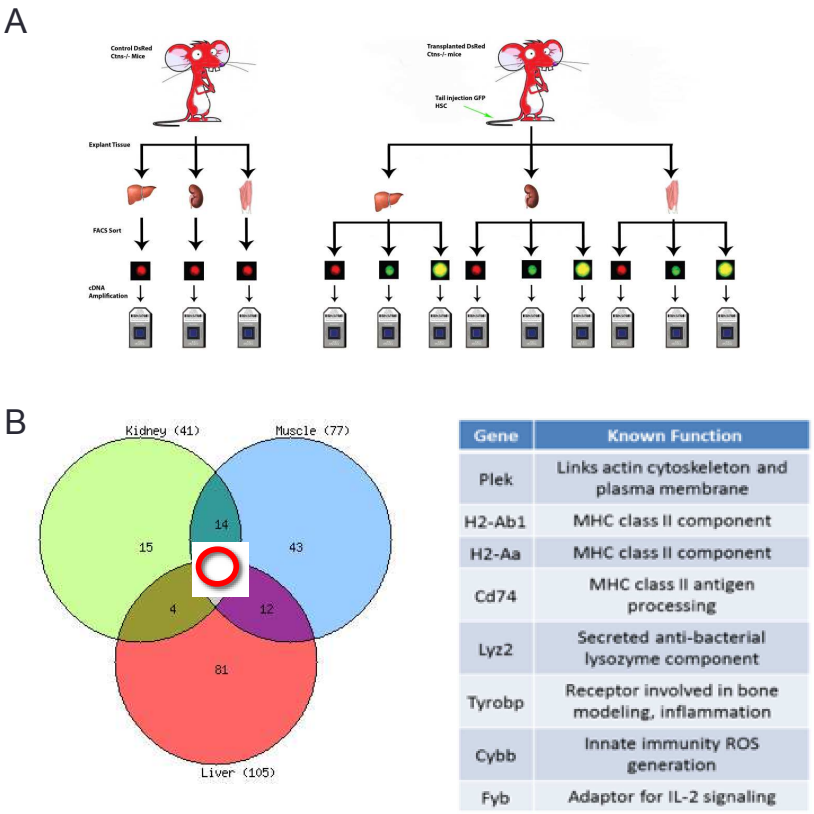

Gene	Known Function
Plek	Links actin cytoskeleton and plasma membrane
H2-Ab1	MHC class II component
H2-Aa	MHC class II component
Cd74	MHC class II antigen processing
Lyz2	Secreted anti-bacterial lysozyme component
Tyrobp	Receptor involved in bone modeling, inflammation
Cybb	Innate immunity ROS generation
Fyb	Adaptor for IL-2 signaling

Figure 3.10: Pleckstrin is potentially involved in intercellular trafficking between HSPC-derived cells and host tissue. A) eGFP HSPCs were transplanted into DsRed cystinotic mice and different colored populations were isolated by FACS sorting from the kidney, liver and spleen. B) DNA microarray analysis identified 8 genes commonly upregulated in yellow cells, which have undergone trafficking to aquire either the DsRed and/or the GFP fluorophore.

Confirmation of the role of Plek in TNT formation. Three separate shRNAs against pleckstrin as well scrambled controls were purchased and assembled into lentiviruses prior to transduction into the mouse peritoneal macrophage IC21 cell line. Pleckstrin expression at both the mRNA and protein levels were reduced, as assessed by qPCR and semi-quantitative immunoblotting, respectively (Figure 3.11 A-B). We then co-cultured these macrophages with DsRed Ctns$^{-/-}$ fibroblasts and analyzed these co-cultures by fluorescent microscopy using our TNT quantification algorithm (see Chapter 3.1). We determined that significantly fewer protrusions were extended in all three knockdown lines relative to scramble or untransduced controls (Figure 3.11 C). Taking a closer look at the protrusions themselves, we observed that macrophage-derived TNTs showed an abnormal phenotype consisting of thicker and branched membrane protrusions

instead of the long, thin and straight TNTs observed in untransduced or scramble-transduced macrophages (Figure 3.11 D). Based on this apparent disorganization of the actin cytoskeleton following knockdown, we initially suspected that Plek might interact with the actin cytoskeleton but high-resolution confocal imaging indicated that Plek may co-localize with tubulin (Figure 3.11 E).

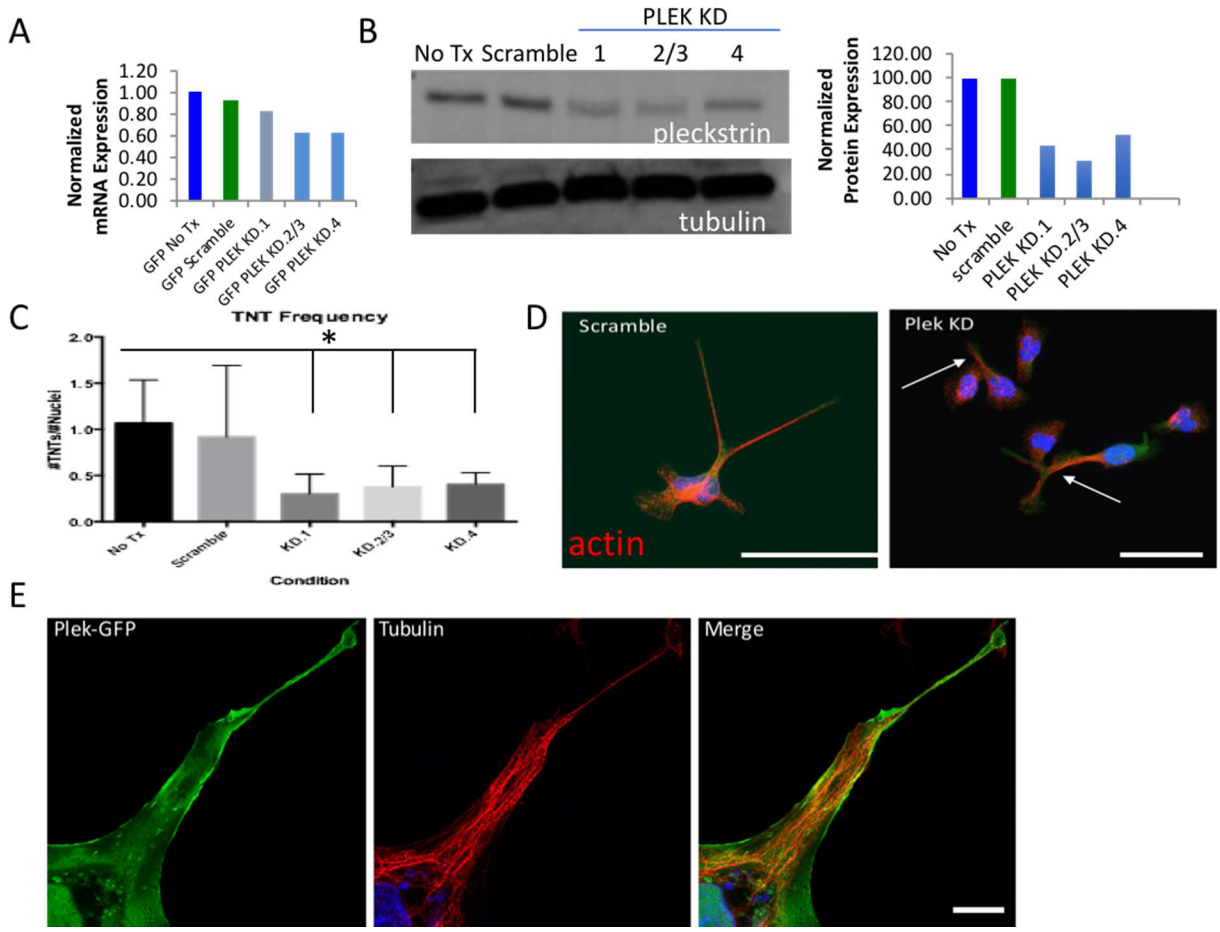

Figure 3.11: Pleckstrin appears to be required for optimal TNT formation from IC-21 macrophages. A-B) IC-21 GFP macrophages were transduced with a lentiviral vector containing either non-targeted shRNA (scramble) or shRNA against Plek (PLEK KD.1, 2/3, 4). Significant reduction of Plek expression was observed both at the RNA (A) and protein levels (B). C) Transduced IC-21 macrophages have fewer TNT-like protrusions relative to scramble or untransduced controls. Blinded automated quantifiaciton performed using a simplified version of protrusion-quantification algorithm described in Chapter 3.1. D) IC-21 macrophages transduced with scramble RNA have normal TNT-like protrusion frequency and morphology, while knockdown cells appear to have protrusions which are less frequent and more disordered (arrows). Actin stain shown in red. Scale bars 100 μm. E) High-resolution confocal micrograph depicting near-colocalization between Pleckstrin-GFP (green) and anti-tubulin (red), specifically within the protrusion. Scale bar 10 μm.

Potential tubulin cytoskeletal interaction with pleckstrin. We then investigated the function of Plek by determining its subcellular localization and protein binding partners. To uncover binding partners, we transduced either Plek-eGFP or eGFP alone as a control into 293T cells and immunoprecipitated (IP) with an anti-eGFP antibody. We surprisingly found that Plek actually appears to co-IP with tubulin (Figure 3.12 A). We did not observe a similar result when probing with an anti-actin antibody (data not shown). In order to determine which domains of Plek are responsible for this interaction, we subcloned smaller fragments of Plek to a c-terminal eGFP tag; we designed two constructs, one lacking the N-terminal PH domain consisting of amino acids 103-350 (Plek No-N) and one without the c-terminal PH domain, amino acids 1-245 (Plek No-C). We verified the size of the expression of these new constructs (Figure 3.12 B) and then used these lysates to assess which fragment, if any, is involved in the pleckstrin-tubulin interaction. We extended our previous findings using both an anti-eGFP (Figure 3.12 C) and anti-tubulin pulldown (Figure 3.12 D) followed by detection by anti-tubulin and anti-eGFP, respectively. Our data confirmed the interaction between Plek and tubulin and suggests that the C-terminal PH-domain is more important for the interaction than the N-terminal. Altogether, these data suggest that Plek could assist in the organization of the microtubule core of TNTs. While all TNTs contain actin, only a subset of "thicker" nanotubes have been shown to also be composed of tubulin as well (9-11). Importantly, macrophages have been reported to generate this specific subset of thicker nanotubes.

We then explored which other proteins known to be involved in TNT formation may interact with Plek. We fused the potential candidates RalA and Rac1 to DsRed and these constructs (as well as the DsRed molecule alone as a control) were then transfected into 293T cells stably expressing Plek-eGFP or eGFP alone. Two days post-transfection, DsRed expression was verified

by fluorescent microscopy and cells were lysed and immunoprecipitated using our anti-eGFP antibody (Figure 3.12 E). As expected, we observed no signal in the DsRed alone conditions in the IP fraction (left two lanes). In the RalA-DsRed lanes (middle two lanes), large bands appeared in both the eGFP and Plek-eGFP conditions, likely representing background or non-specific interactions. With Rac1-DsRed, a unique band was detected in the Plek-eGFP condition (far right lane, arrow) in the IP fraction which was not present in the unbound fraction (data not shown). From this experiment, we therefore conclude that Plek interacts with Rac1 but not RalA. Rac1 is a member of the Rho-family GTPase and has recently been reported to be involved in TNT formation (4) along with a variety of other functions including vesicular transport (12) as well as invadapodia formation in cancer (13). Furthermore, Rac1 has been shown to interact with both the tubulin and actin cytoskeletons (14).

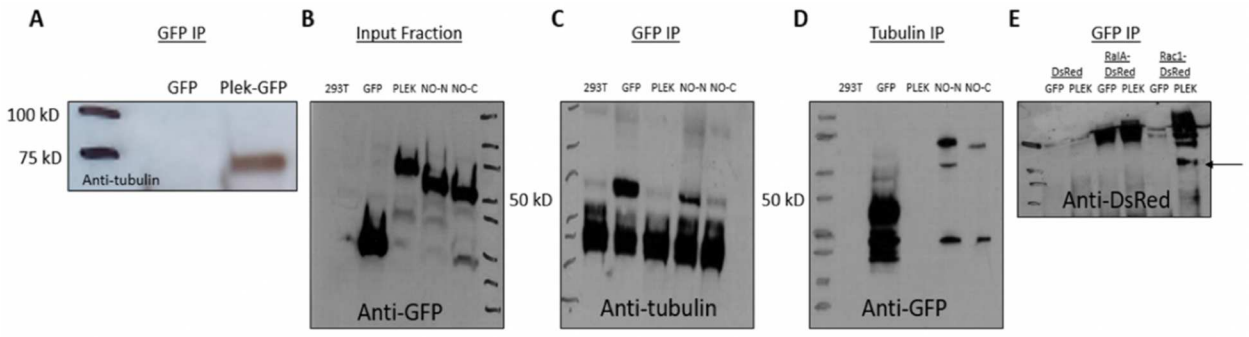

Figure 3.12: Pleckstrin co-immunoprecipatates with tubulin and Rac1. A) 293T cells stably transuced with pleckstrin-GFP results in signala following GFP IP but not GFP alone. B) Fragments of pleckstrin corresponding to amino acids 103-350 without the N-terminal PH domain (No-N) and amino acids 1-245 without the C-terminal domain (No-C) are stably expressed in 293T cells and detected with anti-GFP. C-D) Reciprocal IP demonstrating that increased signal is observed with pleckstrin No-N over No-C when pulled down with either GFP (C) or tubulin (D). E) 293T cells stably expressing GFP or pleckstrin-GFP were transfected with DsRed, RalA-DsRed and Rac1-DsRed and then immunoprecipitated with anti-GFP. Detection was preformed with anti-DsRed. Arrow indicates Rac1-DsRed signal specific to Pleckstrin-GFP input.

3.3.3: References

1. Abounit, S. and C. Zurzolo, *Wiring through tunneling nanotubes--from electrical signals to organelle transfer.* J Cell Sci, 2012. **125**(Pt 5): p. 1089-98.

2. Kimura, S., K. Hase, and H. Ohno, The molecular basis of induction and formation of tunneling nanotubes. Cell Tissue Res, 2013. 352(1): p. 67-76.

3. Hase, K., Kimura, S., Takatsu, H., Ohmae, M., Kawano, S., Kitamura, H., … Ohno, H. (2009). M-Sec promotes membrane nanotube formation by interacting with Ral and the exocyst complex. *Nature Cell Biology*, *11*(12), 1427–1432. doi: 10.1038/ncb1990

4. Hanna, S. J., Mccoy-Simandle, K., Miskolci, V., Guo, P., Cammer, M., Hodgson, L., & Cox, D. (2017). The Role of Rho-GTPases and actin polymerization during Macrophage Tunneling Nanotube Biogenesis. *Scientific Reports*, *7*(1). doi: 10.1038/s41598-017-08950-7

5. Delage, E., Cervantes, D. C., Pénard, E., Schmitt, C., Syan, S., Disanza, A., … Zurzolo, C. (2016). Differential identity of Filopodia and Tunneling Nanotubes revealed by the opposite functions of actin regulatory complexes. *Scientific Reports*, *6*(1). doi: 10.1038/srep39632.

6. Abrams, C. S., Zhao, W., Belmonte, E., & Brass, L. F. (1995). Protein Kinase C Regulates Pleckstrin by Phosphorylation of Sites Adjacent to the N-terminal Pleckstrin Homology Domain. *Journal of Biological Chemistry*, *270*(40), 23317–23321. doi: 10.1074/jbc.270.40.23317

7. Ma, A.D., L.F. Brass, and C.S. Abrams, Pleckstrin associates with plasma membranes and induces the formation of membrane projections: requirements for phosphorylation and the NH2-terminal PH domain. J Cell Biol, 1997. 136(5): p. 1071-9.

8.Ma, A.D. and C.S. Abrams, Pleckstrin induces cytoskeletal reorganization via a Rac-dependent pathway. J Biol Chem, 1999. 274(40): p. 28730-5.

9. Abrams, C. S., Zhao, W., Belmonte, E., & Brass, L. F. (1995). Protein Kinase C Regulates Pleckstrin by Phosphorylation of Sites Adjacent to the N-terminal Pleckstrin Homology Domain. *Journal of Biological Chemistry*, *270*(40), 23317–23321. doi: 10.1074/jbc.270.40.23317

10. Marzo, L., K. Gousset, and C. Zurzolo, Multifaceted roles of tunneling nanotubes in intercellular communication. Front Physiol, 2012. 3: p. 72.

11. Sowinski, S., Alakoskela, J.-M., Jolly, C., & Davis, D. M. (2011). Optimized methods for imaging membrane nanotubes between T cells and trafficking of HIV-1. *Methods*, *53*(1), 27–33. doi: 10.1016/j.ymeth.2010.04.002

12.Ridley, A.J., Rho GTPases and actin dynamics in membrane protrusions and vesicle trafficking. Trends Cell Biol, 2006. 16(10): p. 522-9.

13. Revach, O.-Y., Winograd-Katz, S. E., Samuels, Y., & Geiger, B. (2016). The involvement of mutant Rac1 in the formation of invadopodia in cultured melanoma cells. *Experimental Cell Research*, *343*(1), 82–88. doi: 10.1016/j.yexcr.2016.02.003

14. Guo, F., Debidda, M., Yang, L., Williams, D. A., & Zheng, Y. (2006). Genetic Deletion of Rac1 GTPase Reveals Its Critical Role in Actin Stress Fiber Formation and Focal Adhesion Complex Assembly. *Journal of Biological Chemistry*, *281*(27), 18652–18659. doi: 10.1074/jbc.m603508200

3.4: Search for TNT signals: alternations in cystinotic metabolomics

3.4.1: Introduction

Our observations that TNT formation and intercellular trafficking were upregulated in *in vitro* co-culture with diseased cystinotic (or FRDA) fibroblasts (see figure 3.3 and 3.4) led to the obvious question of what specific signaling might be causing this phenomenon. Many types of stimuli ranging from pathogens to genotoxic agents to varied cellular stressors have been shown to upregulate TNT formation, but these studies invariably investigated protrusion formation from the affected cell itself (1). In our case, TNTs were being formed in a healthy macrophage in response to some stimulus from co-cultured diseased fibroblasts – a situation without extensive reports in the literature beyond our prior word (2).

In collaboration with Dr. Ilya Gertsman, we sought to broadly examine the nature of any differences in cellular metabolites that may lead to an induction of TNT formation and intercellular trafficking. We employed untargeted metabolomics both intracellularly and in the culture media following co-culture between WT macrophages and cystinotic or WT fibroblasts. After discovering differences in purinergic biosynthetic compounds, we utilized our TNT-like protrusion detection algorithm (see Chapter 3.1) to assess if addition of any particular metabolite was effective at altering baseline levels of protrusion formation. However, we did not discover significant effects of any individual compound, and when we repeated the co-culture metabolomics experiments with fresh media we failed to recapitulate our initial results.

To clarify these broad metabolomic findings, we sought to investigate any fundamental differences between cystinotic and WT fibroblasts using a more targeted approach. Such findings may eventually lead to the discovery of novel biomarkers for cystinosis, as there are well-known limitations in the current standard-of-care using intracellular cystine, see Chapter 5 for further

details (3). Furthermore, the underlying pathology of cystinosis is not entirely caused by intralysosomal cystine accumulation as decreasing cystine load still does not completely alleviate many cellular changes associated with the disease. For example, abnormal mitochondrial function and increased mitophagy has been observed in cystinosis, which may be caused by several underlying metabolic abnormalities (4). One option is an increase in ATP consumption (5), while other proposed suggestion is an aberrant gamma glutamyl cycle to be the cause of decreased ATP, as well as lower levels of glutathione in cystinotic cells (6). By further characterizing the nature of metabolic differences between healthy and cystinotic cells, we may be able to improve the understanding of cystinosis pathology.

We hypothesized that noted defects in autophagy during cystinosis (4-6) may be reflected in changes in primary energy pathways such as glycolysis, TCA, amino acids, nucleotides, purines/pyrimidines, or acylcarnitines and so focused on these targets. By comparing fibroblasts in fresh media vs. serum starvation, we were able to detect more dramatic changes in energy metabolites, purine catabolites, glycolytic intermediates, and redox coenzymes in cystinotic fibroblasts. As the ultimate goal of this research would be the discovery of novel human biomarkers, we finally moved from fibroblasts to mouse plasma to determine if metabolic alterations persisted in a more complex *in vivo* environment.

3.4.2: Findings

Metabolomic analysis of macrophage co-cultures with WT v. cystinotic fibroblasts. We have independently observed an upregulation of TNT-like protrusion formation and intercellular trafficking from macrophages in response to cystinotic cells and tissues both *in vitro* (Figure 3.3) as well as *in vivo* as indicated by increased recruitment of HSPC-derived cells to cystinotic tissues (2,7). While we know that this phenomenon is induced by some media-soluble

factor secreted by cystinotic fibroblasts due to the ability of cystinotic fibroblast-conditioned media to elicit an increase in macrophage TNT-like protrusion formation, the precise nature and molecular agents of this signaling remain unknown.

In an attempt to unravel these mechanisms, we employed an untargeted metabolomic approach using high resolution mass spectrometry on both the media and intracellular fractions of WT macrophages in co-culture with cystinotic or WT fibroblasts. Thousands of ions were collected and compared before reducing the dataset to isolate the most important metabolites that distinguish WT and cystinotic co-cultures (Figure 3.13 A). Significant changes in several purinergic signaling compounds were seen between the media of the different co-cultures. (Figure 3.13 B). Specifically, we detected significantly higher adenosine was observed in the media of cystinotic co-cultures. This indicates a potential alteration in purinergic signaling factors and catabolic metabolism, a possibility supported by the observation of very large-scale elevations in purine metabolites such as xanthosine, hypoxanthine, and xanthine. Critically, we detected the opposite change of the final product of the pathway uric acid, implicating an inhibition, blockage or down-regulation of the enzyme xanthine oxidase (XO). XO converts oxygen and water into a byproduct of hydrogen peroxide, and is regulated by disulfide bond formation, which may be altered in cystinosis (8-10). Similar changes, in some cases with even more extreme differences in expression, were detected between WT and cystinotic fibroblasts alone (data not shown). Based on these data, we moved to determine if these purinergic compounds had any direct effect on TNT-like protrusion formation from macrophages.

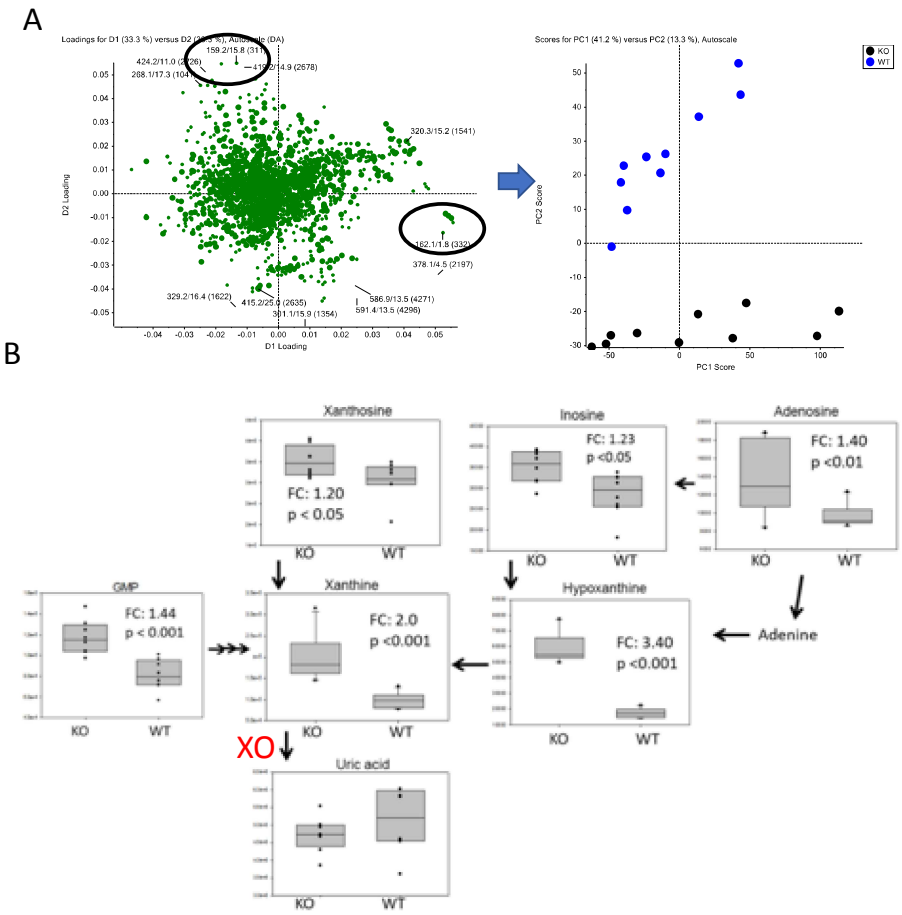

Figure 3.13: Untargeted metabolomics reveals perturbations in purinergic catabolic biosynthetic compounds in the media of cystinotic co-cultures. A) Co-cultures of WT IC-21 macrophages with WT (green dots) or cystinotic (blue) fibroblasts were grown for 3 days and then harvested. High resolution mass spectrometry detects thousands of ions which were reduced by PCA analysis to determine differentially expressed metabolites. B) Dysregulation of adenosine and purinergic compounds was observed in the media of cystinotic co-cultures. Most compounds such as xanthine, hypoxanthine and inosine were lower in WT co-cultures compared to cystinotic, but the final product uric acid was switched. This potentially indicates dysfunction of xanthine oxidase (XO), the enzymatic regulator of the xanthine to uric acid step.

Effect of purinergic compounds on macrophage TNT-like protrusion formation. Based on our untargeted discovery of perturbations in the purinergic biosynthetic pathway, we attempted to determine if any of the differential compounds could induce or suppress TNT-like protrusion formation from IC-21 macrophages. We first determined that there were no differences in the protein expression of xanthine oxidase via western blot between cystinotic and WT fibroblasts (data not shown), indicating that the metabolic changes may be caused by alterations

in activity rather than expression. We then acquired purified xanthine and hypoxanthine in order to test if addition of these compounds would affect protrusion formation.

IC-21 macrophages were seeded in equal numbers in a variety of media; either normal unconditioned RPMI media, media conditioned by two days of growth of cystinotic or WT fibroblasts, or unconditioned media with the addition of purinergic compounds. Using an early simplified variant of our TNT-like protrusion quantification algorithm (see Chapter 3.1), we determined that while significantly more protrusions were formed in the cystinotic-conditioned media, there were no significant changes following addition of xanthine or hypoxanthine at either high or low concentrations (Figure 3.14 A). We also did not detect any significant changes in overall cell number of these compounds compared to unconditioned or WT-conditioned media, although cystinotic-conditioned media did trend towards increased cells in addition to increased protrusions (Figure 3.14 B). These data indicated that the alterations of the purinergic biosynthetic compounds detected via untargeted mass spectrometry are not sufficient to induce TNT-like protrusion formation.

Given our failure to induce TNT-like protrusion formation despite noted metabolic changes in the media of co-cultures, we then re-examined our cell culture model system. Based on our approach described in Chapter 3.1, co-cultures were grown for 3 days in the same media after initial seeding. As metabolites are very sensitive to nutrient depletion in the media, we tried to repeat both the co-culture and fibroblast alone experiments with fresh media and were not able to reproduce the findings. Therefore, the significant differences seen between WT and cystinotic co-cultures may be attributed to differential response of the cystinotic cells to decreasing media nutrients.

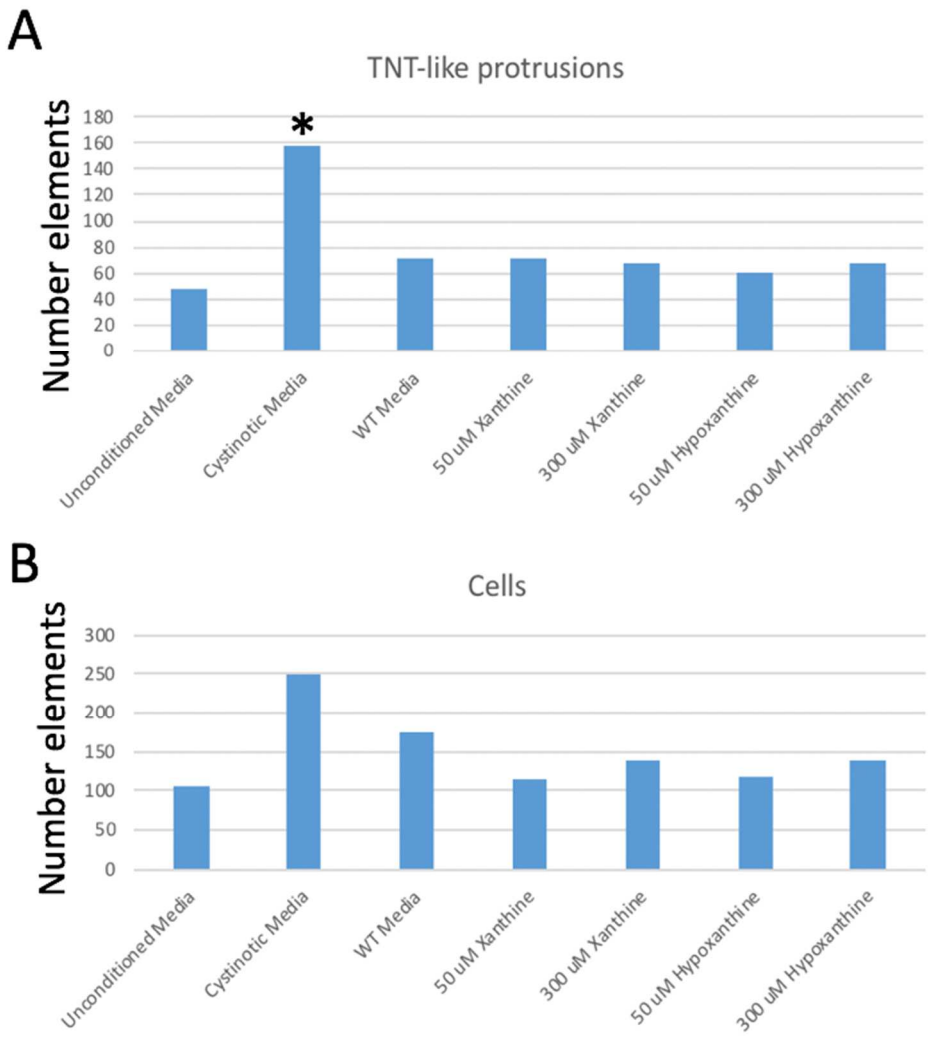

Figure 3.14: Treatment of macrophages with purinergic compounds does not affect TNT-like protrusion formation. A) WT IC-21 macrophages were grown for 3 days in a variety of conditions ranging from normal unconditioned media to media conditioned by the growth of cystinotic or WT fibroblasts to treatment of normal media with the purinergic compounds xanthine or hypoxanthine. No significant changes were detected in the number of TNT-like protrusions in any condition but growth in media conditioned by cystinotic fibroblasts. Protrusion quantification was preformed blind as described in Chapter 3.1. B) No significant changes were detected in total cell count of IC-21 macrophages under any stimulation.

Metabolomic differences between WT and cystinotic fibroblasts and mouse serum. We then sought to determine if any metabolomic changes in the WT or cystinotic fibroblasts could be reproducibly detected when cells were isolated from fresh media (changes within 16 hours of cell harvest). We set up several growth conditions including fresh media, acute starvation (1 hr of culture in HBSS) and starvation followed by refeeding (1 hr in HBSS, 30 mins in fresh media).

Following metabolite harvest and mass spectrometry, we noticed marked changes in the levels of energy nucleotides such as ADP and AMP (but not ATP) under the conditions of serum starvation between WT and cystinotic fibroblasts (Figure 3.15 A-B). Other purine catabolites such as hypoxanthine, uridine and cytidine also displayed a significantly greater upregulation under serum starvation in cystinotic fibroblasts (Figure 3.15 C). Taken together, we observe a dramatic increase of roughly 2.5 fold of the change in purine metabolites upon starvation. These data are likely a reflection of abnormal autophagy in cystinosis (4-6).

However, when we attempted to extend these findings to mouse serum by testing both fasted and fed WT and cystinotic mice, changes between genotypes were far more subtle (Figure 3.15 D). While cytidine appeared more elevated in cystinotic mice compared to WT, differences are reduced compared to cell culture and other metabolites showed no difference between genotypes. This may indicate that any metabolic effects may not be happening uniformly enough in all cell types to cause a significant overall change in plasma despite being significantly altered in fibroblast culture.

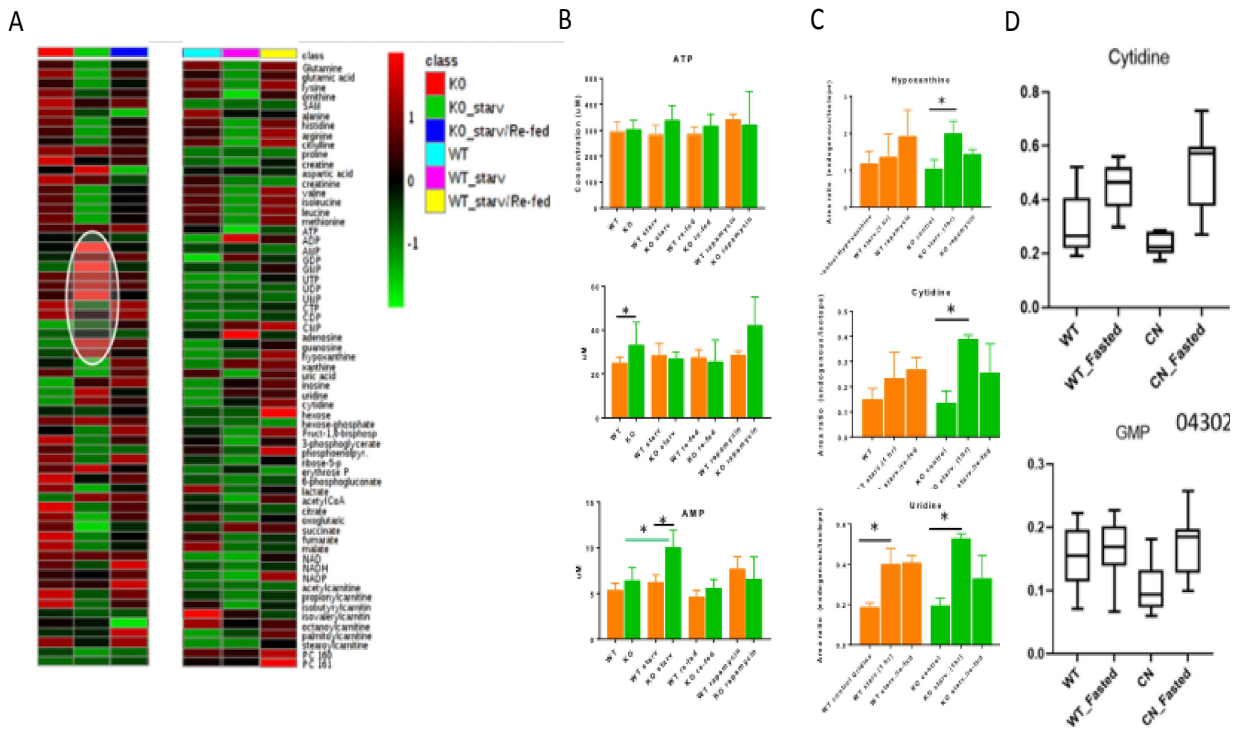

Figure 3.15: Metabolomic alternations are detected between WT and cystinotic fibroblasts but not mouse serum following nutrient depletion or fasting. A) Heatmap depicting metabolite abundance from fibroblasts under a variety of conditions. Left three columns depict cystinotic metabolites from fresh media (far left), starvation (middle) and refeeding (right). Right columns are WT fibroblasts under same conditions. Circled region highlights increased changes of energy carriers following starvation of KO cells. B) Selected comparisons of phosphorylated adenosine molecules from WT or cystinotic fibroblasts. While levels of ATP are unchanged, ADP and AMP are significantly altered in either/both fresh media as well as starvation conditions. C) Enhanced increase in purine catabolites are also observed following starvation of cystinotic fibroblasts. D) Serum was collected from fed or overnight fasted WT and cystinotic mice via retro-orbital bleed. Changes in metabolites were reduced compared to fibroblasts, with only cytidine showing any potentially significant differences between genotypes.

3.4.3: Acknowledgments

Chapter 3.4 is based on unpublished work with the coauthors Swati Naphade, Ilya Gertsman and Stephanie Cherqui. The dissertation author was the co-primary investigator of this work.

3.4.4: References

1. Kimura, S., K. Hase, and H. Ohno, The molecular basis of induction and formation of tunneling nanotubes. Cell Tissue Res, 2013. 352(1): p. 67-76.

2. Naphade, Swati, Jay Sharma, Héloïse P. Gaide Chevronnay, Michael A. Shook, Brian A. Yeagy, Celine J. Rocca, Sarah N. Ur, Athena J. Lau, Pierre J. Courtoy, and Stephanie Cherqui. "Brief Reports: Lysosomal Cross-Correction by Hematopoietic Stem Cell-Derived Macrophages Via Tunneling Nanotubes." Stem Cells 33.1 (2014): 301-09. Print.

3. Belldina, E. B., Huang, M. Y., Schneider, J. A., Brundage, R. C. & Tracy, T. S. Steady-state pharmacokinetics and pharmacodynamics of cysteamine bitartrate in paediatric nephropathic cystinosis patients. Br J Clin Pharmacol 56, 520-525, doi:10.1046/j.1365-2125.2003.01927.x (2003).

4. Sansanwal, Poonam, and Minnie M. Sarwal. "Abnormal Mitochondrial Autophagy in Nephropathic Cystinosis." Autophagy 6.7 (2010): 971-73. Print.

5. Levtchenko, Elena N., Martijn J G Wilmer, Antoon J M Janssen, Jan B. Koenderink, Henk-Jan Visch, Peter H G M Willems, Adriana De Graaf-Hess, Henk J. Blom, Lambertus P Van Den Heuvel, and Leo A. Monnens. "Decreased Intracellular ATP Content and Intact Mitochondrial Energy Generating Capacity in Human Cystinotic Fibroblasts." Pediatric Research 59.2 (2006): 287-92. Print.

6. Kumar, Akhilesh, and Anand Kumar Bachhawat. "A Futile Cycle, Formed between Two ATP-dependant γ-glutamyl Cycle Enzymes, γ-glutamyl Cysteine Synthetase and 5-oxoprolinase: The Cause of Cellular ATP Depletion in Nephrotic Cystinosis?" Journal of Biosciences 35.1 (2010): 21-25. Print.

7. Lobry, Tatiana, Roy Miller, Nathalie Nevo, Celine J. Rocca, Jinzhong Zhang, Sergio D. Catz, Fiona Moore, Lucie Thomas, Daniel Pouly, Anne Bailleux, Ida Chiara Guerrera, Marie-Claire Gubler, Wai W. Cheung, Robert H. Mak, Tristan Montier, Corinne Antignac, and Stephanie Cherqui. "Interaction between Galectin-3 and Cystinosin Uncovers a Pathogenic Role of Inflammation In kidney Involvement of Cystinosis." Kidney International 96.2 (2019): 350-62. Print.

8. Nishino, Tomoko, Ken Okamoto, Bryan T. Eger, Emil F. Pai, and Takeshi Nishino. "Mammalian Xanthine Oxidoreductase - Mechanism of Transition from Xanthine Dehydrogenase to Xanthine Oxidase." FEBS Journal 275.13 (2008): 3278-289. Print.

9. Ryan, Michael J., Janna R. Jackson, Yanlei Hao, Stephen S. Leonard, and Stephen E. Alway. "Inhibition of Xanthine Oxidase Reduces Oxidative Stress and Improves Skeletal Muscle Function in Response to Electrically Stimulated Isometric Contractions in Aged Mice." Free Radical Biology and Medicine 51.1 (2011): 38-52. Print.

10. Corte, E. D., and F. Stirpe. "The Regulation of Rat Liver Xanthine Oxidase. Involvement of Thiol Groups in the Conversion of the Enzyme Activity from Dehydrogenase (type D) into Oxidase (type O) and Purification of the Enzyme." Biochemical Journal 126.3 (1972): 739-45. Print.

Chapter 4: Impact of *Shpk* in HSPC transplantation

The following Chapter 4, in full, is a reprint of material that is being prepared for publication. Initial submission was delayed by COVID-19 and is expected by October 2020 .

4.1: Introduction

Cystinosis is an autosomal-recessive lysosomal storage disorder caused by mutations in the CTNS gene that affects about one out of every 100,000 live births (1). Over 100 unique mutations ranging from single base substitutions to large indels have been identified as causing for cystinosis by perturbing the localization or function of cystinosin, an ubiquitously expressed lysosomal transmembrane cystine-proton transporter (2-4). Without functional cystinosin, cystine accumulates within the lysosomes and deposits as crystals throughout the body, causing organ failure(5). While renal Fanconi syndrome presents as the first clinical manifestation in the first year of life, patients also experience later end-stage renal failure, photophobia, muscle atrophy, diabetes, hypothyroidism and neurological defects (1, 6). Current specific treatment is the drug cysteamine, which depletes cystine by allowing lysosomal export through alternative channels(7). This therapy, in use since 1976, prolongs life expectancy to adulthood, but ultimately merely delays symptomatic progression and does not address the root genetic pathology(8, 9).

Our group has focused on developing hematopoietic stem cell (HSPC) transplantation therapy for cystinosis(10-13). We transplanted wildtype (WT) or gene-corrected HSPCs into lethally irradiated knockout cystinotic (Ctns-/-) recipients, a model which develop comparable disease complications than the cystinosis patients(2, 14-16). After bone marrow reconstitution, HSPC progeny engrafted into all organs, and cystine was significantly decreased across all tissues(10, 12). We observed morphological preservation of the kidney, cornea, and thyroid for the

lifespan of WT HSPC recipients, indicating that a single HSPC transplantation appears to be an effective therapy preventing cystinosis disease progression in the mouse. Study of the mechanism of action revealed that HSPCs differentiate into macrophages and are able to deliver cystinosin-bearing lysosomes to the diseased cells via tunneling nanotubes (TNTs)(13, 17). Based on these promising data, we have initiated a Phase I/II clinical trial translating this strategy to human cystinosis patients, where patients' HSPCs are genetically modified ex vivo using a lentiviral vector containing functional CTNS prior to being reintroduced into the myleoablated patient (ClinicalTrials.gov Identifier: NCT03897361).

One concern with moving this strategy into humans lies in the nature of the most common disease-causing mutation; a large 57 kilo base pair (kbp) deletion spanning not only the entire CTNS gene, but also the neighboring sedoheptulokinase (SHPK) locus(18). Sedoheptulokinase (SHPK), formerly known as carbohydrate-like kinase (CARKL), is metabolic regulatory enzyme found in the non-oxidative arm of the pentose phosphate pathway (PPP) that supplies carbon substrates for glycolysis(19) . In an ATP-dependent fashion, Shpk generates sedoheptulose-7-phosphate (S7P), both a product and substrate of glucose metabolism(20). Via this contribution to metabolic flux, Shpk is a critical regulator of macrophage polarization and differentiation(20). As roughly 40% of human patients carry the 57-kb deletion in the homozygote state and so do not express SHPK, coupled with the fact that tissue rescue by HSPC transplantation relies upon their differentiation into macrophages (13, 17), we had to investigate any therapeutic impact of SHPK-deficient HSPCs for cystinosis. Understanding SHPK in this context is critical to determine if patients carrying the 57-kb deletion at the homozygote state could be enrolled in the ongoing clinical trial.

In this present study, we seek to address the impact of Shpk in the therapeutic efficacy of HSPC transplantation. We generated and charecterized two novel Shpk-deficient mouse models and observed reduction in mRNA and protein expression, as well as a mild metabolic phenotype consisting of perturbation of PPP metabolites in the liver and urine. Transplantation of Shpk-/- HSPCs into cystinotic mice (Ctns-/-Shpk+/+) retained the ability of rescuing cystinosis as assessed by cystine accumulation, Ctns expression and renal function. Therefore, cystinosis patients lacking SHPK are equally likely to receive therapeutic benefit from autologous transplantation of gene-modified HSPCs and will be enrolled in the clinical trial.

4.2: Results

***Shpk* knockout generation and expression characterization.** To assess if Shpk is required for HSPC transplantation therapy for cystinosis, we first needed to eliminate expression from donor HSPCs. To generate novel knockout mouse lines, two CRISPR-Cas9 guides were independently generated targeting the start codon ($Shpk^{\Delta ATG}$), and the second exon ($Shpk^{\Delta E2}$) (Figure 4.1A). The first model created at UC San Diego resulted in numerous deleted offspring, of which a mouse carrying a 168-bp deletion abolishing the ATG start codon was bred to WT C57 B6/J mice (Figure 4.1B, Supplemental File 3, Supplemental Table 1 for primer sequences). As a second independent model, we acquired a *Shpk* KO strain from UC Davis with guides targeted at the second exon leading to a 675-bp deletion ($Shpk^{\Delta E2}$). Offspring of heterozygote founders for both models were cross-bred and resulted in homozygous mutants following a Mendelian ratio (Supplemental File 3, Supplemental Figure 1A-C). Both mouse colonies were subsequently bred to DsRed-expressing mice to generate fluorescently-labeled *Shpk* knockouts.

Shpk knockout was verified at the mRNA and protein levels, by qPCR and semi-quantitative immunoblots, respectively. At the mRNA level, we observed a dramatic reduction of *Shpk* expression in the $Shpk^{\Delta E2}$ as compared to WT, most pronounced in the kidney and liver (Figure 4.1C). However, $Shpk^{\Delta ATG}$ mRNA was surprisingly comparable to WT, with no significant differences in any tissue. As our qPCR primers spanned exon 3-4, we expected both knockouts to reduce mRNA.

Shpk protein level was tested in kidney, liver, brain, heart, spleen and muscle from WT, $Ctns^{-/-}$, $Shpk^{\Delta E2}$, and $Shpk^{\Delta ATG}$ mice. In WT and $Ctns^{-/-}$ liver samples, we detected a strong size appropriate band corresponding to a protein of ~57-kilodaltons (kD) (Figure 4.1D, full blots

Supplemental File 3, Supplemental Figure 2), and complete absence in both $Shpk^{\Delta E2}$ as well as $Shpk^{\Delta ATG}$ tissues, a highly significant reduction compared to WT ($p<0.001$). A less intense size-appropriate Shpk band was detected in WT and $Ctns^{-/-}$ but not Shpk-deficient kidney samples (Supplemental File 3, Supplemental Figure 2A). In brain, heart, spleen and muscle, Shpk was not detected, strongly suggesting that Shpk is expressed mainly in liver in kidney in mice (Supplemental File 3, Supplemental Figure 2 B-E). The inconsistency of mRNA versus protein expression in $Shpk^{\Delta ATG}$ mice suggests that even if partial mRNA is being expressed by $Shpk^{\Delta ATG}$ mice, no functional protein is translated. This could be due to the presence of an internal methionine driving partial mRNA expression but leading to a frameshift and a non-functional protein, which is probably eventually degraded by nonsense-mediated decay(21).

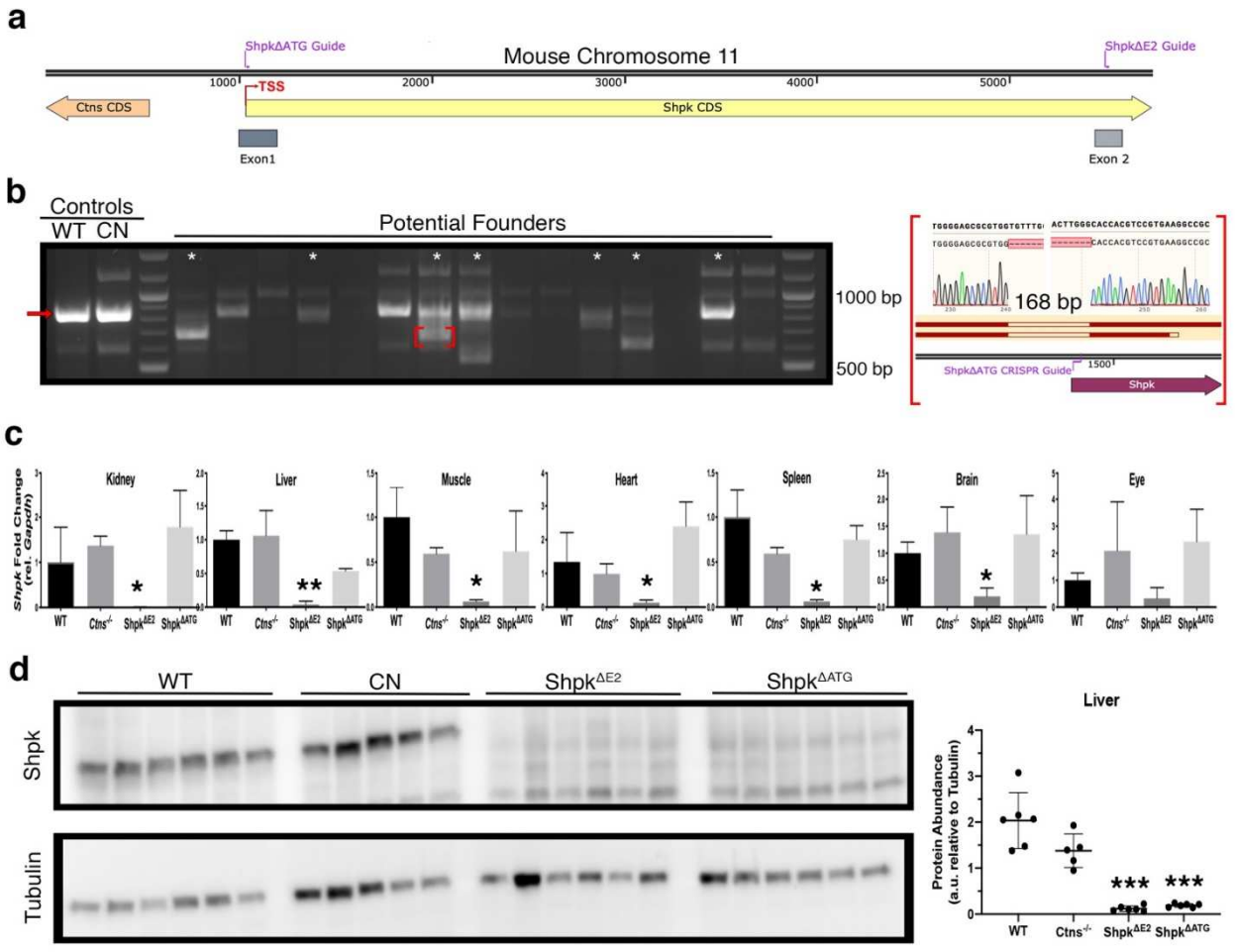

Figure 4.1: Generation and characterization of two novel Shpk knockout mouse models. A) Diagram of the mouse genomic region between *Ctns* and *Shpk.* CRISPR-Cas9 guides depicted at start codon (Shpk$^{\Delta ATG}$) or second exon (Shpk$^{\Delta E2}$). B) PCR gel depicting flanking genotyping primers of normal controls (arrow) or 15 potentially edited Shpk$^{\Delta ATG}$ founders. Expected WT band size is 820 bp. Starred lanes had detectable deletions by Sanger Sequencing. Sequence of bracketed band, representing the selected founder, shown to right. C) Bar graphs depicting relative expression of *Shpk* as measured by qPCR on cDNA derived from various tissues. Delta/delta C_t normalization method employed using *Gapdh* as housekeeping controls. Stars denote significant difference in fold change as compared to WT. D-E) Representative anti-Shpk immunoblots from liver (D) and kidney (E) with anti-tubulin as loading control. Quantitation shown to right based on relative densitometry between size-appropriate Shpk band and tubulin. Stars depict significant difference relative to WT. Full uncropped westerns shown in Supplemental Figure 2. * $P<0.05$, ** $P<0.01$, *** $P<0.001$

Pentose Phosphate Pathway metabolomics are disrupted in Shpk KO liver and urine.

As phosphorylation of sedoheptulose into sedoheptulose-7-phosphate (S7P) is an important step in the PPP catalyzed by Shpk (Figure 4.2A), we sought to assess if any metabolites were

dysregulated in our knockout mouse models. Metabolite abundance was measured by intracellular mass spectrometry on flash-frozen liver samples. We specifically focused on the following PPP metabolites: i) S7P as the direct Shpk product; ii) glyceraldehyde-3-phosphate as an aldose intermediate; iii) erythrose-4-phosphate (E4P), an erythritol precursor found at high urinary concentrations in cystinosis patients; iv) upstream intermediates ribose-4-phosphate (R4P) and xylose-4-phopshate (X4P), which could not be discriminated via our methodology; and v) 6-phosphogluconate (6PG), which could not be discriminated from DHAP. All metabolites but E4P were decreased in both Shpk KO as compared to the WT and $Ctns^{-/-}$ controls (Figure 4.2B)(20, 22). The reduction of S7P is relatively straightforward and expected after eliminating the catalytic enzyme, but changes in upstream R5P and X5P, glyceraldehyde-3-phosphate and 6PG potentially indicate a more complex regulatory role for Shpk.

We also examined the urine of *Shpk*-deficient mice for PPP dysregulation based on suggestive findings from humans lacking *SHPK(23, 24)*. We detected an increase in urinary sedoheptulose and erithryotol in both *Shpk* knockouts as compared to either WT or cystinotic mice (Figure 4.2C). Interestingly, while PPP metabolites are decreased in the liver, they appear upregulated in excreted urine.

While the PPP is perturbated in the Shpk KO mice, we did not detect any change in a wide variety of other molecules including energy carriers (Supplemental File 3, Supplemental Figure 3A), hexose sugars (Supplemental File 3, Supplemental Figure 3B) or NADP cycle intermediates (Supplemental File 3, Supplemental Figure 3C). This is expected considering the supporting role the PPP plays in overall anaerobic metabolism. Furthermore, any other obvious phenotype in the Shpk KO mice was not observed. While some evidence suggested that PPP disruption may result in an ovarian phenotype, we did not observe any abnormal pathologies in *Shpk*-deficient mice(25).

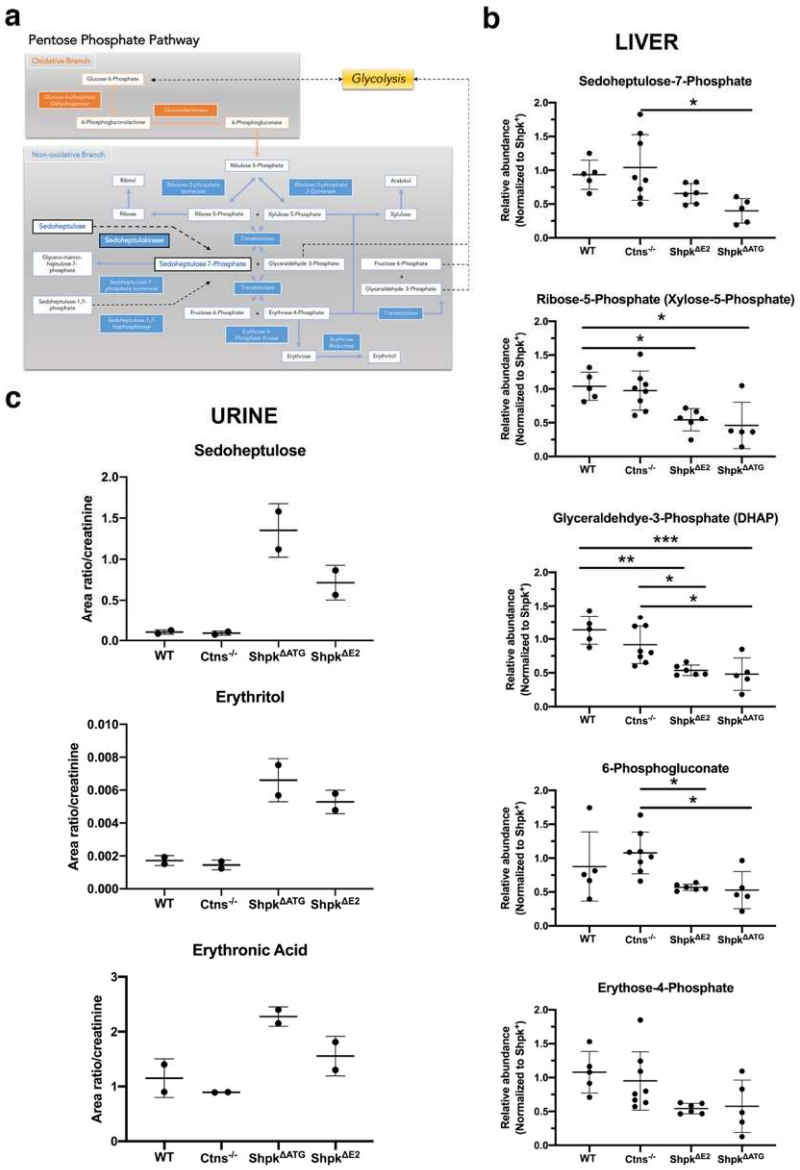

Figure 4.2: Elimination of *Shpk* leads to metabolic perturbations in the PPP. A) Schematic of the pentose phosphate pathway (PPP) illustrating reactions, intermediates and *SHPK* metabolism of implicated metabolites. **(B)** Mass spectrometry quantitation of PPP metabolite relative abundance in WT, *Ctns*$^{-/-}$, *Shpk*$^{\Delta ATG}$, and *Shpk*$^{\Delta E2}$ livers (n=4-6). **(C)** Mass spectrometry quantitation of urinary PPP metabolic content as a consequence of Shpk-deficiency (n=2). . * $P<0.05$, ** $P<0.01$.

Shpk$^{-/-}$ HSPC transplantation reduces cystine load and restores Ctns expression across multiple tissues of cystinotic recipient mice. We next addressed if HSPCs defective in *Shpk* resulted in effective prevention of cystinosis in the Ctns$^{-/-}$ mice. We isolated Sca1^{+} HSPCs

from the marrow of 6-8-week-old Shpk KO and WT and $Ctns^{-/-}$ mice served as positive and negative controls, respectively(10-12). HSPCs were transplanted into 2-month-old lethally irradiated $Ctns^{-/-}$ mice. Mice were sacrificed for analysis at 6 months post-transplantation.

Across a variety of tissues including kidney, liver, muscle and spleen, transplantation of *Shpk*$^{-/-}$ HSPCs significantly lowered cystine accumulation in $Ctns^{-/-}$ mice as compared to $Ctns^{-/-}$ controls, i.e. $Ctns^{-/-}$ HSPC and untreated $Ctns^{-/-}$ recipient mice (Figure 4.3A). We did not observe a significant difference in cystine levels between mice transplanted with WT or Shpk KO HSPCs, nor were significant differences detected between of $Shpk^{\Delta ATG}$ and $Shpk^{\Delta E2}$ HSPC recipients.

Ctns expression was evaluated in same tissues by qPCR. While *Ctns* expression was not detected in the $Ctns^{-/-}$ mice, significant expression was observed in the WT or Shpk KO HSPCs recipients at similar levels (Figure 4.3B). Altogether, these data demonstrate that transplantation of Shpk KO HSPCs are equally efficacious as WT at reducing cystine load by restoring functional cystinosin expression.

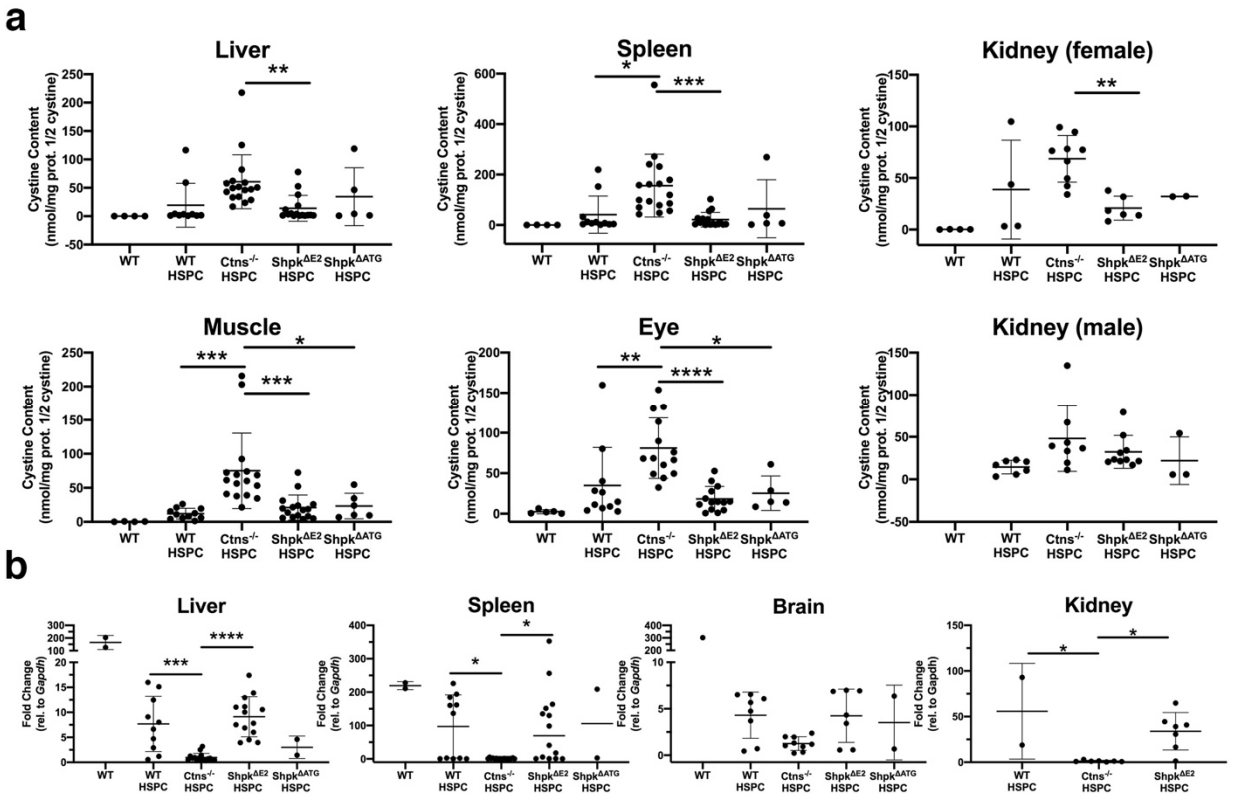

Figure 4.3: Transplantation of Shpk-deficient HSPCs into cystinotic mice effectively reduces cystine accumulation and restores Ctns expression. (Spencer) **(A)** Histograms depicting mass spectrometry analysis of cystine availability following transplantation of WT, *Ctns*$^{-/-}$, *Shpk* $^{\Delta E2}$, and *Shpk* $^{\Delta ATG}$ HSPCs. **(B)** Cystine content normalized to total protein quantitated via BCA assay. Histograms depicting RT-qPCR quantitation of *mCtns* expression relative to housekeeping control *GapDH* gene across several tissue following transplantation of WT, *Ctns*$^{-/-}$, and *Shpk* $^{\Delta E2}$ HSPCs in *Ctns*$^{-/-}$ mice. *mCtns* expression normalized to transplanted *Ctns*$^{-/-}$ HSPCs. . * P<0.05, ** P<0.01, *** P<0.001.

Shpk$^{-/-}$ HSPC transplantation normalizes renal function in Ctns$^{-/-}$ recipient mice. We next assessed the level of kidney function and overall health of recipient cystinotic mice. Blood chemistry analysis did not reveal any significant differences between the HSPC-transplanted groups (Supplemental File 3, Supplemental Table 2). Analysis of complete blood counts (CBC) revealed minor differences between the percentage of lymphocytes and monocytes between individual transplant groups, but values were always within normal range for C57 BL/6 mice, indicating that transplantation of Shpk-deficient stem cells did not specifically alter normal hematopoiesis (Supplemental File 3, Supplemental Tables 3).

To evaluate the renal Fanconi syndrome, we collected 24-hr urine from mice prior to sacrifice. While we did note that healthy wildtype mice had a significantly higher body mass than all groups of cystinotic HSPC recipients, there were no differences between any transplant groups specifically (Supplemental File 3, Supplemental Figure 4A). We also did not observe any changes in polyuria, creatinine clearance, phosphate levels, general proteinuria, or cystatin C measured in the serum (Supplemental File 3, Supplemental Figure 4B-F). Indeed, while a dramatic renal phenotype was seen using the *Ctns*$^{-/-}$ mouse model in the past, we and others have noted steadily decreased symptomatic severity, potentially because of genetic drift(14). As such, we also measured proximal tubular markers that other groups have reported to still be abnormal in the Ctns$^{-/-}$ mouse model(26, 27). We determined that glucosuria was increased in the Ctns$^{-/-}$ controls and was corrected in the WT and Shpk KO HSPC recipients (Figure 4.4A). However, when we examined low-molecular weight proteinuria as measured by abundance of CC16, we did not observe any differences between groups of HSPC recipients, although all groups had significantly higher levels as compared to WT controls (Figure 4.4B). These data further indicate the steadily eroding renal phenotype in this mouse model but also support previous observations of a partial renal Fanconi syndrome phenotype in these cystinotic mice, which is corrected following WT as well as Shpk KO HSPC transplantation.

Histopathology analysis of the kidney section was performed in blind by a certified pathologist. Using a blinded scoring system previously described and performed by a certified pathologist, we observed that tissue morphology is especially susceptible to irradiation required for HSPC transplantation, so we separately considered the untreated and Ctns$^{-/-}$ HSPC cystinotic recipients(12). Regarding the extent of cortical damage, significant reduction of the severity of the kidney damage in WT and Shpk KO HSPC Ctns$^{-/-}$ recipients as compared to Ctns$^{-/-}$ HSPCs

recipients (Figure 4.4C). Glomerulosclerosis, dilated or atrophic convoluted proximal tubules, thickening of the basement membranes, protein casts, and mononuclear infiltrates were reported in all transplanted mice, but at different degree among the different groups appearing most frequent in the $Ctns^{-/-}$ recipients. Thus, WT or Shpk-deficient HSPC has a protective effect on the kidney structure as opposed to $Ctns^{-/-}$ HSPCs in cystinotic mice. In addition, foci of inflammation or mononuclear perivascular cuffs were observed in the lungs of some of the $Ctns^{-/-}$ mice, again most commonly in $Ctns^{-/-}$ recipients (Supplemental File 3, Supplemental Figure 5).

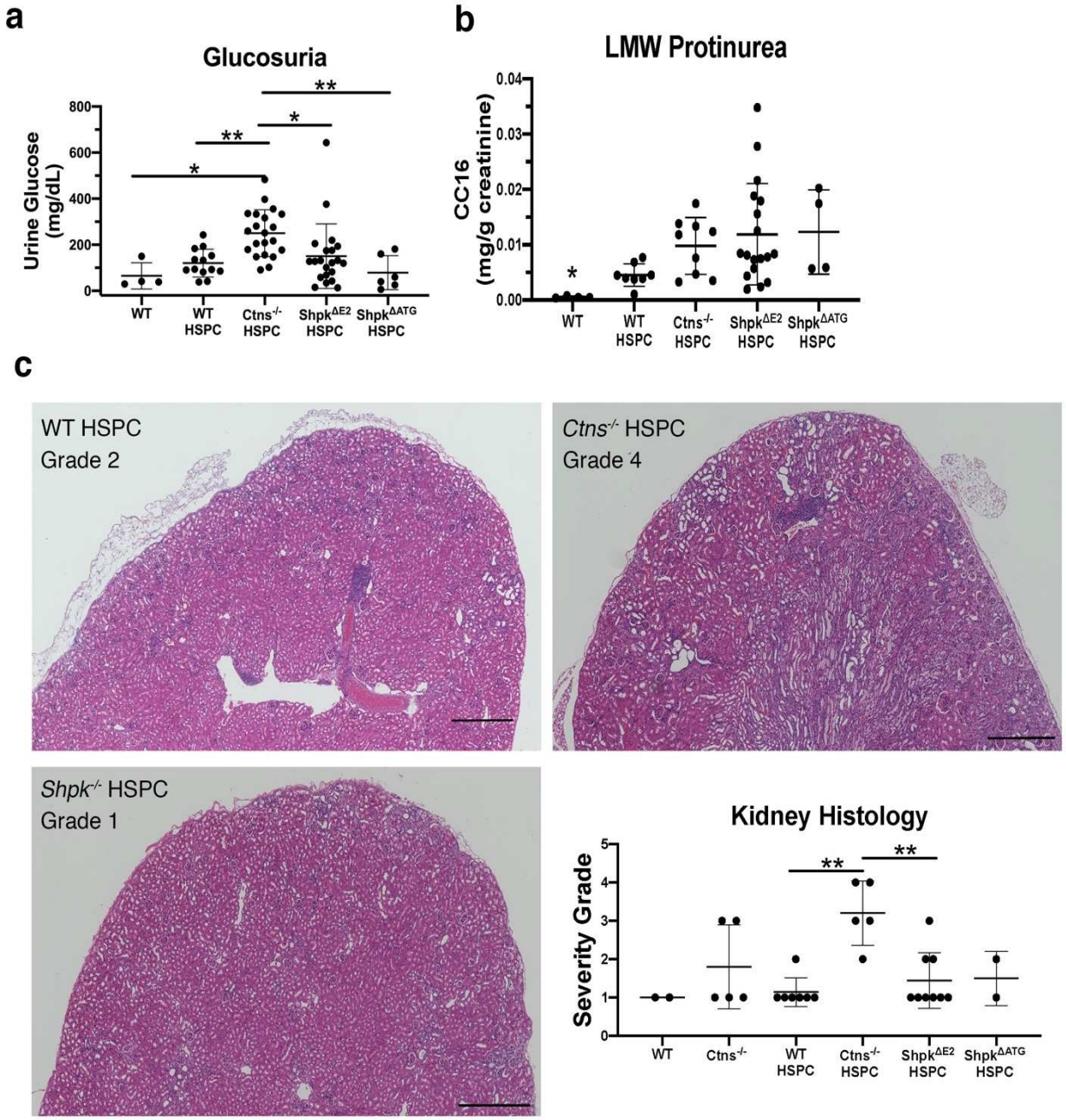

Figure 4.4: Transplantation of Shpk-deficient HSPCs into cystinotic mice reduces markers of renal dysfunction and preserves kidney morphology. **(A and B)** Graphs measuring glucose and low molecular weight (LMW) protein levels in recipient mice six months post-transplantations. Urine samples were collected over 24 hours and treated with protease/phosphatase inhibitors. Error bars represent standard deviation. **(C)** Sample representative H&E images depicting kidney morphology in mice 6-months post-transplant. Samples are graded blind based on cortical damage – see Methods for details. Scale bars = 50 μm. * $P<0.05$, ** $P<0.01$.

***In vivo* and *in vitro* analysis of Shpk$^{-/-}$ macrophages**. In order to identify the HSPC-derived cells *in vivo*, we backcrossed the Shpk KO mice with the DsRed-transgenic mice, to obtain DsRed^{+} Shpk$^{-/-}$ HSPCs. Kidneys and livers section analysis revealed that DsRed^{+} Shpk$^{-/-}$ HSPCs could properly differentiate into macrophages within tissues, colocalizing with F4/80, CD68 and MHC II markers (Figure 5). Tissues from both organs of *Shpk*$^{-/-}$ showed abundant DsRed-positive cell infiltration at levels roughly comparable to wildtype *in vivo*.

We moved to assess if primary cells derived from our knockout models could be employed to further understand the role of *Shpk* in macrophage activity. At the mRNA level, we again observed a decrease in bone marrow-derived macrophages (BMDMs) isolated from Shpk$^{\Delta E2}$ but not Shpk$^{\Delta ATG}$ mice (Supplemental Figure 6A). However, we did not detect any significant changes in the expression of numerous macrophage polarization markers between any genotype (Supplemental Figure 6A). Furthermore, when we isolated protein from BMDMs and probed with several anti-Shpk antibodies, we did not detect any protein expression, even in the WT or *Ctns*$^{-/-}$ conditions (Supplemental Figure 6B). Due to this lack of protein expression, BMDMs do not appear to be an ideal model to investigate the effect of *Shpk* elimination *in vitro.* Experiments are underway using peritoneal macrophages to assess if Shpk protein expression is apparent in the WT condition, and if so, if there is any effect of *Shpk* elimination on macrophage tunneling nanotube formation.

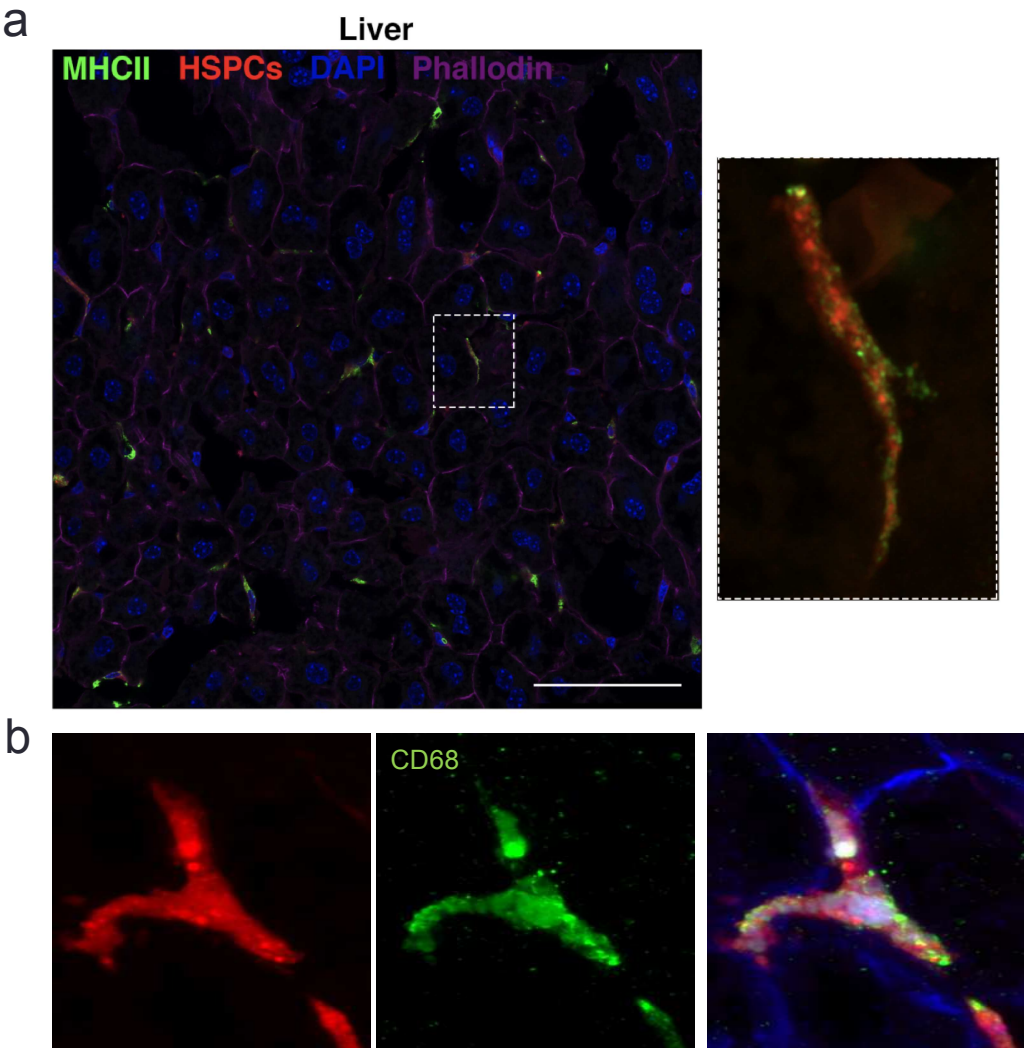

Figure 4.5: Shpk-deficient HSPCs retain the ability to differentiate into tissue-resident macrophages post-transplantation **(A)** Confocal images showing co-localization between transplanted DsRed$^{+/+}$ *Shpk*$^{\Delta E2}$ HSPCs (red) and macrophage markers MHCII in recipient *Ctns*$^{-/-}$ livers. F-actin visualized via phalloidin staining shown in purple. Scale bars = 100 um. **(B)** Zoomed Confocal images showing co-localization with macrophage marker CD68 in the liver. F-actin shown in blue.

4.3: Discussion

The present study characterized the role of the *Shpk* gene in HSPC transplantation therapy for the lysosomal storage disorder cystinosis. This question merited timely evaluation primarily due to the ongoing clinical trial for cystinosis (ClinicalTrials.gov Identifier: NCT03897361) wherein HSPCs from human cystinosis patients are transduced with a lentiviral vector containing functional *CTNS* – but not *SHPK* – cDNA. This was potentially an issue for the patients carrying the 57kb-deletion at the homozygote state because: i) patients most commonly present with a large 57-kb deletion of both the *CTNS* and adjacent *SHPK* loci(4); ii) *SHPK* is known to regulate macrophage differentiation and polarization(20); and iii) HSPC transplantation therapy their differentiation into macrophages that deliver functional cystinosin-bearing lysosomes to diseased tissues(13, 17). Out of an abundance of caution given these facts, patients homozygous for the 57-kb deletion were initially excluded as candidate for the clinical trial.

We generated two novel *Shpk*-deficient mouse knockouts in order to address these concerns and transplanted of $Shpk^{-/-}$ HSPCs into $Ctns^{-/-}$ mice. Through a variety of metrics including renal function, kidney histology, tissue *Ctns* mRNA expression, and most importantly tissue cystine levels, $Ctns^{-/-}$ mice receiving $Shpk^{-/-}$ HSPCs were consistent with WT HSPC recipients and significantly improved compared to untreated $Ctns^{-/-}$ mice or those transplanted with $Ctns^{-/-}$ HSPCs. One potential concern with this approach is that, unlike human 57 kbp homozgyotes, our recipient $Ctns^{-/-}/Shpk^{+/+}$mice model still expressed Ctns. While generation of a novel double-knockout model is underway, our results thus far strongly indicate that *Shpk* is not essential for HSPC transplantation therapeutic efficacy. As such, human subjects homozygous for the 57 kbp deletion have been enrolled as future subjects of the clinical trial.

With the generation and characterization of the first mouse knockouts of *Shpk,* we were able to learn more about the expression, and metabolic function of the gene. The mice carrying the stable heritable mutations of Shpk were viable and fertile. We detect widespread mRNA expression of Shpk in WT mice, as compared to limited studies of *SHPK* mRNA in humans report increased expression in tissues with high biochemical activity such as the liver, kidney, pancreas and heart(23). However, we detected protein expression only readily in mouse liver and to a lesser degree, kidney, but studies of SHPK protein in human tissues have yet to be undertaken to evaluate if human protein expression is limited to these organs.

One particularly interesting finding is that our mouse models effectively recapitulates urinary accumulation of the PPP metabolites erythritol and sedoheptulose. It has been hypothesized that cystinosis patients with the 57-kb deletion have *SHPK*-deficiency (SHPKD) based on elevation of the compounds such as sedoheptulose, erythritol or arabitol, but attribution of this phenotype to *SHPK* deletion specifically is inconclusive(23, 28). While Wamelink *et al.* reported in 2015 that two unrelated patients were discovered to contain isolated *SHPK* deletions with strongly elevated urinary PPP metabolites, our discovery that only *Shpk* but not *Ctns* knockout mice demonstrate elevated urinary erythritol and sedoheptulose provides further independent evidence supporting the hypothesis that the loss of *SHPK* itself in patients does have a detectable effect and may contribute to a small degree to the clinical heterogeneity of cystinosis(24). Our observations of perturbed liver PPP metabolites in *Shpk* knockout mice, while unconfirmed in humans due to the difficulty of obtaining tissue biopsies, further suggest that human metabolic dysregulation is present in tissues rather than confined in the urine

Furthermore, previous studies have shown that in vitro knockdown of Shpk in human macrophages causes a general increase of PPP metabolites R5P, X5P, and G3P, and a decrease in

S7P. Our Shpk-/- in vivo models presented the opposite metabolite perturbation trend except for S7P in the liver. Taken together with urine metabolomics, free-flowing sedoheptulose only enters the catabolic pathway if phosphorylated into S7P(19); thus, in the absence of functional Shpk, we found increased excreted sedoheptulose and lowered converted S7P concentrations in the liver. However, decreases in R5P, G3P, 6-PG, and E4P in response to Shpk-deficiency in tissue once again reiterates that within *in vivo* environments, the functional regulation of Shpk may be context-dependent(29), such as feedback inhibition, metabolic and/or cellular constraints, or alternative enzymatic supply of metabolites. We postulate that since S7P phosphorylation is known to be a rate-limiting carbon-flux rheostat(29), limited supply of S7P may decrease its G6P-conjugated conversion into F6P and E4P within the liver. Our murine observations of perturbed liver PPP metabolites in *Shpk*-/- mice suggest that human metabolic dysregulation is present in tissues rather than confined to only urine and bloodspots. Shpk-/- mice present opportunities for further exploration of the metabolic consequences of Shpk protein in other tissues it is found to be highly expressed such as liver, kidney, and pancreas.

Murine Shpk has also been reported by Haschemi *et al*. to be involved in macrophage polarization *in vitro* in cultured Raw 264.7 cells(20). Following LPS-induced pro-inflammatory stimulation, *SHPK*-overexpressing macrophages showed decreased bio-abundance of PPP intermediates G3P, R5P, and X5P, while unstimulated *SHPK*-knockdown macrophages showed conversely increased levels, as well as reduced S7P levels(20). In contrast, our *in vivo* $Shpk^{-/-}$ tissue of $Shpk^{\Delta E2}$ revealed a general reduction in bio-abundance of PPP intermediates R5P, X5P, 6P6 and glyceraldehyde-3-P, in addition to S7P. We also did not detect any changes in the polarization profiles of either unstimulated BMDMs or peritoneal macrophages derived from our *Shpk* knockout mice. Given the well-known difficulty of macrophage polarization in culture to translate

to the more complex *in vivo* environment, our data highlights the importance of *in vivo* exploration of simplified *in vitro* findings to better represent physiological complexity.

In conclusion, this study reports the generation and characterization novel $Shpk^{-/-}$ mice; prior to this work, Shpk was relatively poorly-studied, especially *in vivo*. We found that *SHPK* deletion led to PPP metabolic dysregulation in tissues, especially liver and kidney, and thus may account for some clinical heterogeneity of cystinosis. Most importantly, we showed that absence of *SHPK* does not alter the mechanistic integrity of the macrophage-mediated HSPC therapy for cystinosis. Therefore, subjects homozygous for the 57-kb deletion are now being enrolled in the autologous HSPC gene therapy clinical trial for cystinosis.

4.4: Methods

Mice and Ethics Statement. C57BL/6 *Ctns*$^{-/-}$ mice were provided by Dr. Antignac (Inserm U983, Paris, France). Shpk$^{\Delta ATG}$ (C57BL/6 *Shpk*$^{-/-}$) mice were generated by the UCSD Mouse Genomics Core. C57BL/6 blastocysts were injected with CRISPR-Cas9 targets aimed the start codon of Shpk genomic locus. Shpk$^{\Delta E2}$ (C57BL/6 *Shpk*$^{-/-}$) mice with CRISPR-Cas9 targets aimed at exon 2 of *Shpk* were obtained from UC Davis. Both strains were continuously bred to homozygosity. Both strains were also crossbred with transgenic DsRed (B6.Cg-Tg(CAG-DsRed*MST)1Nagy/J) mice provided by the Jackson Laboratory (Bar Harbor, ME) to establish colored lines with constitutive expression of DsRed fluorescent protein. All strains and mouse procedures were approved by the University of California, San Diego (UCSD) in accordance with the guidelines set forth by the Institutional Animal Care and Use Committee (Protocol ID S12288).

Mouse Genotyping. Shpk mutant status was identified using PCR-based genotyping assays from mouse tail tissue. DirectPCR (Tail) (Viagen) and Protinease K treatment of mouse tails was used for DNA extraction. PCR protocol of Shpk$^{\Delta ATG}$ DNA amplification is as follows: 95°C (3 min) initial denaturation; 30 cycles of 98°C (20 s) denaturation, 65°C (15 s) annealing, and 72°C (15 s) extension; and 72°C (1 min/kb) final extension. Resultant wild-type band sizes were 632 bp; and mutant size was 495 bp. PCR protocol of Shpk$^{\Delta E2}$ DNA amplification was provided by UC Davis and is as follows: 94°C (2 min) initial denaturation; 10 cycles of 94°C (10 s) denaturation, 65°C (15 s) annealing with consecutive runs lowering in temperature by 1°C (-1°C/cycle), and 68°C (2 min) extension; and 25 cycles of 94°C (2 min) denaturation, 65°C annealing (30 s), and 68°C (2 min) extension with consecutive runs increasing in duration by 20 s (+20 s/cycle). Resultant wild-

type band sizes were 638 and 1184 bp; and mutant size was 500 bp. Primer sequences found in Table S1.

Cell isolation and culture. Bone-marrow derived macrophages (BMDMs) were isolated as previously described (Goodman et. al., 2019). To isolate thioglycolate-elicited macrophages, donor mice were administered 5 ml of 3% thioglycolate via peritoneal injections. Following inflammatory response spanning 5-7 days, isoflurane-euthanized mice were peritoneally injected with 5 ml of PBS, gently massaged, and removed of injected fluid. Isolated peritoneal macrophages were cultured overnight at 37 °C and 5% CO_2 incubation in complete DMEM media (10% FBS, 2% penicillin/streptomycin) on tissue-culture (TC) treated plastic. Media was changed the following day to remove non-macrophages, and subsequent media changes occurred every two days.

Real Time-qPCR. RNEasy Mini Kit and protocol (Qiagen, Hilden, Germany) was used for whole RNA extraction; blood RNA was extracted using the RNeasy Protect Animal Blood Kit (Qiagen). cDNA synthesis occurred by reverse transcription of 1 ug tissue and blood RNA using iScript cDNA Synthesis Kit (Bio-Rad, Hercules, CA). RT-qPCR reaction assembly consisted of 5 ul iTaq Universal SYBR Green, 3 μL cDNA (5 ng/ul), 0.6 μL forward and reverse primer (10 μM), and 1.8 μL H20, and ran on a CFX96 thermocycler (Bio-Rad) under the following conditions: 95 °C (30 s); 40 cycles of 95 °C (5 s) and 60 °C (30 s); then 65 °C (5 s); and 95 °C (5 s). Gene expression was measured using the delta/delta CT method relative to glyceraldehyde 3-phosphate dehydrogenase (*Gapdh*). All primer sequences are shown in Supplemental Table 1.

Immunoblotting. RIPA lysis buffer (Sigma, St Louis, MO) composed of protease/phosphatase inhibitor cocktail (Thermo Fisher Scientific, Waltham, MA) was used for protein lysis. The Pierce BCA Protein Assay Kit (Thermo Fisher Scientific) was used to calibrate protein concentrations. SDS-NuPAGE treatment of 10-20 ug of protein were ran on 4–12% Bis-Tris Gel (Novex by Life Technologies, Carlsbad, CA) and transferred to PVDF membranes. Primary incubation ran at 4 °C overnight using the following antibodies: Anti-Shpk (Sigma; 1:1,000). The next day, membranes were washed three times in Protein Wash Buffer (Azure Biosystems, Dublin, CA) and incubated in HRP-conjugated secondary antibodies goat anti-rabbit (1; 2500 and rhodamine anti-tubulin (BioRad; 1:2,000) for 1 hr at RT. Membranes are again washed three times and a final time in 1x tris buffered saline (TBS). Blots were activated by HRP substrate Radiance Plus ECL Reagent (Azure) and chemiluminescent detection was captured on the c600 Imager (Azure). Western blots were quantitated by comparative densitometry against tubulin loading control.

Metabolomics. Harvested livers were rapidly freeze-clamped and placed in ice-cold liquid nitrogen to preserve robust metabolic activity. Samples were then powderized and 20 mg was suspended in extraction solution (40% methanol/40% acetonitrile/20% H_20) supplemented with 40 μL 13C-labeled internal standards (Cambridge Isotype Laboratories) per mL solution. Samples were homogenized using Precillys homogenizer, immediately returned to dry ice for 1 hr, then spun at 13000 xg for 15 mins. Supernatant was then lyophilized on a speed vac with cold trap to dryness. Data was normalized by comparing the peak area ratio of each compound of Shpk-knockout groups to the average of $Shpk^{+/+}$ mice.

HSPC isolation and transplantation. HSPC isolation and transplantation were performed as previously described (Harrison et. al., 2013). In brief, bone marrow fluid was flushed from harvested tibias and femurs of donor wild-type, $Ctns^{-/-}$, $Shpk^{\Delta ATG}$, and $Shpk^{\Delta E2}$ mice. $Sca1^{+}$ HSPCs were isolated by immunomagnetic separation using magnetic beads conjugated to anti-ScaI antibody (Miltenyi Biotec, Auburn, CA). $Ctns^{-/-}$ mice subjected to 6.5 Gy lethal irradiation the previous day were transplanted with 100 µL containing 1×10^6 HSPCs via tail vein injection. At ~6 months post-transplantation, recipient mice were sacrificed and kidney, liver, and spleen samples were isolated for analyses of therapeutic efficacy.

Cystine Content. Tissue cystine was measured as previously described (Harrison et. al., 2013). Briefly, explanted tissues were homogenized using the Precellys 24 homogenizer (Bertin Technologies) N-ethylmaleimide (Fluka Biochemika). Lysates were transferred to 15% % 5-sulfosalicylic acid (SSA) (Fluka Biochemika) and centrifuged to remove proteins for comparative quantitation using BCA assay (Pierce). The cystine-containing supernatants were transferred to 3% SSA and diluted before being quantitated by mass spectrometry at the UCSD Biochemical Genetics as described previously (Gertsman cystine paper).

Histology. To assess general tissue morphology, dissected tissues were fixed in 10% formalin for 48 hrs and then transferred to the UCSD Moores Cancer Center Biorepository & Tissue Technology Center. Samples were embedded in paraffin, sectioned at 4µm and stained with routine H&E staining to assess histologic anomalies. For kidney, further analysis was done in order to quantify the extent of cortical damage as previously described [12]. To estimate the extend of the affected parenchyma in kidneys, periodic acid- shift (PAS) staining was also performed, which

stains basement membrane, so is useful for evaluating glomerular cell number, basement membrane, mesangium, tubular basement membrane and apical end of the proximal convoluted tubule epithelium's brush border [30]. All kidney's H&E and PAS slides were blindly scored by Dr. Valeria Estrada (Tissue Technology Shared Resource, Moores Cancer Center, UCSD) based on extent of cortical damage ; a grade of 1 corresponded to 0-10% damage, Grade 2 to 10-30%, Grade 3 to 30-50% and Grade 4 to 50-70% (Yeagy paper).

Immunofluorescence. For marker immunofluorescence, tissues were fixed in 4% paraformaldehyde, dehydrated in 20% sucrose and mounted in Tissue Tek Optimum Cutting Temperature (OCT) stored at -80°C. Tissues were cut into 16 um-wide sections and placed on IHC slides. For staining, slides were washed in PBS three times for 10 mins at RT, treated with blocking buffer (1% BSA, 5% goat serum, 0.3% triton X-100) for 1 hour at RT, and probed with macrophage markers CD68 (Biolegend; 1:500), F4/80 (Abcam; 1:500), and MHCII1:500, COMPANY) primary antibodies overnight at 4°C. The following day, slides were washed in PBS three times and probed with secondary antibodies anti-rabbit AF562 (1:500, COMPANY) and phalloidin AF647 (Invitrogen; 1:200) for 1 hour at RT. After two more 10-minute PBS washes and a final PBS and DAPI (1:1000) wash, slides were mounted with glass slips using Prolong Gold. The following day, images were taken using the LSM 880 confocal microscope (Zeiss).

Renal Function. 24-hour urine collections was preformed using metabolic cages with collection over ice and treated with 100x Protease Inhibitors (Sigma). Renal markers creatinine, creatinine clearance, phosphate, and urea were measured using colorimetric assays according to the manufacturer recommendations (BioAssay Systems, Hayward, CA) as previously described

(Harrison et. al., 2013). Total protein was measured using Pierce BCA Protein Assay Kit (Thermo Fisher Scientific) as previously described (Harrison et. al., 2013). Low molecular weight (LMW) proteinurea indicator Clara cell protein of 16 kDa (CC16) was assayed via ELISA (BIOMATIK) per manufactures recommendation. Plasma serum was obtained from survival retro-orbital bleeding and analyzed for creatinine, phosphate, glucose, and urea.

CBC and Blood Chemistry: Blood was collected prior to sacrifice 6 months post-transplant. Blood chemistry was analyzed by ACP Diagnostic Services Laboratory at UCSD and comprised of a custom panel of assays focused on testing liver, pancreas, and renal functions, blood glucose and electrolyte measurements.

Statistics. All statistics were analyzed using Graphpad Prism 8 software. Briefly, Student's *t*-test was used for comparisons of two groups, and one-way analysis of variance (ANOVA) for comparisons of three or more conditions with Tukey's multiple comparison test used to evaluate differences between individual groups. For histological scoring comparisons, the Kruskal Wallis test was employed, followed by Dunn's multiple correction. All graphs display mean ± standard deviation.

4.5: Acknowledgements

Chapter 4, in whole, is currently being prepared for submission for publication of the material. Goodman, S., Khan, M., Li, Z., Sharma, J., Cano, J., Costellanos, C., Estrada, V., Gertsman, I., Cherqui, S. The dissertation author was the primary investigator and author of this material.

4.6: References

1. Emma, F., G. Nesterova, C. Langman, A. Labbe, S. Cherqui, P. Goodyer, M.C. Janssen, M. Greco, R. Topaloglu, E. Elenberg, R. Dohil, D. Trauner, C. Antignac, P. Cochat, F. Kaskel, A. Servais, E. Wuhl, P. Niaudet, W. Van't Hoff, W. Gahl, and E. Levtchenko, Nephropathic cystinosis: an international consensus document. Nephrol Dial Transplant, 2014. 29 Suppl 4: p. iv87-94.

2. Cherqui, S., C. Sevin, G. Hamard, V. Kalatzis, M. Sich, M.O. Pequignot, K. Gogat, M. Abitbol, M. Broyer, M.C. Gubler, and C. Antignac, Intralysosomal cystine accumulation in mice lacking cystinosin, the protein defective in cystinosis. Mol Cell Biol, 2002. 22(21): p. 7622-32.

3. Kalatzis, V., S. Cherqui, C. Antignac, and B. Gasnier, Cystinosin, the protein defective in cystinosis, is a H(+)-driven lysosomal cystine transporter. EMBO J, 2001. 20(21): p. 5940-9.

4. David, D., S. Princiero Berlingerio, M.A. Elmonem, F. Oliveira Arcolino, N. Soliman, B. van den Heuvel, R. Gijsbers, and E. Levtchenko, Molecular Basis of Cystinosis: Geographic Distribution, Functional Consequences of Mutations in the CTNS Gene, and Potential for Repair. Nephron, 2019. 141(2): p. 133-146.

5. Chiaverini, C., H.Y. Kang, L. Sillard, E. Berard, P. Niaudet, G. Guest, M. Cailliez, P. Bahadoran, J.P. Lacour, R. Ballotti, and J.P. Ortonne, In vivo reflectance confocal microscopy of the skin: a noninvasive means of assessing body cystine accumulation in infantile cystinosis. J Am Acad Dermatol, 2013. 68(4): p. e111-e116.

6. Baumner, S. and L.T. Weber, Nephropathic Cystinosis: Symptoms, Treatment, and Perspectives of a Systemic Disease. Front Pediatr, 2018. 6: p. 58.

7. Brodin-Sartorius, A., M.J. Tete, P. Niaudet, C. Antignac, G. Guest, C. Ottolenghi, M. Carbit, D. Moyse, C. Legendre, P. Lesavre, P. Cochat, and A. Servais, Cysteamine therapy delays the progression of nephropathic cystinosis in late adolescents and adults. Kidney Int, 2012. 81(2): p. 179-89.

8. Thoene, J.G., R.G. Oshima, J.C. Crawhall, D.L. Olson, and J.A. Schneider, Cystinosis. Intracellular cystine depletion by aminothiols in vitro and in vivo. J Clin Invest, 1976. 58(1): p. 180-9.

9. Cherqui, S., Cysteamine therapy: a treatment for cystinosis, not a cure. Kidney Int, 2012. 81(2): p. 127-9.

10. Syres, K., F. Harrison, M. Tadlock, J.V. Jester, J. Simpson, S. Roy, D.R. Salomon, and S. Cherqui, Successful treatment of the murine model of cystinosis using bone marrow cell transplantation. Blood, 2009. 114(12): p. 2542-52.

11. Yeagy, B.A., F. Harrison, M.C. Gubler, J.A. Koziol, D.R. Salomon, and S. Cherqui, Kidney preservation by bone marrow cell transplantation in hereditary nephropathy. Kidney Int, 2011. 79(11): p. 1198-206.

12. Harrison, F., B.A. Yeagy, C.J. Rocca, D.B. Kohn, D.R. Salomon, and S. Cherqui, Hematopoietic stem cell gene therapy for the multisystemic lysosomal storage disorder cystinosis. Mol Ther, 2013. 21(2): p. 433-44.

13. Naphade, S., J. Sharma, H.P. Gaide Chevronnay, M.A. Shook, B.A. Yeagy, C.J. Rocca, S.N. Ur, A.J. Lau, P.J. Courtoy, and S. Cherqui, Brief reports: Lysosomal cross-correction by hematopoietic stem cell-derived macrophages via tunneling nanotubes. Stem Cells, 2015. 33(1): p. 301-9.

14. Nevo, N., M. Chol, A. Bailleux, V. Kalatzis, L. Morisset, O. Devuyst, M.C. Gubler, and C. Antignac, Renal phenotype of the cystinosis mouse model is dependent upon genetic background. Nephrol Dial Transplant, 2010. 25(4): p. 1059-66.

15. Gaide Chevronnay, H.P., V. Janssens, P. Van Der Smissen, X.H. Liao, Y. Abid, N. Nevo, C. Antignac, S. Refetoff, S. Cherqui, C.E. Pierreux, and P.J. Courtoy, A mouse model suggests two mechanisms for thyroid alterations in infantile cystinosis: decreased thyroglobulin synthesis due to endoplasmic reticulum stress/unfolded protein response and impaired lysosomal processing. Endocrinology, 2015. 156(6): p. 2349-64.

16. Kalatzis, V., N. Serratrice, C. Hippert, O. Payet, C. Arndt, C. Cazevieille, T. Maurice, C. Hamel, F. Malecaze, C. Antignac, A. Muller, and E.J. Kremer, The ocular anomalies in a cystinosis animal model mimic disease pathogenesis. Pediatr Res, 2007. 62(2): p. 156-62.

17. Goodman, S., S. Naphade, M. Khan, J. Sharma, and S. Cherqui, Macrophage polarization impacts tunneling nanotube formation and intercellular organelle trafficking. Sci Rep, 2019. 9(1): p. 14529.

18. Touchman, J.W., Y. Anikster, N.L. Dietrich, V.V. Maduro, G. McDowell, V. Shotelersuk, G.G. Bouffard, S.M. Beckstrom-Sternberg, W.A. Gahl, and E.D. Green, The genomic region encompassing the nephropathic cystinosis gene (CTNS): complete sequencing of a 200-kb segment and discovery of a novel gene within the common cystinosis-causing deletion. Genome Res, 2000. 10(2): p. 165-73.

19. Nagy, C. and A. Haschemi, Sedoheptulose kinase regulates cellular carbohydrate metabolism by sedoheptulose 7-phosphate supply. Biochem Soc Trans, 2013. 41(2): p. 674-80.

20. Haschemi, A., P. Kosma, L. Gille, C.R. Evans, C.F. Burant, P. Starkl, B. Knapp, R. Haas, J.A. Schmid, C. Jandl, S. Amir, G. Lubec, J. Park, H. Esterbauer, M. Bilban, L. Brizuela, J.A. Pospisilik, L.E. Otterbein, and O. Wagner, The sedoheptulose kinase CARKL directs macrophage polarization through control of glucose metabolism. Cell Metab, 2012. 15(6): p. 813-26.

21. Kadlec, J., E. Izaurralde, and S. Cusack, The structural basis for the interaction between nonsense-mediated mRNA decay factors UPF2 and UPF3. Nat Struct Mol Biol, 2004. 11(4): p. 330-7.

22. Stincone, A., A. Prigione, T. Cramer, M.M. Wamelink, K. Campbell, E. Cheung, V. Olin-Sandoval, N.M. Gruning, A. Kruger, M. Tauqeer Alam, M.A. Keller, M. Breitenbach, K.M. Brindle, J.D. Rabinowitz, and M. Ralser, The return of metabolism: biochemistry and physiology of the pentose phosphate pathway. Biol Rev Camb Philos Soc, 2015. 90(3): p. 927-63.

23. Wamelink, M.M., E.A. Struys, E.E. Jansen, E.N. Levtchenko, F.S. Zijlstra, U. Engelke, H.J. Blom, C. Jakobs, and R.A. Wevers, Sedoheptulokinase deficiency due to a 57-kb deletion in cystinosis patients causes urinary accumulation of sedoheptulose: elucidation of the CARKL gene. Hum Mutat, 2008. 29(4): p. 532-6.

24. Wamelink, M.M., R.J. Ramos, A.P. van den Elzen, G.J. Ruijter, R. Bonte, L. Diogo, P. Garcia, N. Neves, B. Nota, A. Haschemi, I. Tavares de Almeida, and G.S. Salomons, First two unrelated cases of isolated sedoheptulokinase deficiency: A benign disorder? J Inherit Metab Dis, 2015. 38(5): p. 889-94.

25. Jimenez, P.T., A.I. Frolova, M.M. Chi, N.M. Grindler, A.R. Willcockson, K.A. Reynolds, Q. Zhao, and K.H. Moley, DHEA-mediated inhibition of the pentose phosphate pathway alters oocyte lipid metabolism in mice. Endocrinology, 2013. 154(12): p. 4835-44.

26. Gaide Chevronnay, H.P., V. Janssens, P. Van Der Smissen, F. N'Kuli, N. Nevo, Y. Guiot, E. Levtchenko, E. Marbaix, C.E. Pierreux, S. Cherqui, C. Antignac, and P.J. Courtoy, Time course of pathogenic and adaptation mechanisms in cystinotic mouse kidneys. J Am Soc Nephrol, 2014. 25(6): p. 1256-69.

27. Luciani, A., C. Sirac, S. Terryn, V. Javaugue, J.A. Prange, S. Bender, A. Bonaud, M. Cogne, P. Aucouturier, P. Ronco, F. Bridoux, and O. Devuyst, Impaired Lysosomal Function Underlies Monoclonal Light Chain-Associated Renal Fanconi Syndrome. J Am Soc Nephrol, 2016. 27(7): p. 2049-61.

28. Kardon, T., V. Stroobant, M. Veiga-da-Cunha, and E.V. Schaftingen, Characterization of mammalian sedoheptulokinase and mechanism of formation of erythritol in sedoheptulokinase deficiency. FEBS Lett, 2008. 582(23-24): p. 3330-4.

29. Nagy, C. and A. Haschemi, Time and Demand are Two Critical Dimensions of Immunometabolism: The Process of Macrophage Activation and the Pentose Phosphate Pathway. Front Immunol, 2015. 6: p. 164.

30. Agarwal, S.K., S. Sethi, and A.K. Dinda, Basics of kidney biopsy: A nephrologist's perspective. Indian J Nephrol, 2013. 23(4): p. 243-52.

Chapter 5: Exploration of human cystine crystal imaging

The following Chapter 5, in full, is a reprint of material that has been submitted for publication in the *Journal of the American Medical Association.*

5.1: Introduction

Cystinosis is an autosomal recessive lysosomal storage disorder (LSD) with a prevalence of 1:100,000 live births (1). It is characterized by the accumulation of cystine within lysosomes leading to the build-up of crystallized cystine, which is pathognomonic of cystinosis (2-4). The disorder is caused by mutations or deletions in the CTNS gene encoding the lysosomal cystine transporter cystinosin (5).

The most frequent and severe clinical manifestation of cystinosis is the infantile form that initially presents with renal Fanconi syndrome within the first year of life (6,7). Patients also present with chronic kidney disease (CKD) leading to end-stage renal failure (8). Accumulation of soluble cystine and cystine crystals occurs across the entire body progressively causing multi-organ dysfunction such as hypothyroidism, photophobia, neuromuscular disease, and diabetes, which ultimately leads to renal failure and lethality (9). Cysteamine, the only FDA-approved treatment for cystinosis, can slow but not halt disease progression by enabling the export of lysosomal cystine through alternative transporters (10). Long-term compliance is difficult due to frequent dosing, as well as significant side effects including gastrointestinal discomfort and body odor (11,12).

In clinical practice, the response to cysteamine therapy is determined by measuring white blood cell (WBC) cystine levels (13). However, this standard of care is better suited for short-term monitoring and cysteamine dose adjustments but may not reliably reflect tissue cystine levels. Indeed, not only can a recent dose of cysteamine transiently normalize WBC cystine levels, but

also circulating peripheral WBCs may be exposed to higher concentrations of cysteamine than in tissue (14). A retrospective study showed that cystine crystal density within intestinal mucosal tissue correlated inversely with duration of cysteamine therapy, estimated glomerular filtration rate (eGFR) and mean WBC cystine levels (15). However, even though cystine measurement from tissue would be most accurate, it is an invasive approach unsuited to regularly assess disease status and long-term response to treatment.

This study develops an alternative method to non-invasively and reliably measure long-term cystine crystal accumulation in the skin as a potential novel biomarker for cystinosis. A small study previously showed that cystine crystals could be observed in various regions of the skin in patients using reflectance confocal microscopy (RCM) (16). We extended these findings using intradermal RCM to characterize cystine crystal accumulation by developing an automated, unbiased image analysis workflow to visualize and quantitate the prevalence of crystallization. Using this methodology, we report that cystinosis patients have increased crystal area and volume compared to healthy controls, with maximal accumulation in the papillary dermis. We compared crystal accumulation to numerous clinical endpoints to find that the normalized confocal crystal volume (nCCV) is significantly associated with CKD stage and hypothyroidism. We have developed a potential new biomarker for cystinosis to non-invasively monitor long-term disease status, which may facilitate routine clinical monitoring.

5.2: Results

Participant Characteristics. Overall, 70 cystinosis patients (median [range] age: 10 yrs [0.8,54]; 44.6% female) and 31 healthy individuals (38.7 yrs [10,85]; 53.1% female) were enrolled in the study. Images were acquired from 39 patients and 17 controls in 2018; and 45 patients and 20 controls from 2019. Images were acquired in 2 consecutive years for 26 patients and 11 controls. Patients typically were diagnosed with cystinosis before the age of 2 (mean [SD] age: 1.82 yrs [2.12]) (Supplemental File 4, eTable1). Except two, all patients are being treated with cysteamine, 76.8% (n=53) of whom are taking the delayed release Q2 version Procysbi while 20.3% (n=14) are taking the Q4 form, Cystagon. Of the 70 patients, 21.6% of patients have received at least one kidney transplant. CTNS genotypes were obtained from 51 patients and found to be in accordance with published rates of causative mutations21, 47.1 % are homozygous for the 57-kb deletion, 39.2% are heterozygous, and 13.7% do not carry the 57-kb deletion (Supplemental File 4, eFigure 2A). Other mutations in CTNS gene include indels, frameshifts, substitutions and splice site alterations – all but two newly identified mutations, c.565C>T -Q189* and c.330-14_331dup, have been previously reported. We also measured the expression of MCP-1 and cystatin C in serum from a subset of cystinosis patients (n=40) and healthy controls (n=25). We found that cystinosis patients have significantly higher levels of the inflammatory cytokine MCP-1 (mean[SD] patients 283.6 [143.3], controls 206.6 [96.2] pg/ml, P=0.021) as well as renal function marker cystatin C (patients 4.39 [1.6], controls 2.29 [0.6], P<0.001) (eFigure 2B) (22,23).

Observation of tissue cystine crystals by skin biopsy. Skin-punch biopsies were obtained from two cystinosis patients and one healthy control to document dermal abnormalities associated with cystinosis on histopathology using toluidine blue staining. A 20-year-old male diagnosed with infantile cystinosis at 8-months of age exhibited dermal histiocytes containing 2-8

intracytoplasmic crystals per cell (Figure 5.1A). The structures were most commonly rectangular, triangular or square and rarely needle-shaped occupying 25-90% of the cell cytoplasm. Similar findings were noted in a 45-year-old male diagnosed with infantile cystinosis at 6-months of age, with periadnexal inflammatory histiocytes containing 4-22 square to rectangular to rhomboid shaped intracytoplasmic crystals per cell occupying 10-75% of the cytoplasm (Figure 5.1B). None of these abnormalities were observed in the 29-year-old healthy male control (Figure 5.1C). H&E staining revealed rare perivascular chronic inflammatory cells in the upper dermis of the first patient (Figure 5.1A, right). An additional 3 mm skin punch from the 20-year-old patient was processed for cystine measurement by mass spectrometry, revealing a level at 66.21 nmol half cystine/mg protein.

Observation of skin cystine crystals by reflectance confocal microscopy. While cystine crystals were observed in skin biopsies, such an approach is invasive and not quantitative. We therefore developed a reproducible non-invasive methodology to quantitatively assess skin crystallization. We utilized the Vivascope 3000, a RCM device employed to investigate skin pathologies such as melanoma and inflammation (24,25), to capture images from the epidermis to the upper dermis region of the skin (Figure 5.1D). In addition to being non-invasive, key advantages of RCM compared to routine histology are that multiple large regions (750 μm2) can be readily and rapidly acquired, without the need for fixation or serial sectioning to examine different skin layers.

In the majority of cystinosis patients but not healthy controls, we observed multiple small bright irregularly shaped structures (Figure 5.1D, Supplemental Video 5.1). The region of maximal crystal accumulation was the papillary dermis, the transition zone between the epidermis and dermis (26). As the papillary dermis is known as a highly perfused skin layer, comprised of

connective tissue containing abundant blood vessels and vascular networks (26), our findings suggest that cystine crystallization is enhanced by robust vascularization. Unspecific bright structures can occasionally be seen in controls (Supplemental Video 5.2), most frequently within the superficial layers of the epidermis, especially in darker-skinned subjects, which are likely due to the presence of melanocytes (27).

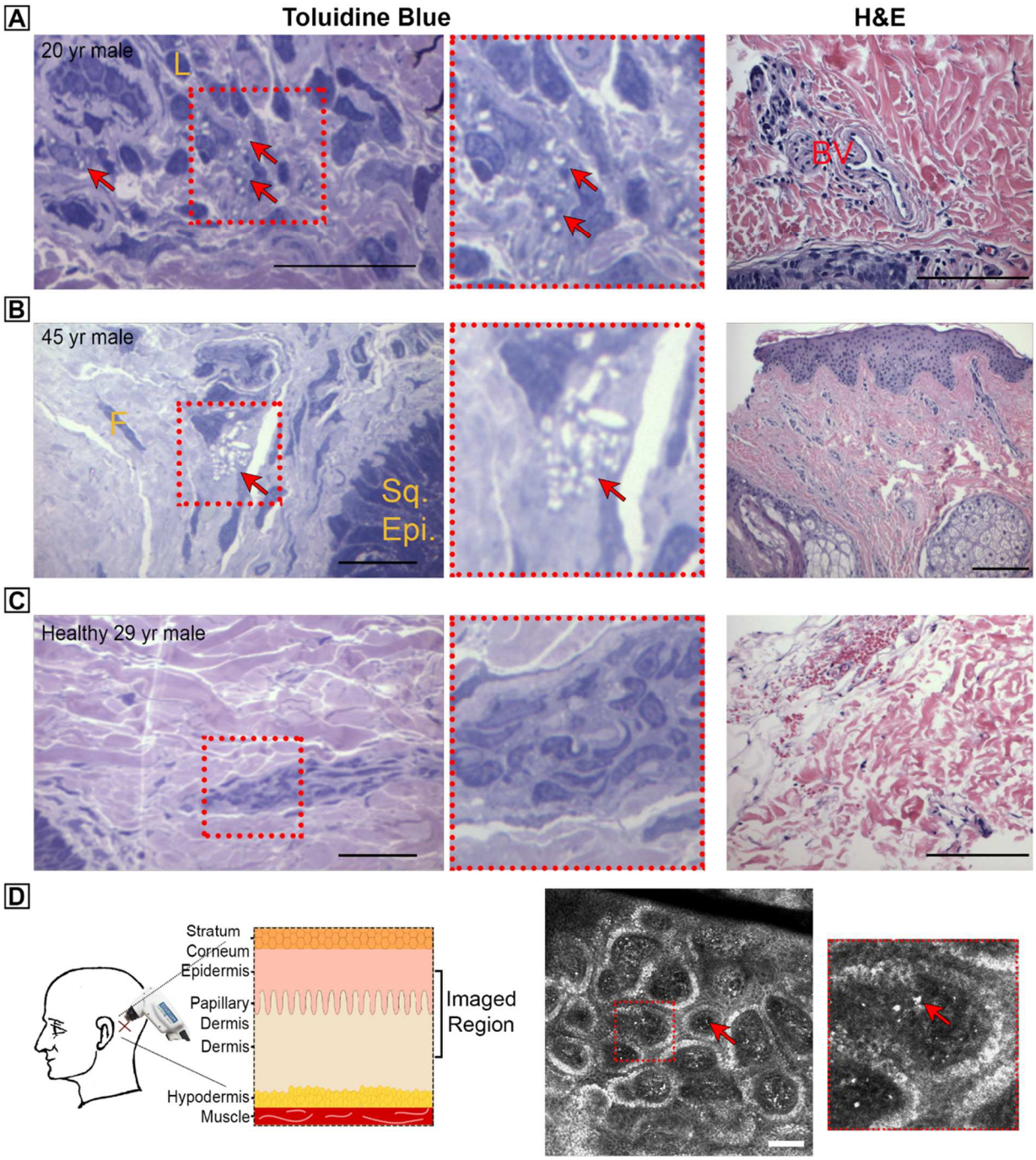

Figure 5.1. Skin biopsies and intradermal confocal imaging highlight crystals in cystinosis patients. **A-C**, Skin punch biopsies taken from 1-2 cm behind the mastoid region of the right ear of two cystinosis patients (**A-B**) and a healthy control (**C**). Samples were sectioned at 1 µm and then stained with Toluidine Blue to detect cystine crystals and H&E for structural evaluation. Arrows indicate crystals. Crystal counting and morphological measurements were conducted by a pathologist. Scale bar = 50 µm for toluidine and 100 µm for H&E . L = lymphocyte, F = fibroblast nucleus, Sq. Epi. = squamous cell epithelium, BV = blood vessel. **D**, Intradermal imaging methodology and sample patient image. Using a handheld RCM device, a 78 slice Zstack with step size of 2.8 µm was taken behind the left ear beginning within the epidermis. A representative single slice with arrows indicating crystals is shown, while complete patient and control Zstacks are provided in Supplemental Videos 5.1-5.2. Scale bar = 100 µm.

Crystal quantification by automated image analysis in 2D. In order to rapidly and reproducibly quantitate the presence of cystine crystals without bias, we generated a novel image analysis workflow using ImagePro Premier 3D (Media Cybernetics). As described in Methods, for each image slice our macro automatically selects and measures the area of crystal-like structures to generate a normalized value representing the sum crystal area relative to the total size of the imaged region (Figure 5.2A left, Supplemental File 4, eFigure 1). Abundant crystal-like structures were detected and quantified in a large majority of patients (Figure 5.2B, Supplemental File 4, Supplemental Video 5.3). Significantly higher total crystal area was observed in patients compared to healthy controls within the papillary dermis region, corresponding to slices 15-50 (Figure 5.2C, Supplemental Video 5.4). The differences were not significant in the epidermis and hypodermis because of high background and low clarity, respectively (Supplemental File 4, eTable 2). Repeated annual images across two years of acquisition further demonstrates that many but not all cystinosis patients ranging from young children to adults display this characteristic increase in crystal accumulation within the superficial dermis, which is not seen in controls (Supplemental File 4, eFigure 3).

Crystal quantification by automated image analysis in 3D reconstructions of the papillary dermis. To visualize and quantitate crystal accumulation in each subject as a single value, we generated 3D reconstructions of the papillary dermal region, encompassing an overall depth of roughly 70 μm (Figure 5.2A right). Patients have markedly higher crystal abundance as compared to controls (Figure 5.2D, Supplemental Videos 5.5-5.6). Total normalized confocal crystal volume (nCCV) was then assessed by measuring the sum volume of crystals followed by normalization to the total size of the 3D region excluding skin structure. We report that cystinosis patients have significantly higher nCCV than healthy controls (mean [SD]: 1934.0 μm^3 [1169.1]

for patients vs. 363.1 μm^3 [194.3] for controls, P<0.001). ROC analysis showed an area under the curve (AUC) of 0.983 (95%CI: 0.957-1.00) for nCCV to discriminate patients from controls.

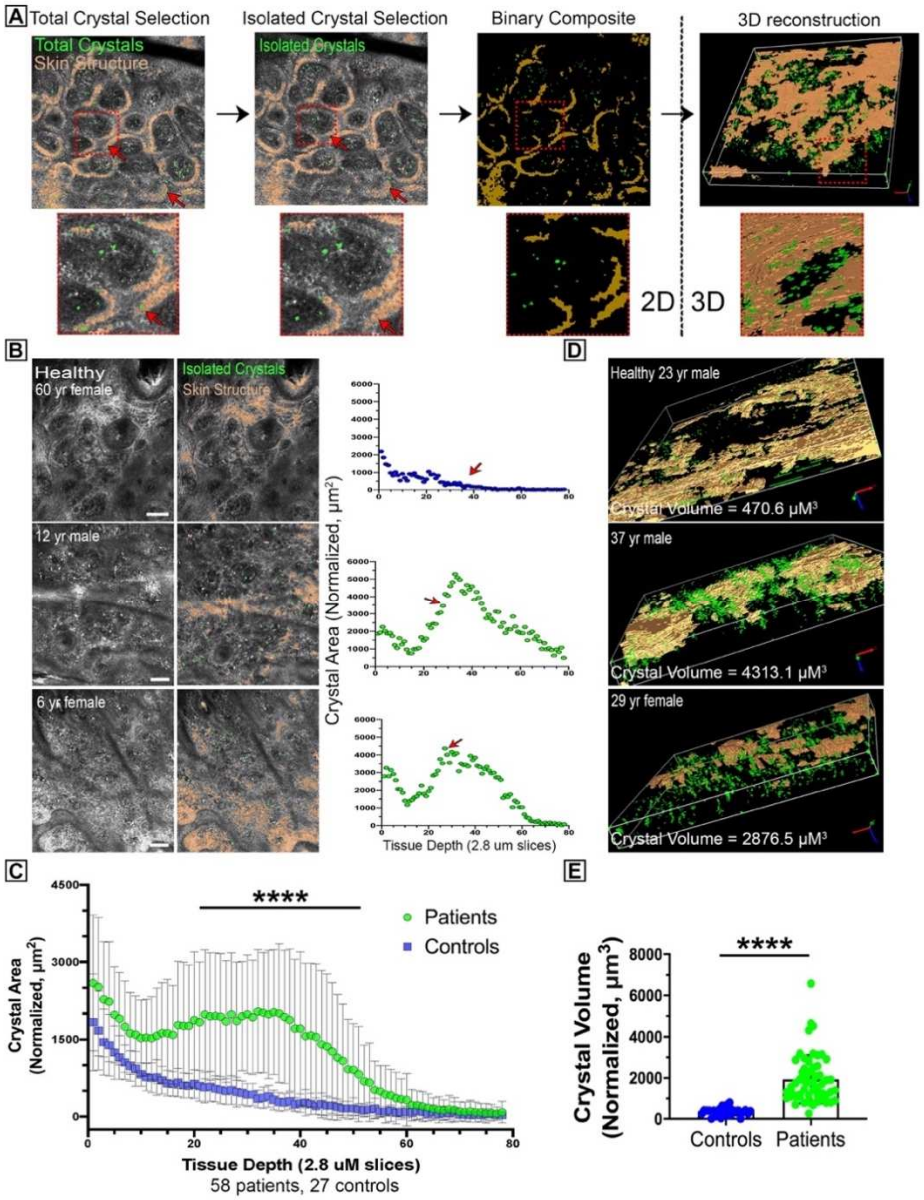

Figure 5.2. Automated 2D and 3D image analysis detects an increased crystallization in cystinotic skin. **A**, Workflow from initial selection of total crystals and skin structure to final 3D reconstruction of the papillary dermis region. Arrows indicate false-positive crystals which are eliminated due to overlap with skin structure. Full description of methodology may be found in eFigure 1 and eMethods. **B**, Representative slices from raw and 2D analyzed intradermal confocal micrographs from a healthy control and patients. XY scatterplot displays sum of crystal area normalized to total imaged region on the Y-axis vs. tissue depth on X-axis. Arrows indicate which slice is the sample image. **C**, XY scatterplot depicting mean crystal area +/- SD vs. tissue depth for grouped cystinosis vs. healthy patients. For subjects with multiple images, only the most recent encounter was included. Starred region indicates slices where patients have significantly higher crystal area. **D**, 3D reconstructions of healthy and patient papillary dermal region. Representative videos are provided in Supplemental Videos 3-4. **E**, Boxplot comparing sum crystal volume (nCCV) between patients and controls. **** = *P*<.001. All scale bars = 100 µm.

To assess the reproducibility of our RCM imaging and subsequent quantification, the same measured position of the mastoid region in three patients and a control were imaged three times sequentially (Supplemental File 4, eFigure 4). We found that all patients and controls had similar measurements - the coefficient of variation (CV) for two patients were below 5% while the third was 18.1%.

Association between normalized confocal crystal volume and medical outcomes. Medical records from 47 patients corresponding to the time of intradermal confocal imaging were collected and blood analysis, urinalysis and disease management data were evaluated in an effort to create a database of cystinosis complications (Table 5.1, Supplemental File 4, eTable 3). We first observed a significant direct correlation between nCCV and age, confirming that crystals progressively accumulate over time (10). We then compared the current standard measure, granulocyte cystine level (median [range]: 1.14 [0.53,6.81] nmol/mg protein ½ cystine), to nCCV and found a moderate correlation (spearman's rho=0.24, P=0.26) when considering patients with infantile cystinosis (n=43). However, granulocyte cystine was available for only a subset of patients (n=24). A negative correlation between granulocyte cystine and cysteamine medication dosage (OR=-0.02, P=0.007) was observed, but no further significant correlations were detected against clinical outcomes. This suggests that either the analysis is under-powered or reflects the ability of this test to measure the short-term impact of cysteamine in the blood as opposed to long-term tissue status. In contrast, we detected significant associations between nCCV and several medical outcomes (Table 5.2). Higher nCCV level was associated with more severe chronic kidney disease stage (slope estimate=0.53, 95%CI: [0.05, 1.00], P=0.03) after adjusting for age and eGFR.

It was also associated with increased risk of hypothyroidism (OR=19.68, 95%CI: [1.60, 242.46], P=0.02) after adjusting for gender.

Table 5.1. Demographic and clinical characteristics of study patients.

Characteristic		**Value**	**Units**
Age (Median [range])		11 (0.8-54)	years
Gender (%)	Female	22 (51.2%)	
	Male	21 (48.8%)	
BMI (Mean[SD])		17.6 (3.3)	kg/m^2
Kidney Transplant (%)	No	34 (79.1%)	
	Yes	9 (20.9%)	
Medication (%)	None	2 (4.7%)	
	Cystagon	8 (18.6%)	
	Procysbi	33 (76.7%	
CKD (patients without kidney transplant) (%)	No	13 (38.2%)	
	Stage1	4 (11.8%)	
	Stage2	8 (23.5%)	
	Stage3	7 (20.6%)	
	Stage4	2 (5.9%)	
Glomerular Filtration Rate (GFR) (Mean[SD])		70.99 (37.40)	mL/min
Hypothyroidism (patients age>=9) (%)	No	12 (60%)	
	Yes	8 (40%)	
Thyroid Stimulating Hormone (TSH) (Mean[SD])		3.7 (6.11)	IU/L
Parathyroid Hormone (PTH) (Mean[SD])		47.06 (43.56)	pg/mL
Cysteamine Dose (Mean[SD])		1185.32 (694.0)	mg
Platelet Count (Mean[SD])		306 (11.74)	
Serum Sodium (Mean[SD])		139.17 (2.61)	mmol/L
nCCV (Mean [SD])		1633.5 (806.5)	μm^3
Granulocyte cystine level (median[IQR])*		1.07 (0.8-1.5)	nmol/mg
Fanconi Syndrome (%)	No	10 (23.3%)	
	Yes	33 (76.7%)	
Polydipsia (%)	No	27 (64.3%)	
	Yes	15 (35.7%)	

* only available for n=24 patients.

Table 5.2. Association between nCCV and various medical outcomes.

Continuous Medical Outcomes	Coefficient (95% CI)	Wald Test Chi-square	p.value
Age (n=57)	0.036 (0.018, 0.053)	16.25	**<0.0005**
BMI (n=33)[a]	0.45 (-0.66, 1.56)	0.64	0.43
Serum Sodium (n=38)[a]	-0.72 (-1.55, 0.11)	2.91	0.08
Systolic Blood Pressure (n=33)[b]	-7.21 (-12.97, -1.44)	6.01	**0.01**
CKD stage (0-5) (n=22)[c]	0.53 (0.05, 1.00)	4.69	**0.03**
Glomerlular Filtration Rate (GFR) (n=34)	-2.39 (-14.90, 10.11)	0.14	0.707
Platelet Count (n=42)	-28.69 (-69.14, 11.76)	1.93	0.164

Binary Medical Outcomes	Odds Ratio (95% CI)	Wald Test Chi-square	p.value
Hypothyroidism (n=20)[d]	19.68 (1.60, 242.46)	5.41	**0.02**
Fanconi Syndrome (n=39)	0.74 (0.36, 1.52)	0.67	0.41
Polydipsia (n=38)	0.99 (0.52, 1.88)	0	0.97

[a]: Model adjusted for age.
[b]: Model adjusted for age and BMI.
[c]: Model adjusted for age and eGFR.
[d]: Model adjusted for gender and restricted to sample with age>=9.
For each of the continuous medical outcomes, separate linear regression model was fit with standardized nCCV as the main predictor.
For each of the binary medical outcomes, separate logistic regression model was fit with the standardized nCCV as the main predictor.

Case studies of cystinosis patients. To take a focused look at the predictive potential of nCCV, this case study closely examined two patients – Patient 1 who is compliant to medication and heterozygous for the 57kb deletion and a one bp duplication (c.696dup- p.Val233Argfs*63) vs. Patient 2 who is non-compliant carrying the 57kb deletion in the homozygous state. Patient 1 is a 20-year-old male presenting with infantile cystinosis diagnosed at 6-month of age, renal Fanconi syndrome, and stage 2 chronic kidney disease (Figure 5.3A, Supplemental Video 5.7). A review of symptoms and a physical exam revealed the patient was fairly asymptomatic due to

cystinosis and had well maintained kidney function. Patient 2 is a 31-year-old male presenting with infantile cystinosis diagnosed at 14-months of age, renal Fanconi syndrome, and chronic kidney failure (Figure 5.3B, Supplemental Video 5.8). A review of symptoms and a physical exam revealed hypothyroidism, photophobia, diabetes mellitus, hypertension, and dysphagia. The patient has received two kidney transplants at 14 and 26 years of age. Patient 1 had a low and stable nCCV from 2018 (935.24 μm^3) to 2019 (803.35 μm^3), while Patient 2 presented with a increase in nCCV between 2019 (3956.3 μm^3) and 2020 (6586.15 μm3) (Figure 5.3C). Differences in crystallization are further reflected in various clinical indicators between the two patients (Figure 5.3D). Treatment compliance, disease control, or underlying genetics can all be potential explanations for this dramatic difference in nCCV.

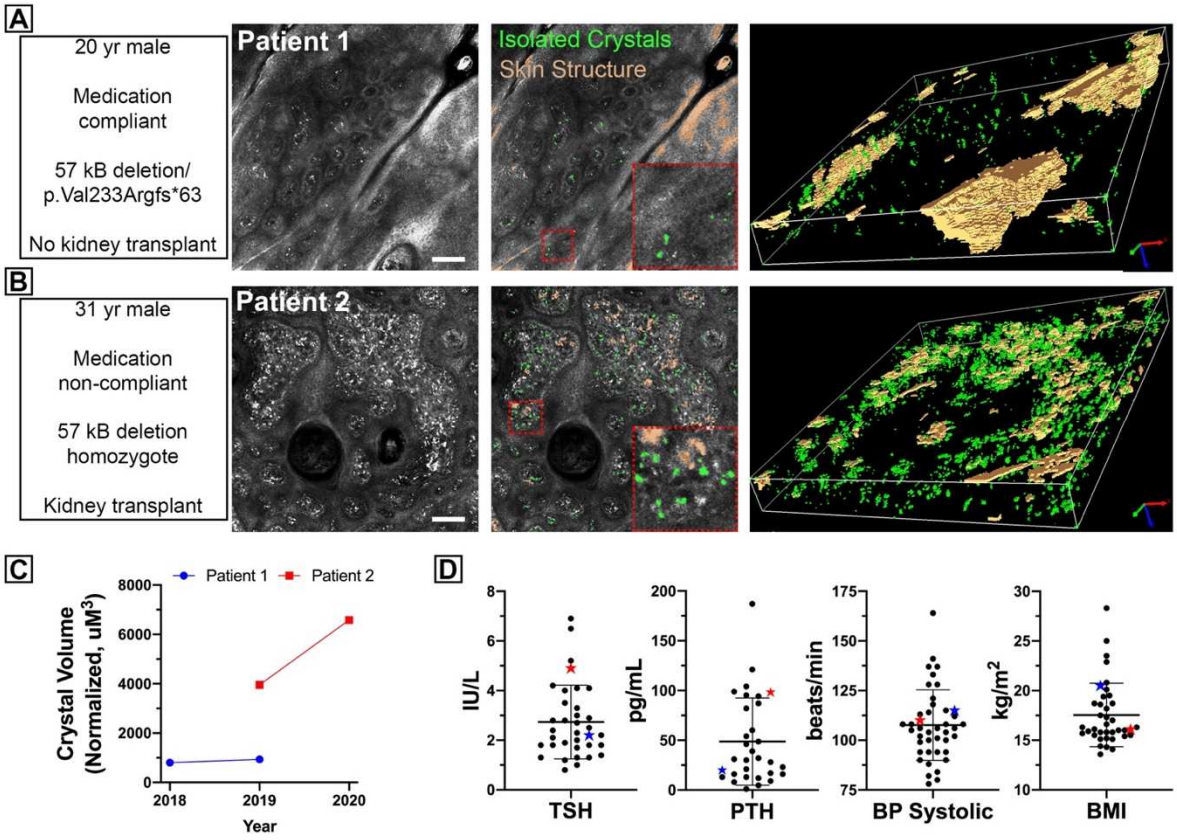

Figure 5.3. Focused case study investigating predictive potential of nCCV for two cystinosis patients. **A-B**, Intradermal imaging and analysis in 2D and 3D for two cystinosis subjects: A) Subject 1, a 20 yr old compliant male heterozygote carrying the 57kb deletion without a kidney transplant and iB) Subject 2, a 31 yr old non-compliant, homozygote for the 57kb deletion who has received two kidney transplantations. Scale bar = 100 μm. **C**, nCCV quantitation of Patients 1 and 2 for multiple years of acquisition. **D,** Selected medical outcomes displaying subject 1 (blue star) and subject 2 (red star) compared to the full set of patients for various symptoms during the most recent year of acquisition

5.3: Discussion

The current standard of care assessment to base dosage and other clinical adjustments in cystinosis relies on the measurement of WBC cystine level. However, this approach is highly dependent on the timing of the most recent dose of cysteamine and is not likely representative of the overall tissue cystine storage (14). This was supported by our study showing a negative correlation between granulocyte cystine and cysteamine medication dosage, but not with other clinical outcomes. This may further reflect the advantage of granulocyte cystine as a short-term metric for dosing adjustments as opposed to long-term measurement of prolonged cystine accumulation in tissues.

Measuring cystine in tissues via biopsy would be a more accurate measure of prolonged cystine accretion. However, this is impractical to implement in routine clinical monitoring. In contrast, intradermal RCM represents a non-invasive and reliable way to monitor patients regularly to visualize and quantify cystine crystals, and determine the impact of oral cysteamine treatment. By using an automated macro for crystal selection that is unbiased and easily reproducible, our results demonstrate standardization, consistency and reproducibility on large cohorts of patients, which can allow future expansion into clinical practice. We thus established an automated measure of normalized confocal crystal volume (nCCV) representing the quantification of crystal volume in 3D reconstituted image stacks. We showed that nCCV was significantly increased in cystinosis patients compared to healthy controls, and that it is increased in older patients.

We sought to determine if the level of crystal accumulation in the skin, as determined by nCCV, would correlate with certain clinical disease states. As expected, due to several factors including medication dosing, compliance to medication, and genetic mutation, patients have wide

variability in disease status and symptom manifestation. The most prevalent long-term complication in cystinosis is CKD (28). Significant correlation between nCCV and the stage of CKD suggests that skin crystallization may either be directly representative of intra-renal cystine accumulation or reflective of the decreased ability of damaged kidneys to filter out cystine. Thyroid dysfunction, a common endocrine complication in cystinosis, manifests clinically in patients as hypothyroidism, and biochemically as elevated thyroid stimulating hormone (TSH) but normal T4 levels (29). We observed a positive association between nCCV and the clinical diagnosis of hypothyroidism. This association further supports that cystine accumulation directly leads to thyroid pathophysiology, a late complication in cystinosis (30). As expected, due to supportive medications to stabilize TSH or T4 levels, no significant association between nCCV and thyroid hormone levels was observed. In contrast, no correlation was found between nCCV and complications such as renal Fanconi syndrome and polydipsia (Table 5.2). These symptoms reflect proximal tubulopathy, which has an early onset in cystinosis and is not considered to be caused by cystine accumulation, but rather due to the absence of the cystinosin protein (7). These data may suggest that non-compliance to cysteamine, a known issue in managing cystinosis, is more likely to be detected by nCCV as opposed to WBC cystine level that can be transiently normalized by taking medication immediately prior to testing.

Here we show that nCCV has the potential to become a biomarker for cystinosis to monitor disease status. Unlike WBC cystine measurement, which is acceptable for evaluating cysteamine dosage adjustments, nCCV directly examines cystine crystal deposition within tissues. The degree of crystallization observed is more likely to be the result of steady prolonged deposition over a longer timeframe, which is more representative of the disease status. Our approach has been used to acquire RCM images from patients over 2 years and we will continue to build a more complete

descriptive epidemiology to improve the understanding, management, and follow-up of cystinosis patients. In the meantime, nCCV is currently being used as an exploratory endpoint in an ongoing clinical trial to monitor the intradermal changes in cystinosis patients after autologous transplantation of gene-modified hematopoietic stem cells (ClinicalTrials.gov Identifier: NCT03897361). Altogether, this study identifies a promising new technology to non-invasively follow disease status and compliance in cystinosis patients.

5.4: Methods

Study design and collection. Under the UCSD International Review Board (IRB) approved protocol #161168, 30 females and 40 males with cystinosis, whose sex has been self-reported, between the ages of 10 months and 54 years of age provided written informed consent and were enrolled in this study. 17 females and 14 males between the ages of 8 to 85 years of age have similarly been enrolled as healthy control subjects. Subjects can enroll or leave the study at any time. Patients were imaged from 2017 to 2019 at Rady Children's Hospital, San Diego, the University of California, San Diego, and the Cystinosis Day of Hope conference in Newport, CA with optional yearly follow-up. Cystinosis patients and controls who cannot remain still for 5 minutes and/or subjects with highly pigmented skin were excluded from the study, due to the observation of higher backgrounds presenting as false positive crystals. This did not substantially affect our subject population because the majority of cystinosis patients are Caucasians of European descent and because of the potential role of cystinosin in melanin synthesis (16). A Rady/UCSD HIPAA authorization form was signed by subjects to allow access to their personal health information (PHI), medical records, for review of diagnosis, medical history and laboratory analysis. Medical outcomes were obtained from records within 6 months before or after confocal imaging.

Human biopsies for histology and mass spectrometry. To obtain skin tissue, punch biopsies with diameters of 4 mm and 3 mm were performed on the area approximately 1-2 cm behind the mastoid region of the right ear. The 4 mm skin punch was cut vertically with half fixed for standard hematoxylin and eosin (H&E) staining in formaldehyde and the other half stained for crystal

visualization with toluene blue by fixation in glutaraldehyde, post-fixation in osmium tetroxide, dehydration in alcohols and finally embedding in epoxy. 1 μm thick sections were cut and imaged using the FEI Technai Spirit BioTWIN. For cystine quantification, the 3 mm punch was fixed in N-Ethylmaleimide (NEM) buffer and analyzed by mass spectrometry as previously described (17).

Intradermal imaging of human skin. To acquire image stacks from patients and controls, we employed the Vivascope 3000 (Caliber I.D.), a handheld in vivo RCM device capable of acquiring 750 μm^2 images from the skin surface to superficial collagen to capture the epidermis and upper dermal layers. The region ~1-2 cm behind the earlobe in the mastoid region was first disinfected with 70% isopropyl alcohol, then mineral oil was applied to the region as an immersion fluid. While holding steady, we acquired a total of 78 images with a 2.8 μm step size, roughly 200 μm deep. Several patients were repeatedly imaged at the same location to establish the reproducibility of our assay.

Image analysis: automated quantitation of crystal-like structure area and volume. All image processing steps were identically performed automatically on every slice of skin Zstacks using ImagePro Premier 3D (Media Cybernetics) (Supplmental File 4, eFigure 1). Full methodology details and filtration settings can be found in eMethods. In brief, we first highlighted total crystals by selecting all small bright objects, then separately selected regions of skin structure. These two regions of interest (ROIs) were combined in order to exclude any false positive crystals which were actually part of the skin structure, leaving only isolated crystals. Crystal area was then measured and normalized to the total region of analysis, excluding the skin structure. Using the selected ROIs, we generated 3D reconstructions of isolated crystals and skin structure within the

region of maximal crystal accumulation. Total normalized crystal volume (nCCV) was quantified by normalizing the sum volume of crystals against the total region of analysis, yielding a single nCCV value per Zstack.

ELISAs. Whole blood was collected from cystinosis patients and healthy subjects using standard venipuncture procedure. Serum was isolated by centrifugation and frozen in aliquots. Serum concentration of MCP-1 (Abcam ab179886) and Cystatin C (Abcam ab179883) were measured via ELISA using manufacturers protocol.

CTNS mutation genotyping. Buccal swabs were collected from cystinosis patients and healthy subjects using the Puritan Hydraflock sterile collection devices (REF: 25-3406-H). DNA was isolated from the buccal swabs using the Gentra Puregene Buccal Cell Kit (Qiagen Cat# 158845) using the manufacturer's protocol. 57 kb deletions were characterized by PCR while exonic Sanger sequencing was employed to determine smaller CTNS indels or substitutions (5).

Statistics. 2D crystal area accumulation was analyzed using two-way ANOVA with Sidak's multiple comparison test to assess the difference between patient and control mean at every image slice. 3D nCCV and ELISA results were compared between cases and controls using a student's t-test. Area under the curve (AUC) analysis was then performed to further verify the sensitivity and specificity of nCCV to discriminate between patients and controls.

In a subset of patients with infantile cystinosis, we studied associations between nCCV and clinical outcomes using logistic regression models for binary outcomes and linear regression models for continuous outcomes. Models adjusted for potential covariates such as age, gender and

BMI. Hypothyroidism was only assessed in patients 9 years and older. Statistical significance was evaluated at $p<0.05$. No multiple comparison correction was applied. All analyses were performed using R (https://www.r-project.org) version 3.5.1).

Medical Records. Estimated Glomerular Filtration Rate (eGFR) was calculated using the bedside Schwart's equation (19). From patients containing a leukocyte cystine level, granulocyte cystine levels were calculated by multiplying the leukocyte cystine level by 1.95 (19).

5.5: Acknowledgements

Chapter 5.1, in whole, has been submitted for publication of the material which may appear in Journal of the American Medical Association. Bengali, M., Goodman, S., Sun, X., Dohil, M., Newbury, R., Dohil, R., Jain, S., Cherqui, S. *"Intradermal imaging of cystine crystals as a non-invasive biomarker for cystinosis."* The dissertation author was the co-primary investigation and equally collaborated in writing the paper.

5.6: References

1.Emma, F., G. Nesterova, C. Langman, A. Labbe, S. Cherqui, P. Goodyer, M.C. Janssen, M. Greco, R. Topaloglu, E. Elenberg, R. Dohil, D. Trauner, C. Antignac, P. Cochat, F. Kaskel, A. Servais, E. Wuhl, P. Niaudet, W. Van't Hoff, W. Gahl, and E. Levtchenko, *Nephropathic cystinosis: an international consensus document.* Nephrol Dial Transplant, 2014. **29 Suppl 4**: p. iv87-94.

2.Kalatzis, V., S. Cherqui, C. Antignac, and B. Gasnier, *Cystinosin, the protein defective in cystinosis, is a H(+)-driven lysosomal cystine transporter.* EMBO J, 2001. **20**(21): p. 5940-9.

3.Cherqui, S., C. Sevin, G. Hamard, V. Kalatzis, M. Sich, M.O. Pequignot, K. Gogat, M. Abitbol, M. Broyer, M.C. Gubler, and C. Antignac, *Intralysosomal cystine accumulation in mice lacking cystinosin, the protein defective in cystinosis.* Mol Cell Biol, 2002. **22**(21): p. 7622-32.

4.Ivanova, E., M.G. De Leo, M.A. De Matteis, and E. Levtchenko, *Cystinosis: clinical presentation, pathogenesis and treatment.* Pediatr Endocrinol Rev, 2014. **12 Suppl 1**: p. 176-84.

5.Forestier, L., G. Jean, M. Attard, S. Cherqui, C. Lewis, W. van't Hoff, M. Broyer, M. Town, and C. Antignac, *Molecular characterization of CTNS deletions in nephropathic cystinosis: development of a PCR-based detection assay.* Am J Hum Genet, 1999. **65**(2): p. 353-9.

6.Haffner, D., A. Weinfurth, F. Manz, H. Schmidt, H.J. Bremer, O. Mehls, and K. Scharer, *Long-term outcome of paediatric patients with hereditary tubular disorders.* Nephron, 1999. **83**(3): p. 250-60.

7.Cherqui, S. and P.J. Courtoy, *The renal Fanconi syndrome in cystinosis: pathogenic insights and therapeutic perspectives.* Nat Rev Nephrol, 2017. **13**(2): p. 115-131.

8.Greco, M., M. Brugnara, M. Zaffanello, A. Taranta, A. Pastore, and F. Emma, *Long-term outcome of nephropathic cystinosis: a 20-year single-center experience.* Pediatr Nephrol, 2010. **25**(12): p. 2459-67.

9.Rocca, C.J., A. Kreymerman, S.N. Ur, K.E. Frizzi, S. Naphade, A. Lau, T. Tran, N.A. Calcutt, J.L. Goldberg, and S. Cherqui, *Treatment of Inherited Eye Defects by Systemic Hematopoietic Stem Cell Transplantation.* Invest Ophthalmol Vis Sci, 2015. **56**(12): p. 7214-23.

10.Brodin-Sartorius, A., M.J. Tete, P. Niaudet, C. Antignac, G. Guest, C. Ottolenghi, M. Charbit, D. Moyse, C. Legendre, P. Lesavre, P. Cochat, and A. Servais, *Cysteamine therapy delays the progression of nephropathic cystinosis in late adolescents and adults.* Kidney Int, 2012. **81**(2): p. 179-89.

11.Cherqui, S., *Cysteamine therapy: a treatment for cystinosis, not a cure.* Kidney Int, 2012. **81**(2): p. 127-9.

12.Ariceta, G., E. Lara, J.A. Camacho, F. Oppenheimer, J. Vara, F. Santos, M.A. Munoz, C. Cantarell, M. Gil Calvo, R. Romero, B. Valenciano, V. Garcia-Nieto, M.J. Sanahuja, J. Crespo, M.L. Justa, A. Urisarri, R. Bedoya, A. Bueno, A. Daza, J. Bravo, F. Llamas, and L.A. Jimenez Del Cerro, *Cysteamine (Cystagon(R)) adherence in patients with cystinosis in Spain: successful in children and a challenge in adolescents and adults.* Nephrol Dial Transplant, 2015. **30**(3): p. 475-80.

13.Wilmer, M.J., J.P. Schoeber, L.P. van den Heuvel, and E.N. Levtchenko, *Cystinosis: practical tools for diagnosis and treatment.* Pediatr Nephrol, 2011. **26**(2): p. 205-15.

14.Belldina, E.B., M.Y. Huang, J.A. Schneider, R.C. Brundage, and T.S. Tracy, *Steady-state pharmacokinetics and pharmacodynamics of cysteamine bitartrate in paediatric nephropathic cystinosis patients.* Br J Clin Pharmacol, 2003. **56**(5): p. 520-5.

15.Dohil, R., A. Carrigg, and R. Newbury, *A potential new method to estimate tissue cystine content in nephropathic cystinosis.* J Pediatr, 2012. **161**(3): p. 531-535 e1.

16.Chiaverini, C., H.Y. Kang, L. Sillard, E. Berard, P. Niaudet, G. Guest, M. Cailliez, P. Bahadoran, J.P. Lacour, R. Ballotti, and J.P. Ortonne, *In vivo reflectance confocal microscopy of the skin: a noninvasive means of assessing body cystine accumulation in infantile cystinosis.* J Am Acad Dermatol, 2013. **68**(4): p. e111-e116

17.Chiaverini, C., L. Sillard, E. Flori, S. Ito, S. Briganti, K. Wakamatsu, E. Fontas, E. Berard, M. Cailliez, P. Cochat, M. Foulard, G. Guest, P. Niaudet, M. Picardo, F.X. Bernard, C. Antignac, J.P. Ortonne, and R. Ballotti, *Cystinosin is a melanosomal protein that regulates melanin synthesis.* FASEB J, 2012. **26**(9): p. 3779-89.

18.Yeagy, B.A., F. Harrison, M.C. Gubler, J.A. Koziol, D.R. Salomon, and S. Cherqui, *Kidney preservation by bone marrow cell transplantation in hereditary nephropathy.* Kidney Int, 2011. **79**(11): p. 1198-206.

19.Schwartz, G.J. and D.F. Work, *Measurement and estimation of GFR in children and adolescents.* Clin J Am Soc Nephrol, 2009. **4**(11): p. 1832-43.

20.Gertsman, I., W.S. Johnson, C. Nishikawa, J.A. Gangoiti, B. Holmes, and B.A. Barshop, *Diagnosis and Monitoring of Cystinosis Using Immunomagnetically Purified Granulocytes.* Clin Chem, 2016. **62**(5): p. 766-72.

21.Gahl, W.A., J.G. Thoene, and J.A. Schneider, *Cystinosis.* N Engl J Med, 2002. **347**(2): p. 111-21.

22.Tatiana Lobry, R.M., Nathalie Nevo, Celine Rocca, Jinzhong Zhang, Stephanie Cherqui, *Interaction between galectin-3 and cystinosin uncovers a pathogenic role of inflammation in kidney involvement of cystinosis.* Kidney Int, 2019

23.Guimaraes, L.P., L.A. Neri, N.M. Sumita, and M.H. Vaisbich, *[Practical markers of renal function in cystinosis patients]*. J Bras Nefrol, 2012. **34**(3): p. 309-12.

24.Maarouf, M., C.M. Costello, S. Gonzalez, I. Angulo, C.N. Curiel-Lewandrowski, and V.Y. Shi, *In Vivo Reflectance Confocal Microscopy: Emerging Role in Noninvasive Diagnosis and Monitoring of Eczematous Dermatoses.* Actas Dermosifiliogr, 2019. **110**(8): p. 626-636.

25.Navarrete-Dechent, C., M. Cordova, K. Liopyris, A. Rishpon, S. Aleissa, A.M. Rossi, E. Lee, C.J. Chen, K.J. Busam, A.A. Marghoob, and K.S. Nehal, *Reflectance confocal microscopy and dermoscopy aid in evaluating repigmentation within or adjacent to lentigo maligna melanoma surgical scars.* J Eur Acad Dermatol Venereol, 2020. **34**(1): p. 74-81.

26.Brown, T.M. and K. Krishnamurthy, *Histology, Dermis*, in *StatPearls*. 2020: Treasure Island (FL).

27.Cichorek, M., M. Wachulska, A. Stasiewicz, and A. Tyminska, *Skin melanocytes: biology and development.* Postepy Dermatol Alergol, 2013. **30**(1): p. 30-41.

28.Baumner, S. and L.T. Weber, *Nephropathic Cystinosis: Symptoms, Treatment, and Perspectives of a Systemic Disease.* Front Pediatr, 2018. **6**: p. 58.

29.Levtchenko, E., *Endocrine Complications of Cystinosis.* J Pediatr, 2017. **183S**: p. S5-S8.

30.Gaide Chevronnay, H.P., V. Janssens, P. Van Der Smissen, X.H. Liao, Y. Abid, N. Nevo, C. Antignac, S. Refetoff, S. Cherqui, C.E. Pierreux, and P.J. Courtoy, *A mouse model suggests two mechanisms for thyroid alterations in infantile cystinosis: decreased thyroglobulin synthesis due to endoplasmic reticulum stress/unfolded protein response and impaired lysosomal processing.* Endocrinology, 2015. **156**(6): p. 2349-64.

Chapter 6: Conclusions

At the broadest level, this work as a whole highlights the unrivaled potential for molecular-based regenerative therapies to expand the nature of a treatable disease. By precisely understanding the mechanistic underpinnings of a disease such as cystinosis or Friedreich's ataxia, we can design more effective and complex therapies to target the root genetic or pathological causes of the disorder. So rather than just treating symptoms as they progress and become more severe, we can use a combination of gene therapy and HSPCs to stimulate and enhance the ability of the patient to restore normal tissue homeostasis – the ultimate goal of regenerative therapies in general.

As our group had previously demonstrated the potential of HSPCs in the mouse model of cystinosis, one major aspect of my work sought to extend this basic knowledge into a more complete picture of the mechanism of action. In pursuit of this goal, I sought a detailed understanding of the nature of macrophage intercellular trafficking of lysosomes through TNTs. I adapted macrophage polarization strategies to facilitate robust study *in vitro* and then developed quantitative high-throughput image analysis strategies. This methodological approach – of automating imaging to draw quantitative conclusions – is a major contribution of this work in general for several important reasons. Firstly, prior to these approaches, many in the field manually counted images for quantification.. Not only is such an approach time consuming but it is inherently subject to experimenter bias, even unconsciously. Furthermore, manual approaches are limiting even if blinded because measuring complex aspects of an image such as shape or area cannot be precisely repeated if done by hand. Secondly, automation inherently allows examination of larger image sets, enabling a dramatical increase in analysis throughput. Beyond improving data reliability, automation of image analysis fundamentally expands the type of insights microscopy can facilitate. For example, researchers have previously described the effect of pro-

inflammatory stimulation upon macrophage cell shape in terms of a more rounded morphology, but by developing a methodology to recognize TNT-like protrusions automatically, I was able to quantitate the frequency of cells which formed protrusion-positive cells. A qualitative observation of a change in morphology was developed into a quantitative assessment of the frequency of the morphological response. Thus, automated strategies – employed here to study frequency of protrusion formation, intercellular trafficking, or cystine crystal accumulation in the skin – improves the ability to discern reliable quantitative data from microscopic images.

Overall, these imaging analyses, when combined with traditional molecular and biochemical approaches, allowed to advance our understanding of macrophage-mediated TNT formation such as proinflammatory macrophages appeared less active at TNT-mediated intercellular trafficking. However, while this work as a whole highlights the translatability of many basic experimental findings to the development of human therapies, in this case we also need to be aware of the serious limitations of such an approach. In this case, macrophage polarization via *in vitro* pushed cells far beyond physiological phenotype, as demonstrated by the retention of the ability of *Rac2*-deficient HSPCs, defective in anti-inflammatory polarization, to prevent cystinosis *in vivo* following transplantation into cystinotic mice. This discrepancy highlights the importance of animal models as a far more complex and biologically meaningful system. While obviously less experimentally tractable, employing transgenic mice allows assessment of the many factors – hormonal, immunological, biochemical or pathological - by which an entire organism will respond to a therapy like HSPC transplantation even if these factors and interactions are not fully known or understood.

The importance of animal study to model complex therapies underscores the next major finding of this work, that is, the role of *Shpk* in HSPC therapy for cystinosis. More than any other

aspect of this work, this project exemplifies the translational appear of regenerative therapy. A question which directly affects patient enrollment in a revolutionary clinical trial could best be addressed by very basic generation and characterization of a novel mouse model to assess the impact of *Shpk*-deficient stem cells. Here again the critical nature of complex models is evident; only by mimicking the genetic mutations of human cystinosis patients in mice were we able to conclude that *Shpk* is unlikely to be a critical determinant of therapeutic success. This evidence was sufficient to permit future enrollment of cystinosis patients homozygous null for *SHPK* in the trial – a dramatic expansion of the pool of patients to recruit and the population which may benefit from therapy.

Of course, despite any amount of rigorous data from predictive animal models, fundamentally the only way to know the outcome of a therapy in humans is to test humans. People are far more complex than any congenic model, and so the ultimate aim of regenerative therapy is and has always been the application of knowledge gained from cells or mice to human subjects. The ongoing Phase I/II clinical trial for cystinosis as a whole is a massive undertaking far larger than any one PhD project. That said, an important element of the success of this or any trial is the ability to accurately and quantitatively assess treatment efficacy, which in the case of rare disorders like cystinosis presents a major challenge. By applying the skills gained from basic image analysis, this work develops such a novel endpoint in the form of nCCV, an automated and quantitative assessment of cystine crystal density in human skin. Our findings that cystinosis patients have significantly higher nCCV than healthy controls, along with tantalizing observed correlations to disease outcomes, indicate that not only can accurately assess if our HSPC therapy is effective, but also have developed a methodology which may lead to a novel biomarker of the disease and eventually directly affect daily clinical management of patients. While this possibility requires

extensive additional patient analysis over years of additional study, it demonstrates how my research exemplifies the translational principle of regenerative medicine to bring molecular conclusions directly to patient care.

While the bulk of this work focuses on the particulars of understanding and developing an HSPC therapy for the rare disorder cystinosis, the principles, methodology and conclusions can be seen as widely applicable to a larger group of genetic disorders. Included here is the application of our transplantation therapy to Friedreich's ataxia, but numerous other organellular loss-of-function disorders are actively under investigation following our approach. As such, the insights into the basic biology we describe are more broadly applicable and can lead to novel therapies for many more disorders and patients. For many years the field of gene therapy in general has struggled to translate its immense promise into actionable therapies. I believe that we stand now upon a critical inflection point as more and more regenerative therapies progress into human trials and ultimately clinical use. This work aims to assist in that progression not only with the data specifically described but also as an conceptual example of the cell to mouse to human regenerative pipeline.